Role of Mixed Layer Depth and Subduction Processes for the Southern Ocean Carbon and Nutrient Cycles

Dissertation

Essowè Panassa
Bremen, March 2018

Gutachter

Prof. Dr. Dieter A. Wolf-Gladrow
Prof. Dr. Birgit Schneider

Vielen Dank an / Thanks to / Merci à ...

Contents

Chapter 1

Summary & Zusammenfassung

Summary

Changes in wind forcing in the Southern Ocean exert a large impact on the dynamics of the surface mixed layer and subduction processes. Over the last two decades, the index of the Southern Annular Mode (SAM) has experienced a trend towards its positive phase, which is characterized by stronger westerly winds. The positive trend in the SAM index results from the complex interaction between the steady increase of atmospheric CO_2 concentration due to anthropogenic emissions and the stratospheric ozone depletion. Co-occurring with the wind signal is the global warming effect driven by the increase in atmospheric CO_2. Increased wind forcing alone would lead to a deepening of the mixed layer and enhance the supply of carbon and nutrients to the euphotic zone. In contrast, the surface ocean warming alone would lead to more surface stratification, and therefore to a shoaling of the mixed layer.

The main objective of this PhD thesis is to answer the question: How did the combined changes in atmospheric forcing affect the surface mixed layer and the carbon and nutrient subduction rates on the timescale of interannual to decadal variability?

In the first part of my thesis, I assessed the impact of the recent changes in atmospheric temperature and zonal wind speed on the summer mixed-layer depth (MLD) in the SO (south of 30°S) from observations and a set of model sensitivity experiments over the period of 2002-2011. The study showed that summer MLD changes in response to recent atmospheric forcing were zonally asymmetric. Summer MLD increased in the Antarctic Zone of the Atlantic and the Indian Ocean sectors. Overall, the effect of recent changes in wind forcing dominated over temperature-induced changes in summer MLD.

In the second part of this thesis, I examined the decadal variability in nutrient and dissolved inorganic carbon (DIC) concentrations in the Antarctic Intermediate Water of the Atlantic sector of the Southern Ocean between 1990 and 2014 using cruise data sampled along the Prime Meridian. The results showed a positive trend in DIC and nitrate concentrations along with a negative trend in temperature and salinity. These observations support a scenario of an increase in the upper-ocean overturning circulation probably linked to the positive trend in the SAM index.

The third part of this thesis focused on the SAM impact on the inter-annual variability

of carbon and nutrient subduction rates across the base of the winter mixed layer between 1958 and 2016 using a coupled physical-biogeochemical general circulation model. The study showed that the variations in SAM led to large-scale anomalies in carbon and nutrient subduction and obduction rates that are zonally symmetric. More obduction occured south of the Antarctic Polar Front (APF) and more subduction occurred where the MLD gradient is strongest in response to the positive trend in the SAM index. Also, I found that the annual mean carbon and nutrient subduction rates varied by around 10% around the long-term mean on interannual to decadal time scales with a stronger positive trend since 1990 leading to an approximately 20% increase in DIC and nitrate subduction rates between 1990 and 2016.

My findings (parts I, II and III) suggest that the positive trend of the SAM index (wind intensification) has profoundly affected the surface mixed layer, and increased upwelling of carbon and nutrient-rich deep water. The increased upwelling is driven by the Ekman divergence and is balanced by the stronger northward Ekman transport across the APF. North of the APF these water masses subduct as mode and intermediate waters. While today changes in the wind forcing play a larger role than atmospheric temperature changes, this might reverse in the future.

Zusammenfassung

Änderungen der Windeinwirkung im Südlichen Ozean üben einen großen Einfluss auf die Dynamik der durchmischten Oberflächen-Schicht und Subduktions-Prozesse aus. Während der letzten beiden Dekaden erfuhr der Southern Annular Mode (SAM) Index einen Trend in Richtung positive Phase, die durch stärkere Westwinde charakterisiert ist. Der positive Trend im SAM Index resultiert aus einer komplexen Wechselbeziehung zwischen der stetigen Erhöhung der CO_2 Konzentration in der Atmosphäre aufgrund von anthropogenen Emissionen und dem Ozonloch in der Stratosphäre. Gleichzeitig zum Windsignal tritt der Effekt der globalen Erwärmung auf, der durch den Anstieg des atmosphärischen CO_2 gesteuert wird. Erhöhter Windantrieb allein würde zu einer Vertiefung der durchmischten Oberflächen-Schicht führen und die Versorgung der euphotischen Zone mit Kohlenstoff und Nährstoffen verstärken. Im Gegensatz dazu würde eine Erwärmung der Meeresoberfläche allein zu stärkerer Schichtung und deshalb zu einer flacheren durchmischten Oberflächen-Schicht führen.

Das Hauptziel dieser Dissertation ist die Beantwortung der Frage: Wie beeinflussten die kombinierten Änderungen in der Atmosphäre die durchmischte Oberflächen-Schicht und die Subduktionsraten von Kohlenstoff und Nährstoffen auf einer Zeitskala von zwischenjährlichen bis dekadischen Schwankungen?

Im ersten Teil meiner Dissertation verglich ich den Einfluss von rezenten Änderungen der Atmosphärentemperatur und der zonalen Windgeschwindigkeiten auf die durchmischte Oberflächen-Schicht (MLD) im Südlichen Ozean (südlich von 30°S) anhand von Beobachtungsdaten mit einer Reihe von Modell-Sensitivitäts-Experimenten über die Zeitspanne von 2002 bis 2011. Die Studie zeigte, dass die MLD Änderungen als Reaktion auf die rezenten atmosphärischen Treiber zonal asymmetrisch waren. Die Sommer MLD nahm in der Antarktischen Zone des Atlantischen und Indischen Ozeansektors zu. Insgesamt dominierte der Effekt von rezenten Windänderungen gegenüber Temperaturänderungen auf die Sommer MLD.

Im zweiten Teil dieser Dissertation untersuchte ich mithilfe eines Datensatzes, der entlang des Nullmeridians genommen wurde, dekadische Schwankungen in den Konzentrationen von Nährstoffen und gelöstem anorganischem Kohlenstoff (DIC) im antarktischen

Zwischenwasser des Atlantischen Sektors des Südlichen Ozeans zwischen 1990 und 2014. Die Ergebnisse zeigten einen positiven Trend bei DIC und Nitratkonzentrationen zusammen mit einem negativen Trend bei Temperatur und Salzgehalt. Diese Beobachtungen stützen das Szenario einer Beschleunigung der Umwälzzirkulation im oberen Ozean, das wahrscheinlich gekoppelt ist an den positiven Trend im SAM Index.

Der dritte Teil dieser Dissertation konzentrierte sich auf den Einfluss von SAM auf die zwischenjährlichen Schwankungen von Kohlenstoff- und Nährstoff-Subduktionsraten durch das tiefste Level der durchmischten Oberflächen-Schicht im Winter zwischen 1958 und 2016. Hierfür benutzte ich ein gekoppeltes physikalisch-biogeochemisches Zirkulationsmodell. Die Studie zeigte, dass die Schwankungen in SAM zu groskaligen Anomalien in Kohlenstoff- und Nährstoff-Subduktions- und Obduktionsraten führten, die zonal symmetrisch sind. Südlich der Antarktischen Polarfront (APF) fand mehr Obduktion statt, während dort, wo der MLD-Gradient am stärksten ist, mehr Subduktion stattfand als Reaktion auf den positiven Trend im SAM Index. Ein weiteres Ergebnis war, dass die jährlichen durchschnittlichen Kohlenstoff- und Nährstoff-Subduktionsraten um ungefähr 10% um das langjährige Mittel auf jährlichen bis dekadischen Zeitskalen schwankten, mit einem stärkeren positiven Trend seit 1990, der zu einer Zunahme der DIC und Nitrat-Subduktionsrate um 20% zwischen 1990 und 2016 geführt hat.

Meine Forschungsergebnisse (Teile I, II und III) deuten darauf hin, dass der positive Trend im SAM Index (Intensivierung der Winde) die durchmischte Oberflächen-Schicht ebenso tiefgreifend beeinflusst hat wie auch den vermehrten Auftrieb von kohlenstoff- und nährstoffreichem Tiefenwasser. Der vermehrte Auftrieb wird angetrieben von der Ekman Divergenz, und wird vom stärkeren nördlichen Ekman Transport über die APF ausgeglichen. Nördlich der APF tauchen diese Wassermassen als Mode- und Zwischenwasser ab. Während Windveränderungen heute eine größere Rolle spielen als atmosphärische Temperaturveränderungen, ist es gut möglich, dass sich dies in Zukunft umkehrt.

Chapter 2

Introduction

2.1   The global carbon cycle

Since the beginning of the preindustrial era (about 1750), the concentration of carbon dioxide (CO_2) in the atmosphere has been building up continuously. From 277 parts per million (ppm) in 1750 (*Joos and Spahni*, 2008), the CO_2 mixing ratio has reached now 407 ppm in December 2017 which is equivalent to an amount of 862 Pg carbon (*Keeling et al.*, 1976; *Dlugokencky and Tans*, 2018). This is predominantly caused by the steady release of carbon to the atmosphere due to human activities, namely burning of fossil fuels, cement production, and land-use change. The anthropogenic carbon is redistributed among the atmosphere, ocean and terrestrial biosphere reservoirs. Of the total estimated carbon emissions due to fossil fuels and land-use change over the last decade 2007-2016, about 50% stayed in the atmosphere, 25-30% were taken up by the ocean and 25-30% ended up on land (*Le Quéré et al.*, 2017). The estimated contribution of the ocean and land sink (SOCEAN 2.4 $\pm$ 0.5 GtC yr^{-1}, and SLAND 3.0 $\pm$ 0.8 GtC yr^{-1}; Figure 2.1) exhibited substantial variability, but have remained in the same range throughout the last decade 2007-2016 (*Le Quéré et al.*, 2017). The Southern Ocean (SO) alone sequesters about 40% from the total 25-30% carbon sequestered by the global ocean (*Khatiwala et al.*, 2009; 2013). This highlights its importance in the global carbon cycle. The efficiency of the SO in the uptake of the anthropogenic carbon at the surface ocean is controlled by the physical and biological carbon pumps (*Volk and Hoffert*, 1985). The biological carbon pump is inefficient in the Southern Ocean, a High-Nitrate Low-Chlorophyll (HNLC) region, because of iron limitation (*de Baar et al.*, 1990; *Smetacek et al.*, 2012).

2.1.1   The marine carbon cycle

The biological carbon pumps

The biological carbon pump consists of two components, the soft-tissue and the carbonate counter pump. The soft-tissue pump encompasses organic matter production by photosynthesis (Eq. 2.1),

$$CO_2 + H_2O + light \rightarrow CH_2O + O_2, \qquad (2.1)$$
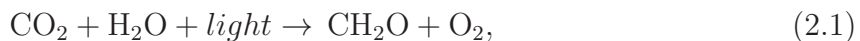
export of organic material out of the surface ocean and remineralization in deeper ocean layers (*Sigman and Hain*, 2012). Part of the organic matter produced by the phytoplankton is directly recycled within the euphotic zone and constitutes the regenerated production. The remaining part sinks to deep waters. Part of the organic matter that sinks to the deeper layers is remineralized into dissolved inorganic carbon (DIC) and nutrients and transported back to the surface ocean by upwelling where it sustains new production
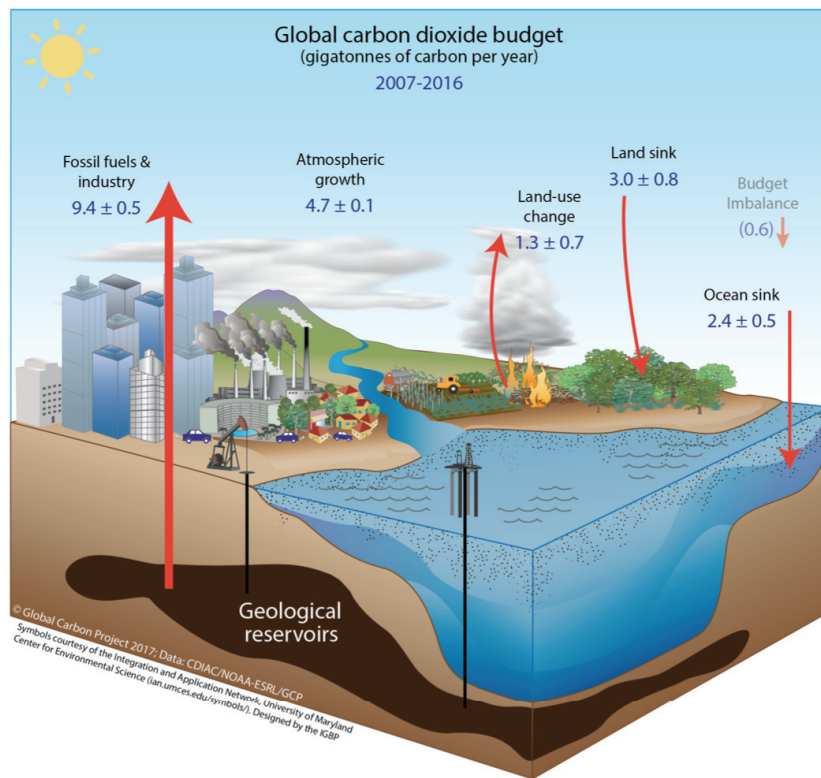
Figure 2.1: Schematic representation of the perturbation of the global carbon cycle caused by anthropogenic activities, averaged globally for the decade 2007-2016 (*Le Quéré et al.*, 2017).

(*Dugdale and Goering*, 1967). The remaining organic matter not remineralized sinks to the bottom and is stored in the sediments for a time scales of hundreds to thousands of years (*Sundquist*, 1993). The carbonate counter pump encompasses calcium carbonate ($CaCO_3$) production and sinking by calcifying organisms such as coccolithophores and zooplankton (foraminifera) that use calcium (Ca) and DIC to form $CaCO_3$ following Eq. 2.2.

$$Ca^{2+} + 2\,HCO_3^- \rightarrow CaCO_3 + CO_2 + H_2O \qquad (2.2)$$

The formation of calcium carbonate in the surface ocean releases CO_2 and as a consequence increases pCO_2 in the surface ocean. This effect is opposite to the soft tissue pump that leads to a decrease of pCO_2 in the surface ocean. As calcium carbonate is much denser than sea water, it sinks to deep ocean layers where it is sequestered in the sediment layer at the sea floor. A fraction of the calcium carbonate sinking to depth is dissolved as pressure increases towards the sea floor. Dissolution of the calcium carbonate is also provoked by the soft-tissue pump (organic matter remineralization at depth) that lowers the pH of the deep ocean (*Sigman and Hain*, 2012). The combined effects of soft

and hard-tissue pumps contribute to increase deep ocean DIC.

2.1.2   The physical carbon pump

The physical carbon pump represents the physical process of carbon transport that is associated with deep vertical mixing. The cooling of the surface seawater leads to more uptake of carbon dioxide from the atmosphere by the ocean. In contrast, warming of surface seawater releases more CO_2 to the atmosphere. The solubility of CO_2 in seawater is a strong function of temperature and is controlled by thermodynamic equilibrium given by Henry's law (Eq. 2.3):

$$[CO_2(aq)] = K_0(T, S) \cdot pCO_2, \qquad (2.3)$$

where $[CO_2(aq)]$ is the concentration of aqueous CO_2, pCO_2 is the partial pressure of CO_2 in the air and K_0 is the solubility coefficient of CO_2 in seawater.

The uptake of atmospheric CO_2 by the ocean occurs only when the partial pressure of CO_2 in the atmosphere, pCO_2, is greater than the equilibrium partial pressure of CO_2 in the surface ocean, PCO_2. In contrary, when the pCO_2 (atm) is lower than the PCO_2 (ocean), for example in the case of an upwelling region where a large amount of CO_2-rich deep water is brought to the surface layer, there is a net transfer of CO_2 from the ocean to the atmosphere. In equilibrium, the net exchange of CO_2 between ocean and atmosphere is zero (*Zeebe and Wolf-Gladrow*, 2001).

2.1.3   The mixed layer and its processes

The mixed layer is defined as the ocean surface layer in which water mass properties of both temperature and salinity (density) are more or less constant. The mixed-layer depth (MLD) depends strongly on the wind forcing that induces mechanical turbulence in the Ekman layer and buoyancy forcing which is controlled by net surface heating/cooling (Q_{net}) and precipitation minus evaporation (P-E) processes (*Denman*, 1973). The MLD varies seasonally and with latitude (*Falkowski*, 1994). The MLD shows a weak seasonal variability in low latitudes and strong seasonal variability in mid to high latitudes (*Kara et al.*, 2003; *de Boyer Montégut et al.*, 2004). The variation in mixed layer depth is an important process that controls the exchange of heat and carbon at the interface of ocean and atmosphere (*Sallée et al.*, 2010a). The seasonal cycle of mixed layer depth influences biological production as it controls light and nutrient availability (*Falkowski*, 1994; *Longhurst*, 1995; *Polovina et al.*, 1995; *Sallée et al.*, 2010a). Seasonal variations in the MLD play a crucial role on the development and timing of phytoplankton blooms in the ocean (*Sverdrup*, 1953; *Behrenfeld*, 2010).

The critical depth hypothesis (Sverdrup theory)   According to the critical depth hypothesis (*Sverdrup*, 1953), the initiation of phytoplankton blooms depends on the availability of light and is linked to the variation in the MLD. *Sverdrup* (1953) suggests that there exists a critical depth in the ocean at which the total production of organic matter by the phytoplankton is equal to loss terms by respiration (Figure 2.2a). If phytoplankton cells are mixed over depth larger than the critical depth, the phytoplankton production is less than the net loss of phytoplankton biomass. In contrast, when the mixed layer depth shoals beyond the critical depth, phytoplankton production exceeds the net loss of biomass and can initiate a phytoplankton bloom in the presence of sufficient light (Figure 2.2b).

Dilution recoupling hypotheis (Behrenfeld, 2010)   *Behrenfeld* (2010) argued that a phytoplankton bloom starts already in winter when the mixed layer is deepest which coincides with the decrease in zooplankton concentration. This argument is contrary to the Critical Depth Hypothesis of Sverdrup who suggested that the bloom starts in spring when the MLD shoals. *Behrenfeld* (2010) argued that the deepening of the MLD during winter favours the replenishment of the surface ocean with essential nutrients for bloom formation and dilutes zooplankton cell density.
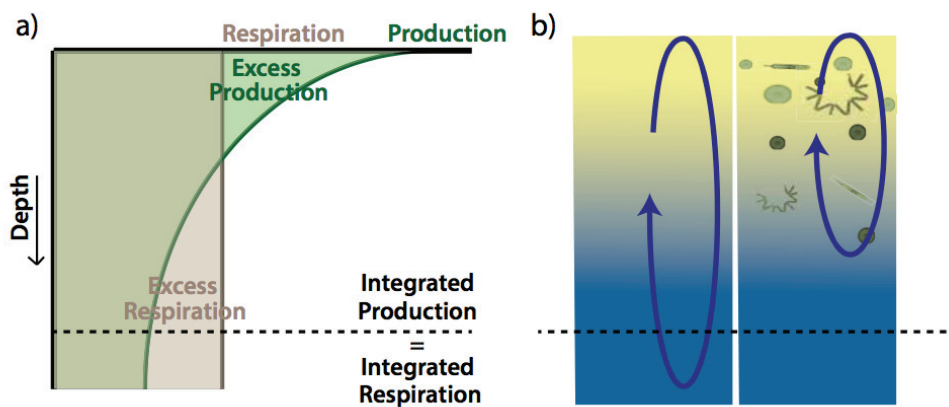
Figure 2.2: Schematic depiction of Sverdrups Critical Depth Hypothesis (a, b). (a) Production is governed solely by light and thus declines exponentially with depth, while loss/respiration is constant with depth. The critical depth is the bottom of the layer within which the integrated production equals integrated respiration (dashed line). (b) When mixing is deeper than the critical depth, there is net loss, so a bloom is not expected (left ellipse); if the mixing depth is shallower than the critical depth, there is excess production and a bloom can occur (right ellipse). Figure taken from *Fischer et al.* (2014).

2.2   Hydrography and water mass circulation
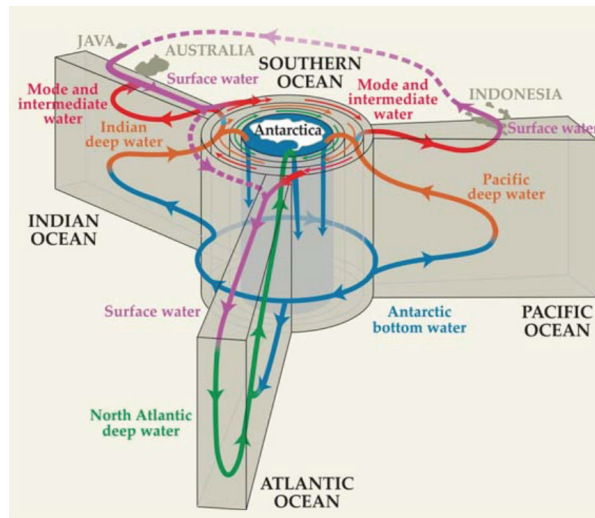
Figure 2.3: Schematic Meridional Overturning Circulation adapted from *Talley* (2013) by *Morrison et al.* (2015).
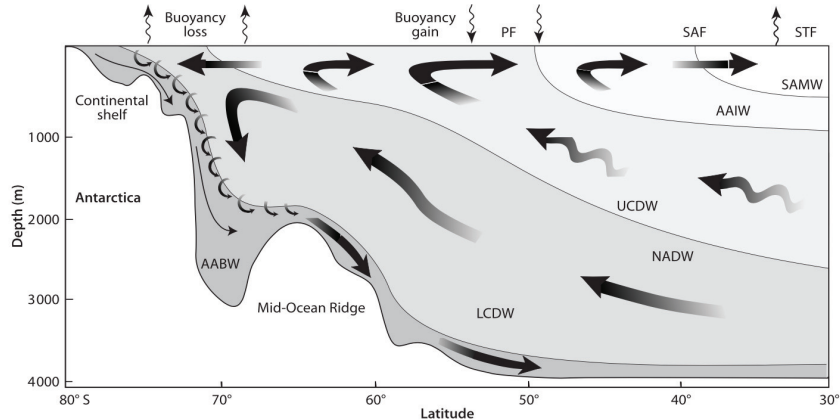
Figure 2.4: Schematic of the two-cell meridional overturning in the Southern Ocean. The upper cell is primarily formed by northwards Ekman transport and gyre transport of surface water, Antarctic Intermediate Water (AAIW) and Subantarctic Mode Water (SAMW). The lower cell is primarily driven by dense water formation near the Antarctic continent with a northwards transport of Antarctic Bottom Water (AABW). Both cells are fed by the southwards transport of Circumpolar and North Atlantic Deep Waters (NADW), which is partly achieved by eddy transport. The Antarctic Polar Front is denoted by PF, the Subantarctic Front by SAF and the Subtropical Front by STF (reproduced from *Speer et al.* (2000) by *Williams and Follows* (2003). Figure taken from *Williams and Follows* (2003).

2.2.1   The role of the Southern Ocean for the global meridional overturning circulation

The Southern Ocean (SO) is commonly considered as that part of the Southern Hemisphere ocean region south of the Subtropical Front (approximately at 40°S) to the Antarctic continent. The SO contains the largest current of the worlds ocean, the so-called Antarctic Circumpolar Current (ACC). The ACC is the longest (24,000 km; *Whitworth III*, 1988) and strongest ocean current with a mean volume transport of 136 Sv as measured across the Drake Passage (*Cunningham et al.*, 2003). The ACC flows eastwards around Antarctica and is controlled by strong westerlies. The energy transfer by westerlies to the SO represents about 70% of the total wind energy transfer to the global ocean, making the SO a highly mixed ocean (*Wunsch*, 1998). The ACC consists of multiple jets or frontal filaments associated with particular streamlines (*Sokolov and Rintoul*, 2007; 2009a). The path, width, and intensity of the fronts are strongly influenced by the bottom topography, mean flow and eddy fields (*Sokolov and Rintoul*, 2007; 2009a). Of all ocean currents, the ACC is the only current that connects all major ocean basins (Atlantic, Pacific, and Indian Ocean), as well as the surface and deep waters in the global overturning circulation (Figure 2.3; *Talley*, 2013; *Sloyan and Rintoul*, 2001). This connection is mediated through the wind-induced upwelling (*Marshall and Speer*, 2012).

The main driver of the global overturning circulation is wind forcing (*Wunsch*, 1998; *Lozier*, 2010). Strong winds-stress curl leads to a large-scale upwelling of carbon- and nutrient rich upper-circumpolar deep water (UCDW; *Whitworth and Nowlin*, 1987) in the Southern Ocean (Figure 2.4; *Talley*, 2013). A part of the upwelled UCDW warms as it gets transported northwards across the Antarctic Circumpolar Current (ACC) driven by wind-induced northward Ekman transport (*Marshall and Speer*, 2012). A fraction of UCDW reaching the Polar Front and the Subantarctic zones sinks to the lower thermocline and flows northward as Antarctic Intermediate Water (AAIW) and Subantarctic Mode Water (SAMW) and forms the upper circulation cell of the global overturning circulation (*Talley*, 2008). About 8 Sv of SAMW and AAIW flow across 30°S (*Talley*, 2013). Another fraction of the upwelled UCDW together with the upwelled North Atlantic Deep Water (NADW) is transported southwards, cools and becomes saltier as a result of brine rejection during sea-ice formation and sinks along the continental shelf to ultimately form Antarctic Bottom Water (AABW; *Marshall and Speer*, 2012; *Talley*, 2013). The AABW flows northwards out of the Southern Ocean in the bottom layers and forms the lower cell of the overturning circulation (*Marshall and Speer*, 2012; *Talley*, 2013). The meridional overturning circulation not only brings deep water and nutrients up to the surface (in the Southern Ocean), but it also carries surface water down, and distributes heat and

carbon dioxide as it flows through the worlds oceans (*Marshall and Speer*, 2012; *Talley*, 2013). About 80% of the deep cold waters resurface in the Southern Ocean south of 58°S (*Lumpkin and Speer*, 2007; *Talley*, 2013). This highlights the importance of the Southern Hemisphere overturning circulation (large scale upwelling) in regulating the global climate system.

2.2.2   Southern Ocean mixed layer

The surface mixed layer in the SO shows a strong seasonal variation (*Kara et al.*, 2003; *de Boyer Montégut et al.*, 2004). Between 45 and 60°S very deep MLDs occur in austral winter (MLD>300 m), and even the minimum MLD, in summer, is with 70 m quite deep (*Rintoul and Trull*, 2001). The regions with deepest MLD during winter are located north of the ACC in the Pacific and Indian sectors (*Dong et al.*, 2008). During spring and summer the deepest MLDs occur in the ACC region. The MLD seasonal cycle is, however, weaker south of 60°S. It varies from 30 m in summer to values of nearly 100 m in winter (*de Boyer Montégut et al.*, 2004). The shoaling of the MLD during spring and summer is due to the increase in solar radiation that increases surface water stratification. During autumn and winter the deepening of the winter mixed layer is mainly caused by the surface cooling, wind stress forcing (turbulent mixing or entrainment) and other processes such as the advection and diffusion of heat into the mixed layer (*Kang et al.*, 2010). The accurate determination of the depth of the mixed layer in the Southern Ocean is more challenging than in lower latitudes where the ocean is strictly temperature stratified (*Dong et al.*, 2008) whereas in the Southern Ocean temperature inversion occurs and salinity plays a major role in the surface water stratification (*de Boyer Montégut et al.*, 2004; *Dong et al.*, 2008; *Holte and Talley*, 2009). Different criteria are used to define the depth of the mixed layer in the SO. Temperature/density-based criteria, difference criteria, gradient criteria and hybrid methods (*Brainerd and Gregg*, 1995; *Wijesekera and Gregg*, 1996; *Obata et al.*, 1996; *Monterey and Levitus*, 1997; *Holte and Talley*, 2009; *de Boyer Montégut et al.*, 2004; *Dong et al.*, 2008) have been proposed. In the difference-based criteria, the MLD is defined as the depth where the oceanic property has changed from a reference surface value by a constant amount (e.g., *de Boyer Montégut et al.*, 2004), whereas, in the gradient-based criteria, the MLD is defined as the depth where the vertical gradient of the property equals or exceeds a threshold value (e.g., *Lorbacher et al.*, 2006). Previous studies have shown that the MLD based on difference criteria is realistic compared to the one estimated from the gradient method (*Kara et al.*, 2000; *de Boyer Montégut et al.*, 2004; *Holte and Talley*, 2009; *Dong et al.*, 2008). *Thomson and Fine* (2003) found that the threshold methods can better approximate the true mixed layer depth, whereas the integral and regression methods typically compute the depth of the underlying pycnocline. *Holte and*

Talley (2009), using a hybrid method to construct MLD in the Southern Ocean, showed that density criteria are relatively robust but criteria based on temperature alone are inadequate in the presence of strong salinity stratification. In general, the threshold methods find deeper MLDs compared to the hybrid method and the gradient methods produce more anomalous MLDs (*Dong et al.*, 2008). The most common density difference criterion used is 0.03 kg m^{-3} with a reference depth of 10 m (*de Boyer Montégut et al.*, 2004). The 10 m reference depth is chosen to avoid the representation of diurnal cycle mixing layer rather than the mixed layer. The 0.03 kg m^{-3} density criterion is used in this thesis.

2.2.3   Subduction processes

Water mass formation in the SO is volumetrically dominated by the formation of mode and intermediate waters (SAMW and AAIW) that occur in the Polar Frontal Zone (PFZ) and the Subantarctic Zone (SAZ; *Talley*, 2013). Subduction of water masses and carbon sequestration (natural and anthropogenic) are tightly coupled (*Marshall et al.*, 1993; *Sallée et al.*, 2010b; *Lee et al.*, 2011; *Trossman et al.*, 2012). The subduction rate of water masses into the permanent thermocline at the base of the winter mixed layer is driven by horizontal and vertical transport (*Marshall et al.*, 1993). In the annual mean, the maximum transfer of water fluxes into the permanent thermocline occurs during late winter and early spring when the mixed-layer shoals. The shoaling of the mixed layer leads to increased stratification in the mixed layer with denser water at the base of the mixed layer that irreversibly sinks to the stratified permanent thermocline (*Marshall et al.*, 1993). The net subduction rate is the residual of the Eulerian-mean and eddy contributions (*Marshall*, 1997). This suggests that eddy formation significantly affects the water mass subduction rate in the Southern Ocean (*Morrison and Hogg*, 2013). Horizontal advection is the main physical mechanism that controls the subduction processes in the Southern Ocean (*Downes et al.*, 2009; 2010; *Sallée et al.*, 2010b). The horizontal advection is also known as lateral induction (*Marshall et al.*, 1993). Other mechanisms such as vertical diffusion, entrainment and eddy mixing might as well play an important role in the physical transfer of water mass properties from the mixed layer to the ocean interior (Figure 2.5; *Bopp et al.*, 2015; *Sallée et al.*, 2012; *Langlais et al.*, 2017).

Of the large amount of the anthropogenic carbon that is taken up in the Southern Ocean (south of 30°S; *Sabine et al.*, 2004; *Gruber et al.*, 2009; *Khatiwala et al.*, 2009), about 56% of this anthropogenic carbon is sequestered in the Antarctic Intermediate Water(AAIW) and Subantarctic Mode Water (SAMW) mode waters (*Langlais et al.*, 2017). The transport of the anthropogenic carbon to the ocean interior is also reinforced by the sinking of cold dense shelf waters along the margins of Antarctica (*van Heuven et al.*,

2014). By these processes, a large amount of anthropogenic carbon from the surface is stored in the deeper layers of the ocean for time scales of decades to hundreds of years (*Archer et al.*, 1997). The main hotspots of carbon transfer occur along the path of the ACC (*Sallée et al.*, 2010b; *Lévy et al.*, 2013; *Langlais et al.*, 2017). Coarse models with eddy parameterizations forced by the pre-industrial atmospheric CO_2 concentration suggest that the subduction of carbon in the ACC region is mostly driven by vertical advection and partially compensated by local eddy mixing effects (*Lévy et al.*, 2013). This suggests that mesoscale circulation plays an important role for the variation in carbon subduction. Furthermore, *Sallée et al.* (2012) found that subduction of anthropogenic carbon occurs in some specific locations resulting from the interaction between wind-driven Ekman transport, eddy fluxes and variations in mixed-layer depth. They also found that north of the ACC the subduction of anthropogenic carbon is more zonally-symmetric and controlled by the northward Ekman transport. Eddies contribute to partially compensate the effect of the Ekman transport, with subduction in and south of the ACC (*Sallée et al.*, 2012). The rate of subduction of carbon depends on the variations of the winter mixed-layer depth and the mean lateral flow at the base of the mixed layer (*Karleskind et al.*, 2011; *Sallée et al.*, 2012). Recent high-resolution eddy model analysis suggests that the subduction of anthropogenic carbon in the Southern Ocean is dominantly driven by the mesoscale stationary Rossby waves generated where the ACC interacts with the bottom topography (*Langlais et al.*, 2017). *Langlais et al.* (2017) found that anthropogenic carbon subduction in the SAMW and AAIW density classes is dominated by the horizontal advection that dominates over vertical subduction and small eddy contribution (about 13%). In contrast to advection suggested to be the main physical process for subduction of anthropogenic carbon from the studies cited above, *Bopp et al.* (2015), using a coarse model simulation, highlight that vertical diffusion is the main physical process that controls anthropogenic carbon subduction in the Southern Ocean. *Bopp et al.* (2015), however, define subduction across the base of the seasonally varying mixed layer which differs from the definition used by the other studies cited above. All these findings suggest there is still lack of agreement on the main physical process that controls total (natural and anthropogenic) carbon subduction in the Southern Ocean. Further studies are needed with high-resolution data from observations to shed light on the main physical mechanism of anthropogenic carbon subduction in the Southern Ocean.
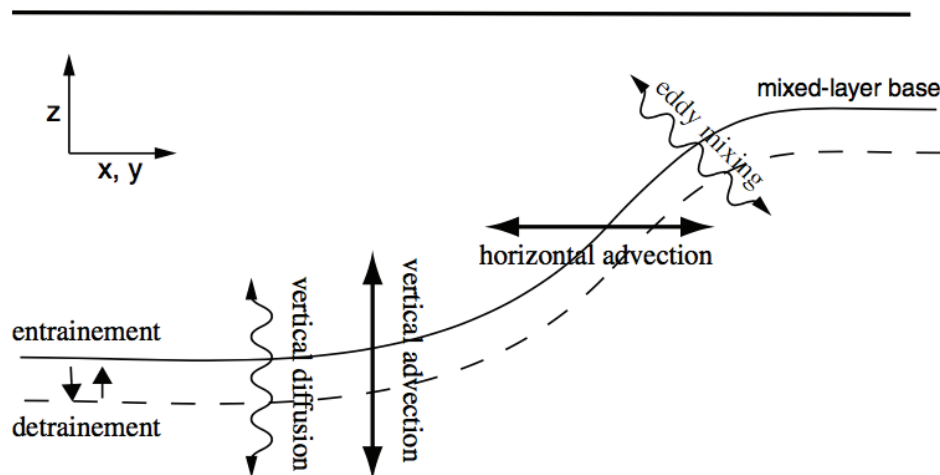
Figure 2.5: Schematic figure indicating the main processes contributing to physical transfer across the base of the mixed-layer (adapted from *Lévy et al.* (2013)).

2.3   Southern Hemisphere climate variability and change

2.3.1   Atmospheric change

Climate variability in the Southern Hemisphere from high to very low frequency are mostly related to the Southern Annular Mode (SAM; *Thompson et al.*, 2011). Over the past few decades, there is evidence for a positive trend in the Southern Annual Mode (*Thompson and Solomon*, 2002; *Marshall*, 2003; *Thompson et al.*, 2011; *Abram et al.*, 2014). This is due to the constant increase in the concentration of greenhouse gases in the atmosphere by human activities and stratospheric ozone depletion over Antarctica (*Thompson et al.*, 2011; *Lee and Feldstein*, 2013; *Abram et al.*, 2014). The long-term reconstruction of the SAM index using proxy data shows a steady SAM index (*Villalba et al.*, 2012) or declining (*Abram et al.*, 2014) SAM trend since 1800, reaching its minimum in 1950. Since then, a positive trend in the SAM index has been observed (Figure 2.6; *Marshall*, 2003; *Thompson et al.*, 2011). The positive trend in SAM has led to an anomaly, i.e. an intensification of westerlies and their poleward shift over the recent decades (*Thompson et al.*, 2011). Increased surface wind stress in the SO in response to a positive trend in SAM has induced significant changes in ocean circulation and biogeochemistry of this region.
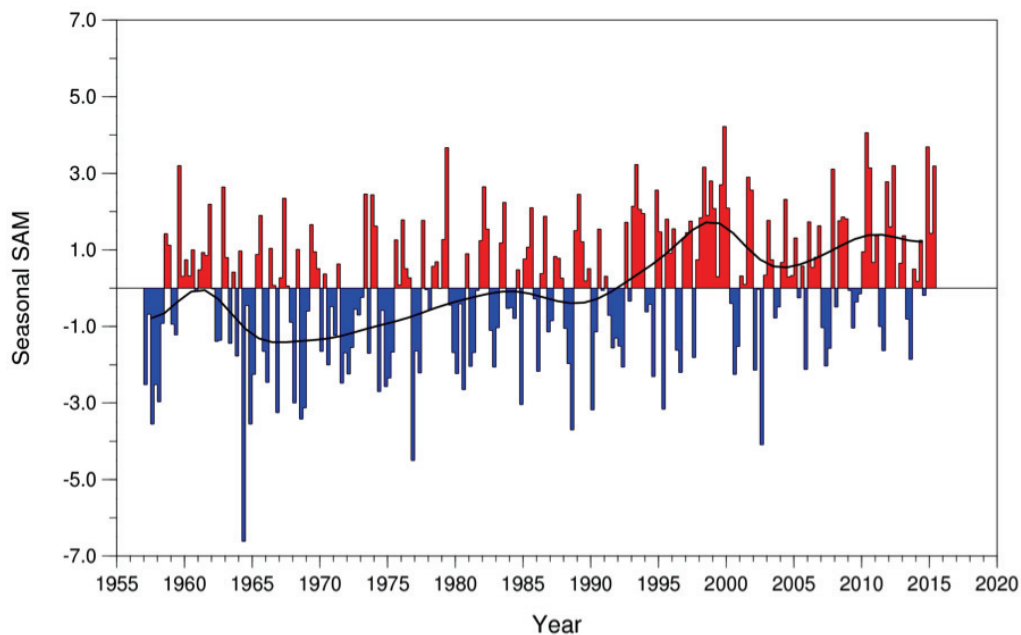
Figure 2.6: Seasonal (monthly mean) values of the observation-based SAM index. The smooth black curve shows decadal variations. Marshall's Southern Annular Mode index is calculated based on the difference in station sea-level pressure between 40°S and 65°S. Figure taken from https://climatedataguide.ucar.edu/climate-data/marshall-southern-annular-mode-sam-index-station-based.

2.3.2 Changes in ocean circulation and mixing

Over the last decades, significant changes have occurred in the Southern Ocean surface climate (*Jones et al.*, 2016b). The most conspicuous large-scale change over recent decades is the freshening and subsurface warming of the Southern Ocean (*Gille*, 2008; *Schmidtko et al.*, 2014; *Rye et al.*, 2014). Warming of the subsurface ocean in this region is the result of the recent increase in heat uptake in response to the increase in the atmospheric temperature (*Gille*, 2008; *Levitus et al.*, 2012; *Fahrbach et al.*, 2011; *England et al.*, 2014). Most observed warming is concentrated within the ACC (*Gille*, 2002; 2008). Part of the heat was transported and stored in abyssal oceans (e.g., the Weddell Gyre, *Fahrbach et al.*, 2011). Other channels of heat transport from the surface to the ocean interior is through the formation of mode and intermediate waters driven by the stronger northward Ekman transport (*England et al.*, 2014; *Downes et al.*, 2011). The freshening observed in the Southern Ocean is related to transport of melt water from the coastal zone to the open ocean controlled by wind forcing (*Holland and Kwok*, 2012; *Haumann et al.*, 2014; 2016) which led to freshened surface and intermediate waters (*Durack et al.*, 2012; *Helm et al.*, 2010). The increase in atmospheric precipitation over evaporation has also contributed

to the surface freshening in the SO over the last decades (*Durack et al.*, 2012).

The atmospheric forcing has induced regional cooling of the sea surface (*England et al.*, 2014; *Jones et al.*, 2016b). The strongest cooling signal in sea surface temperature occurred in the Pacific sector (*England et al.*, 2014; *Jones et al.*, 2016b). The persistent cooling observed in the South Pacific has contributed to the slow-down of the global atmospheric warming effect (*Jones et al.*, 2016b). Also, there is a positive trend in the Antarctic sea-ice extent (*Turner et al.*, 2015; *Jones et al.*, 2016b) though with regional variability. The cause of the recent hemispheric scale positive trend in sea-ice is still not fully understood, but the changes in the atmospheric circulation have been proposed as potential drivers (*Turner et al.*, 2015; *Haumann et al.*, 2014). Changes in sea-ice melting are expected to increase open ocean stratification (more freshening) and as a consequence the MLD will decrease. The positive trend in SAM in this region also leads to large-scale anomalies in the MLD that are zonally asymmetric (*Sallée et al.*, 2010a).

The recent increase in wind stress in the SO has induced a poleward shift and small increase in the ACC intensity controlled by the balance between the changes in eddies formation and Eulerian mean flow (*Hogg et al.*, 2008; *Böning et al.*, 2008; *Hallberg and Gnanadesikan*, 2006; *Farneti and Delworth*, 2010; *Farneti et al.*, 2010; *Downes et al.*, 2011). Increased wind forcing also leads to more subduction of SAMW and AAIW in the Southern Ocean as suggested by a model simulation (*Downes et al.*, 2011). In fact, an increase in surface wind stress in the ACC region leads to an elevated northward Ekman transport of upwelled cool surface waters across the ACC, followed by a deepening in winter mixed layer, and consequently to increased subduction rates of AAIW and SAMW north of the APF and SAF. Furthermore, a model sensitivity study showed that an increase in the Southern Ocean wind stress enhances the upper cell of the overturning circulation fed by the increase of potential energy delivered by the stronger upwelling of cold deep waters (*Hogg et al.*, 2017). This result is in contrast to the suggested decrease in the upper ocean overturning circulation by *DeVries et al.* (2017) in the 2000s. However, *Hogg et al.* (2017) showed that the effect of stronger winds could be opposed by the poleward shift and the overall result would depend on the pattern of wind change.

The response of the Southern Ocean upper ocean circulation to the positive trend in SAM is immediate and not lagging in time (*Hauck et al.*, 2013). In contrast, the effect of the positive trend in SAM on the deep layer circulation of the Southern Ocean is lagging in time. On longer-time scales, the increase in westerly winds enhances eddy kinetic energy and leads to a poleward heat flux transport and, thereby, increases ocean warming south of the APF (*Hogg et al.*, 2008; *Screen et al.*, 2009). In fact, increased wind stress in the SO has enhanced eddy formation and their kinetic energy in the ACC region with little significant impact on the ACC volume transport (*Meredith and Hogg*, 2006; *Hogg*

et al., 2008). The relationship between changes in wind stress and eddy kinetic energy is almost linear (*Morrison and Hogg*, 2013) but the full wind forcing effect on the eddy activity is lagged in time, 2-3 years after a positive anomaly in the SAM index (*Meredith and Hogg*, 2006). This is explained by the fact that surface wind stress needs more time to perturb the deep circulation (*Meredith and Hogg*, 2006). Furthermore, the southward flow induced by eddies leads to partial compensation of the northward Ekman transport of the surface waters confined within the Ekman layer (*Hughes and Ash*, 2001; *Meredith et al.*, 2012; *Morrison and Hogg*, 2013; *Hogg et al.*, 2017).

2.3.3 Changes in biogeochemistry

In the Southern Ocean, the carbon sink appears to have decreased from the 1980s to the early 2000s (*Le Quéré et al.*, 2007; *Zickfeld et al.*, 2008; *Le Quéré et al.*, 2009) explained by the increase in more upwelling of natural CO_2 in response to the increase of the westerlies (*Le Quéré et al.*, 2007; *Lovenduski et al.*, 2008). Since 2002, the SO has now experienced a reinvigoration of the carbon sink (*Landschützer et al.*, 2015; *Rödenbeck et al.*, 2015). The temperature-driven effects on the solubility of CO_2 is identified as a regional driver (*Landschützer et al.*, 2015; *Rödenbeck et al.*, 2015). Nevertheless, an ocean inversion model study suggests that the recent increase in the SO CO_2 uptake could largely be explained by the decrease in upper ocean circulation in this region since the 2000s (*DeVries et al.*, 2017). Decreased upper-ocean overturning circulation leads to less upwelling of natural carbon-rich deep waters. It is, however, not clear, how the overturning circulation could have slowed while the SAM index and westerly winds keep increasing (Figure 2.6). In this respect, a full explanation on the recent reinvigoration of the Southern Ocean carbon sink is lacking. At basin scale, significant variability in the carbon and nutrient concentration was observed both in surface and bottom layers. This was suggested to be linked to changes in circulation in response to a positive trend in SAM, which leads to increased upwelling of subsurface water and their subduction north of the ACC into deeper layers (*Tanhua et al.*, 2017; *Salt et al.*, 2015; *Ayers and Strutton*, 2013; *van Heuven et al.*, 2011; 2014; *Hoppema et al.*, 2015; *Panassa et al.*, 2018). All these observations suggest that the positive trend in the SAM has restructured the ocean circulation of this region, and, as a consequence, induced significant changes in the biogeochemistry system of this region.

2.4   Future change

2.4.1   Atmospheric change

The atmospheric inventory of CO_2 has increased by about 30% since the beginning of the industrial era (around 1750) and is still expected to steadily rise as the CO_2 emissions are increasing (according to business-as-usual scenarios). Based on the representative concentration pathways (RCPs) defined in the Intergovernmental Panel on Climate Change fifth assessment report (IPCC AR5), atmospheric CO_2 emission growth could result in an atmospheric CO_2 concentration of 480 ppm (RCP2.6) or >1000 ppm (RCP8.5) by 2100. Such changes will intensify the global warming effect in the Southern Ocean and elsewhere. In the future, the Antarctic ozone layer is expected to recover but the forcing by greenhouse gases will still increase. This will likely further drive the positive trend observed in SAM (*Thompson et al.*, 2011). A more positive SAM index in the future is predicted to shift SO westerly winds polewards and to intensify them with a probable strong effect during summer season (*Thompson et al.*, 2011; *Fyfe and Saenko*, 2005; *Kushner et al.*, 2001; *Cai et al.*, 2005). The projected poleward-intensification of westerly winds together with the global warming is expected to drive significant changes in the circulation, heat and carbon fluxes and biogeochemistry of this region.

2.4.2   Changes in ocean physics

By the end of the twenty-first century, coarseresolution models of the Coupled Model Intercomparison Project 5 (CMIP5) project that under global warming scenarios (increased westerlies, warming, and freshening), the Southern Ocean will experience a warming and freshening of intermediate waters driven by sea-ice melting and, as a consequence, will reduce the upper 2000 m water density (Figure 2.7, *Meijers*, 2014). This will increase surface water stratification and shoal the mixed layer and as a consequence decrease the bottom, mode and intermediate water formation rates (*Downes et al.*, 2009; 2010; *Meijers*, 2014). The projected decrease in the SAMW and AAIW subduction rate will probably reduce the transfer rate of anthropogenic carbon along with residual nutrients from the surface ocean to the deep ocean. This might affect the low latitude primary productivity (*Sarmiento et al.*, 2004; *Palter et al.*, 2010; *Holzer and Primeau*, 2013). In contrast to the projected freshening of the intermediate waters, bottom waters are expected to become more saline (*Meijers*, 2014). Even though the wind stress in the SO is expected to increase by 20% at the end of the twenty-first century, the ACC transport is insensitive to this effect, rather a decrease in ACC volume transport is projected and linked to the increase in the freshwater fluxes and surface heat in the ACC region (*Downes and Hogg*,

2013). In contrast, the future increase in the surface wind stress in tandem with heat gain in the surface ocean are expected to strengthen the upper-ocean overturning circulation, whereas the lower cell (deep circulation) is projected to weaken (*Downes and Hogg*, 2013; *Meijers*, 2014). Also in the future, we may expect changes in the SO overturning circulation to be partially compensated by eddy activity (*Downes and Hogg*, 2013; *Meijers*, 2014). Furthermore, a poleward shift of subtropical gyres is also expected under the future climate by the end of the twenty-first century (*Meijers*, 2014).
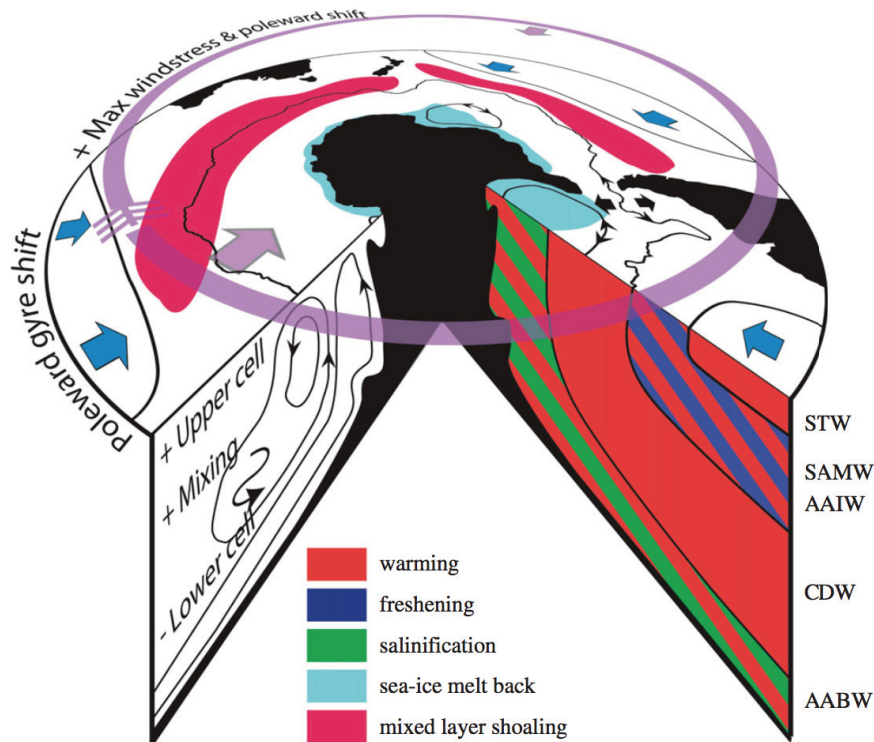
Figure 2.7: Schematic showing the impact of climate forcing in CMIP5 models in the Southern Ocean by the end of the twenty-first century. See text for more details. Arrows in both directions for the ACC and subpolar gyres indicate significant changes in the transport of both signs within the model ensemble. Figure taken from *Meijers* (2014).

2.4.3 Changes in biogeochemistry

Future poleward-intensified westerly winds in the Southern Ocean under global warming scenarios are projected to strongly increase anthropogenic carbon dioxide and heat uptake in this region (*Russell et al.*, 2006). This is driven by the increase in wind-driven upwelling of cold deep waters that lead to enhancing anthropogenic CO_2 solubility and favour heat uptake. By the end of the 21st century most of CMIP5 simulations project that the Southern Ocean will highly acidify and experience probably a medium or severe decrease in

subsurface oxygen, and a mixed response (spots of increase and decrease) in NPP with an integrated slight increase in NPP (*Bopp et al.*, 2013). The increase in NPP is driven by the increase in light availability. The increase in ocean acidification is caused by the increase in atmospheric CO_2. Southern Ocean surface waters are expected to become undersaturated with respect to aragonite during the 21st century (*Orr et al.*, 2005; *Bopp et al.*, 2013). Deoxygenation results from ocean warming (reduced oxygen solubility). Furthermore, by the end of the 21st century, the biological carbon pump (export production) in the SO is expected to increase during the summer season (*Laufkötter et al.*, 2015; *Hauck et al.*, 2015). This might to some extent draw down anthropogenic CO_2 in the atmosphere and lead to changes in the Revelle factor (*Hauck and Völker*, 2015). In the future, we may expect biology to contribute more to the total CO_2 uptake in the Southern Ocean (*Hauck and Völker*, 2015).

2.5   Outline of the thesis

The combined effects of stratospheric ozone depletion over Antarctica, driven by chlorofluorocarbon (CFC) emissions, and the increase in greenhouse gases lead to an unprecedented perturbation of the Southern Hemisphere atmospheric circulation characterized by a positive trend in the Southern Annular Mode (SAM; *Marshall*, 2003; *Thompson et al.*, 2011). The positive trend in SAM is projected to continue and to become stronger during the summer season (*Thompson et al.*, 2011). As a characteristic of the positive trend in SAM, westerly winds are strengthening and shifting poleward (*Thompson et al.*, 2011).

Increased westerly winds could enhance the upwelling of the cold and nutrient-rich deep waters driven by the Ekman divergence in the ACC region. Increased northward Ekman transport of the upwelled water across the ACC could enhance the subduction rate of upwelled waters north of the Antarctic Polar Front and the Subantarctic Front as intermediate and mode waters (*Downes et al.*, 2011; *Hauck et al.*, 2013). This results from the interplay between the mixed layer deepening and increase in current flow (*Marshall et al.*, 1993; *Sallée et al.*, 2010b). Enhanced subduction of intermediate and mode waters will significantly fuel the low latitude primary productivity and impact the carbon cycle on longer time scales (*Sarmiento et al.*, 2004; *Marinov et al.*, 2006; *Palter et al.*, 2010; *Holzer and Primeau*, 2013). Enhanced wind-induced mixing could lead to an increase in nutrient concentration in the surface layer, but could as well lead to a dilution of phytoplankton concentration by bringing them into deeper layers where light is a limiting factor (*Sverdrup*, 1953; *Behrenfeld*, 2010). In addition to the wind signal, that would lead to more mixing in the Southern Ocean, there is the global warming effect. Increased ocean warming would lead to more surface water stratification and less mixing. This will

affect the efficiency of nutrient cycling in the water column and, as a consequence, could limit the phytoplankton productivity caused by the shoaling of the mixed layer. There is already some evidence from observations of Southern Ocean warming that is confined mostly to the intermediate layers (*Gille*, 2002; 2008). While the subsurface waters are warming, model and observational studies revealed a surface cooling that is induced by the strengthening of the surface wind stress over the last decades (*Capotondi et al.*, 2012; *England et al.*, 2014). Based on analysis of annual mean data, the strengthening of wind forcing over the last two decades has induced a zonally asymmetric response of the mixed layer depth (*Sallée et al.*, 2010a). What is lacking in the literature is an overview on the effect of changes in the seasonal wind forcing along with global warming effects on the seasonal mixed layer dynamics. The summer season is of particular interest because of biological production and its impact on oceanic CO_2 uptake.

How do circulation changes impact cycling of carbon and nutrients locally in the SO? How do atmospheric circulation changes in the Southern Hemisphere alter the mixed layer dynamics? How does that affect the physical transport rate of carbon and nutrients from high to low latitudes? These are the main research questions I attempt to answer in this PhD thesis.

Most of the studies that investigated the effect of the change in atmospheric circulation on the physical, biological and biogeochemical feedbacks in the SO were based on model studies (*Lovenduski et al.*, 2008; *Hauck et al.*, 2013). Only few studies, that used the satellite observations with relatively short time series, investigated the impact of the positive trend in SAM on the Southern Ocean circulation and biology (*Lovenduski and Gruber*, 2005) but so far, no comprehensive in-situ data were explored. This is because observations are sparse in this region. Since the last two decades the number of observational (cruise, Argo floats) data of hydrographic and biogeochemistry have grown, making possible the quantification of the interannual variability of ocean properties and ocean circulation in this region.

Recent studies based on the repeat section data have revealed substantial changes in the biogeochemistry of intermediate and mode waters in the Indian, Australian and Pacific sectors of the Southern Ocean (*Iida et al.*, 2013; *Ayers and Strutton*, 2013; *Pardo et al.*, 2017). All these observations suggest that the upwelling in the Southern Ocean has intensified in response to the wind forcing driven by a positive trend in SAM, and, as a consequence, has enhanced subduction north of the Antarctic Polar Front. What is still missing is a solid understanding of how the recent change in circulation related to a positive trend in the SAM did affect the biogeochemistry of intermediate waters in the Atlantic sector of the Southern Ocean.

The aim of this thesis is to enhance our understanding of the relative effects of the

recent changes in atmospheric forcing on the Southern Ocean circulation and their link to the biogeochemistry from observations and by a combination with simulations using a biogeochemical ocean general circulation model (BOGCM).

In Publication I (chapter 3), I investigate interannual to decadal variability of carbon and nutrients in the Antarctic intermediate water (AAIW) and discuss the potential drivers in the Atlantic sector of the Southern Ocean based on cruise data. Publication II (chapter 4) takes advantage of the growing number of in-situ temperature and salinity profile data in the SO since 2000 (Argo program) in combination with a BOGCM to study the sensitivity of the summer mixed layer depth variability to recent atmospheric forcing. In Publication III (chapter 5), I use the output from a BOGCM to investigate the impact of SAM variability and trend on the volume, carbon and nutrient transports via subduction across the base of the winter mixed layer in the Southern Ocean on interannual timescales. In the last chapter (chapter 6), a general discussion and conclusion of the dissertation is provided. In this chapter, the results of the previous chapters (3, 4 and 5) are placed into the context of the previously existing literature.

2.6 List of publications and declaration of own contribution

Publication I: Essowè Panassa, J. Magdalena Santana-Casiano, Melchor González-Dávila, Mario Hoppema, Steven M.A.C van Heuven, Christoph Völker, Dieter Wolf-Gladrow, Judith Hauck (2018): Variability of nutrients and carbon dioxide in the Antarctic Intermediate Water between 1990 and 2014. *Ocean Dynamics, 68(3), pp. 295-308, doi:10.1007/s10236-018-1131-2*

I have initially designed the study and adjusted it according to the co-authors' comments. I performed the analysis of the data. I drafted the manuscript and incorporated the co-authors' comments.

Publication II: E. Panassa, C. Völker, D. Wolf-Gladrow, and J. Hauck: Drivers of interannual variability of summer Mixed Layer Depth in the Southern Ocean between 2002-2011. *In review at Journal of Geophysical Research: Oceans*

I planned and performed the analysis of the observations and I planned the sensitivity experiments under the supervision of Judith Hauck and Christoph Völker. I investigated the availability of data sets and acquired the data. I prepared the model forcing fields and analyzed the model output. I wrote the manuscript and discussed it with the co-authors.

Publication III: E. Panassa, C. Völker, D. Wolf-Gladrow, and J. Hauck: Interannual variability of carbon and nutrient subduction in the Southern Ocean. *To be submitted to Journal of Geophysical Research: Oceans*

I designed the study, built the subduction rate code, and performed the analysis of the model output. I wrote the manuscript and discussed it with the co-authors.

Chapter 3

Variability of nutrients and carbon dioxide in the Antarctic Intermediate Water between 1990 and 2014

CrossMark

Variability of nutrients and carbon dioxide in the Antarctic Intermediate Water between 1990 and 2014

Essowè Panassa[1] [ORCID] · J. Magdalena Santana-Casiano[2] · Melchor González-Dávila[2] · Mario Hoppema[1] · Steven M.A.C van Heuven[3] · Christoph Völker[1] · Dieter Wolf-Gladrow[1] · Judith Hauck[1]

Abstract

Antarctic Intermediate Water (AAIW) formation constitutes an important mechanism for the export of macronutrients out of the Southern Ocean that fuels primary production in low latitudes. We used quality-controlled gridded data from five hydrographic cruises between 1990 and 2014 to examine decadal variability in nutrients and dissolved inorganic carbon (DIC) in the AAIW (neutral density range $27 < \gamma_n < 27.4$) along the Prime Meridian. Significant positive trends were found in DIC (0.70 ± 0.4 μmol kg^{-1} year^{-1}) and nitrate (0.08 ± 0.06 μmol kg^{-1} year^{-1}) along with decreasing trends in temperature (-0.015 ± 0.01 °C year^{-1}) and salinity (-0.003 ± 0.002 year^{-1}) in the AAIW. Accompanying this is an increase in apparent oxygen utilization (AOU, 0.16 ± 0.07 μmol kg^{-1} year^{-1}). We estimated that 75% of the DIC change has an anthropogenic origin. The remainder of the trends support a scenario of a strengthening of the upper-ocean overturning circulation in the Atlantic sector of the Southern Ocean in response to the positive trend in the Southern Annular Mode. A decrease in net primary productivity (more nutrients unutilized) in the source waters of the AAIW could have contributed as well but cannot fully explain all observed changes.

Keywords Prime Meridian · Antarctic Intermediate Water · Carbon · Nutrients · Decadal variability

1 Introduction

The Southern Ocean (SO) is a key ocean region of the global carbon cycle. Outgassing of CO_2 driven by the upwelling of carbon-rich deep water (Hoppema 2004b) is counteracted by CO_2 draw-down by biological production and by uptake of anthropogenic CO_2 (Metzl et al. 2006; Gruber et al. 2009). The global ocean takes up 30% of the anthropogenic carbon that is released to the atmosphere (Le Quéré et al. 2016). Of those 30%, the SO takes up about 40%, i.e., 12%

✉ Essowè Panassa
   essowe.panassa@awi.de

Extended author information available on the last page of the article.

of total anthropogenic CO_2 emissions (Sabine et al. 2004; Khatiwala et al. 2009). A reduction in the SO uptake of anthropogenic CO_2 in the 1990s was suggested by Wetzel et al. (2005) and Le Quéré et al. (2007) based on ocean and atmosphere inverse models and observations of atmospheric CO_2. The observations were explained by the increase in the westerlies in response to the positive trend in the Southern Annular Mode, leading to more upwelling (Thompson et al. 2011; Marshall 2003). However, in the 2000s, the SO carbon sink has regained its strength (Landschützer et al. 2015). The reinvigoration of the SO carbon sink was suggested to be linked to the weakening of the upper-ocean overturning circulation as revealed by global inverse model analysis (DeVries et al. 2017).

The SO is also the largest high-nitrate low-chlorophyll (HNLC) region. The macronutrients nitrate and phosphate are not utilized completely by the phytoplankton because of iron (Martin et al. 1990; De Baar et al. 1990) and light limitation (Mitchell et al. 1991; Nelson and Smith 1991). These macronutrients are supplied from below by large-scale upwelling. The unused nutrients are advected further north

by Ekman transport. Surface waters which are still rich in nitrate and phosphate are subducted between the Antarctic Polar Front (APF) and the Subantarctic Front (SAF), forming Antarctic Intermediate Water (AAIW) and Subantarctic Mode Water (SAMW, Gordon 1981; Peterson and Whitworth 1989; Talley 1996; Hanawa and Talley 2001). The formation and ventilation of SAMW and AAIW in the SO are crucial for the exchange of water mass properties between high and low latitudes (Rintoul et al. 2001; Talley 2013; Gordon 1981; de las Heras and Schlitzer 1999). The export of nutrients through this pathway may be responsible for the nutrient supply that fuels up to three quarters of the biological export production in the global ocean north of 30°S (Marinov et al. 2006; Sarmiento et al. 2004).

The Atlantic sector of the SO is one of the primary conduits through which high latitude surface, thermocline, and intermediate waters are advected equatorward and further to cold northern Atlantic regions (de las Heras and Schlitzer 1999). The northward transport of surface and intermediate waters in the Atlantic sector of the SO compensates the southward flow of North Atlantic Deep Water (NADW) and Circumpolar Deep Water (CDW) and forms part of the global Meridional Overturning Circulation (Bryden et al. 2005; Wunsch and Heimbach 2006; de las Heras and Schlitzer 1999). The Upper Circumpolar Deep Water (UCDW) upwells in the Antarctic Divergence zone between 55 and 65°S and is characterized by high concentrations of CO_2 and nutrients (Fig. 1; Whitworth and Nowlin 1987). The northward Ekman transport of the resulting surface waters across the Antarctic Circumpolar Current (ACC) reaches its maximum value at about 50°S between the Antarctic Polar Front (APF) and the Subantarctic Front (SAF) (Morrison et al. 2015). Here, subduction leads to the formation of the Antarctic Intermediate Water (AAIW, neutral density of $27 < \gamma_n < 27.4$; Sloyan and Rintoul 2001, Fig. 2). The Subantarctic Mode Water (SAMW, $26.0 < \gamma_n < 26.8$; Sloyan and Rintoul 2001) is produced north of the SAF (Hanawa and Talley 2001). In deeper layers, North Atlantic Deep Water (NADW), a high-saline and low-nutrient water mass flows southward, feeding into the CDW.

South of the Antarctic divergence, Antarctic Surface Water (AASW) flows toward the Antarctic continent where it cools and becomes saltier as a result of brine rejection during sea-ice formation. This loss of buoyancy leads to a sinking of water to the bottom layer where it is known as Weddell Sea Bottom Water (WSBW). Weddell Sea Deep Water (WSDW) is formed partly by sinking of dense shelf waters that mixed with Warm Deep Water (WDW) to intermediate depth and partly by mixing of WSBW with overlying water masses (Rintoul et al. 2001). WSDW is light enough to leave the Weddell Sea and is then spread in the
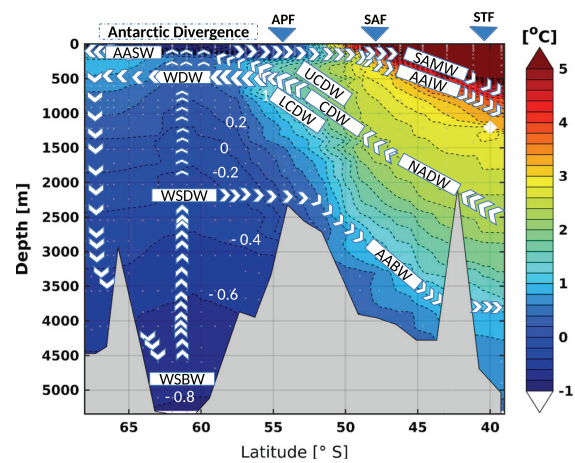
Fig. 1 Section of potential temperature of the cruise ANT-XXX/2 (2014). On the top, we show the schematic representation of the circulation of the water masses along the Prime Meridian south of the Subtropical Front (STF) located at about 40°S, modified from van Heuven et al. (2011). AAIW = Antarctic Intermediate Water; AASW = Antarctic Surface Water; NADW = North Atlantic Deep Water; CDW = Circumpolar Deep Water; UCDW = Upper Circumpolar Deep Water; LCDW = Lower Circumpolar Deep Water; WDW = Warm Deep Water; WSDW = Weddell Sea Deep Water; WSBW = Weddell Sea Bottom Water; and AABW = Antarctic Bottom Water. The blue triangles represent the mean positions of the Antarctic Polar Front (APF), Subantarctic Front (SAF), and STF

world oceans as Antarctic Bottom Water (AABW, Orsi et al. 1999).

Recently, a speed-up in the transport of surface and intermediate waters in the Atlantic sector of the SO was reported based on the observations of transient tracers, leading to more sequestration of anthropogenic carbon dioxide in this water mass (Tanhua et al. 2017). Salt et al. (2015) reported rapid acidification of the AAIW in the southwest Atlantic. More to the south in the Weddell Gyre, nutrient concentrations significantly increased in the surface and bottom layers from 1996 to 2011 (Hoppema et al. 2015). Also, in the same region along the Prime Meridian, van Heuven et al. (2011, 2014) found that dissolved inorganic carbon (DIC) concentrations significantly increased in the bottom water. This suggests that gradual changes are occurring in the nutrient and carbon concentrations in the Atlantic sector of the SO. An investigation on how nutrients and total carbon dioxide concentrations have changed in the Antarctic Intermediate Water along the Prime Meridian is, however, lacking.

The objective of this study is to investigate the interannual variability of nutrients and dissolved inorganic carbon (DIC) in the AAIW in the Atlantic sector of the SO. We additionally use hydrographic and oxygen data between 1990 and 2014 along the Prime Meridian north of the APF
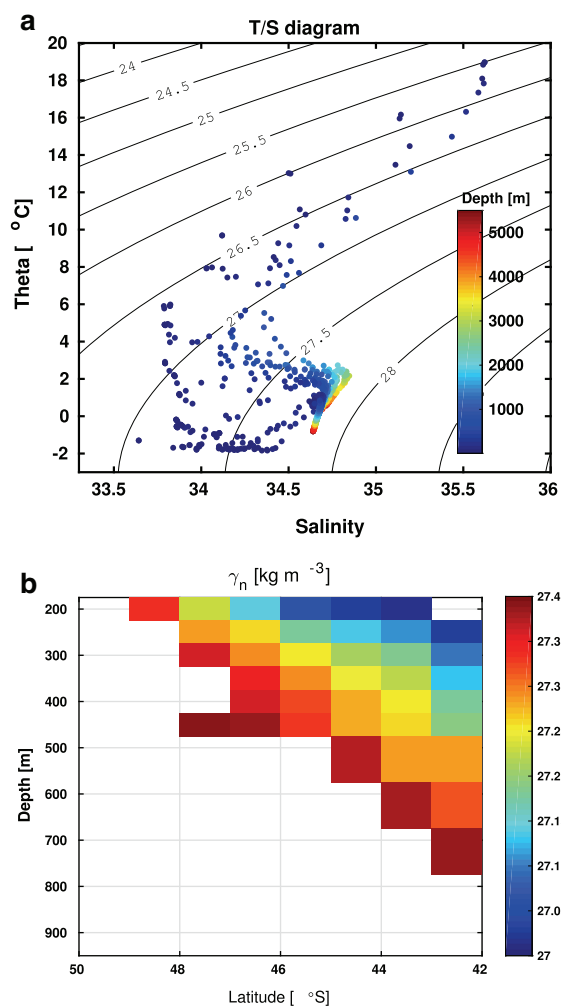
Fig. 2 **a** Temperature-salinity (T/S) diagram of niskin bottle data and **b** section plot of neutral density of the cruise 2014 (ANT-XXX/2). AAIW is located within the neutral density range of $27 < \gamma_n < 27.4$ (Sloyan and Rintoul 2001)

for supporting our case. Possible mechanisms that drive the observed variability of nutrients and DIC in relation to the circulation in the Atlantic sector of the SO are discussed.

2 Methods and data

Data are presented from a new cruise in 2014 (Boebel 2015) which has not been published previously. In addition, we extracted relevant hydrographic and biogeochemical data from cruises that covered our area of investigation (Prime Meridian north of the APF) from the global ocean data analysis project version 2 (GLODAPv2) database (Olsen

et al. 2016), an internally consistent data product for the world ocean. We extracted 10 cruises from GLODAPv2 that sampled our area of interest and from these we selected the cruises that met all of the following criteria: (i) sufficient spatial resolution in the region north of the APF between 50 and 42°S, the latitude range along which the intermediate and mode waters are formed (Hanawa and Talley 2001), (ii) acceptable quality of the carbon dioxide, and chemical data (WOCE flag = 2, Olsen et al. 2016), (iii) cruises also sampled the region between 57°S and 66°S that is used for checking the consistency of the datasets (explained below).

Four cruises from GLODAPv2 met these criteria so in total we analyzed the datasets from five cruises that cover the years 1990, 1992, 1998, 2008, and 2014 (Table 1, Fig. 3). Four cruises (1992, 1998, 2008, and 2014) are from the German icebreaker FS Polarstern. The 1990 expedition was conducted on board FS Meteor. The cruise from 1992 did not sample dissolved oxygen data north of 50°S. The new data from the cruise in 2014 (ANT-XXX/2, expocode 06AQ20141202; 2 December 2014 to 1 February 2015) is presented in this study (Section 3.1). The hydrographic data of this cruise appear in Driemel et al. (2017).

The data collected by the five cruises used in this study encompass potential temperature (θ), salinity (S), macronutrients (nitrate NO_3^-, phosphate PO_4^{3-} and silicic acid H_4SiO_4), total alkalinity (A_T), directly measured dissolved inorganic carbon (DIC) (as opposed to calculated from secondary variables), and dissolved oxygen (O_2). For the 2014 cruise (Boebel 2015), measurements of the dissolved nutrients, NO_3^-, PO_4^{3-}, and H_4SiO_4 were performed by UV-Vis spectrophotometric methods (Grasshoff et al. 1983) carried out on board with a Seal Analytical continuous-flow AutoAnalyzer. The concentration of dissolved oxygen in each sample collected by Niskin bottles at the Rosette sampler, mounted around the conductivity-temperature depth (CTD) sensor, was analyzed using a potentiometric Winkler method (Carpenter 1965). A VINDTA 3C system (Mintrop et al. 2000) was used for the determination of both A_T by acid potentiometric titration and DIC by coulometry after phosphoric acid addition, with a precision of ± 2 and ± 1 μmol kg^{-1}, respectively. From 1998 onwards, Certified Reference Material (CRM) was used for all CO_2 analyses (Dickson 2010).

We checked the consistency of the cruise ANT-XXX/2 (2014) data against adjusted GLODAPv2 cruises in the range of the lower Warm Deep Water and upper Weddell Sea Deep Water (lWDW/uWSDW) between the latitudes of 57–66°S and 800–2200 m depth for all eleven cruises that cover this region. This water mass is considered the least ventilated in the wider region (Klatt et al. 2002). For this purpose, we used all GLODAPv2 cruises that fulfilled the selection criteria (ii) and (iii) from above, i.e., cruises that cover the region chosen for the quality control with

Table 1 Relevant details of the five cruises used in this study: expocode, cruise, research vessel, and adjustments applied to the data and use of Certified Reference Material (CRM, Dickson 2010)

Expocode	Cruise	Vessel	SAL	DIC	A_T	NO_3^-	PO_4^{3-}	H_4SiO_4	O_2	Reference	CRMs
06MT19900123	06MT	Meteor	−0.0004 (0.0)	+1.01 (0.0)	NA	×1.00 (×0.98)	×1.00 (×0.98)	×1.02 (×0.96)	×1.00 (×0.99)	Chipman et al. (1994)	No
06AQ19920521	ANT-X/4	Polarstern	+0.001 (0.0)	−0.68(0.0)	NA	×1.01 (×0.98)	×1.00 (×0.98)	×1.00 (×1.00)	×1.00 (×1.00)	Hoppema et al. (1995)	No
06AQ19980328	ANT-XV/4	Polarstern	+0.0007 (0.0)	0.17 (−3)	NA	×0.99 (×1.0)	0.99 (×1.0)	0.99 (×1.0)	×0.99 (×1.00)	Hoppema (2004a)	Yes
06AQ20080210	ANT-XXIV/3	Polarstern	−0.0002 (0.0)	−0.92 (0.0)	+0.29 (−4)	×1.00 (×1.0)	×1.00 (×1.0)	×1.00 (×1.0)	×1.00 (×1.01)	van Heuven et al. (2011)	Yes
06AQ20141202	ANT-XXX/2	Polarstern	+0.004	−1.36	−1.00	×0.98	×0.98	NA	×0.99	This work	Yes

The data of all cruises were extracted from the GLODAPv2 product, except the 2014 cruise data (ANT-XXX/2). The table shows the adjustments that we applied in this study to obtain consistency on a regional level and the adjustments already applied in the GLODAPv2 dataset in brackets before we checked the local consistency. Both corrections were taken into account as we used the adjusted GLODAPv2 dataset and applied our own adjustments on top. Adjustments applied to the data are additive for S, DIC, and A_T, and multiplicative for the other parameters. NA=not available and ×1.00=means no adjustments were applied to the data
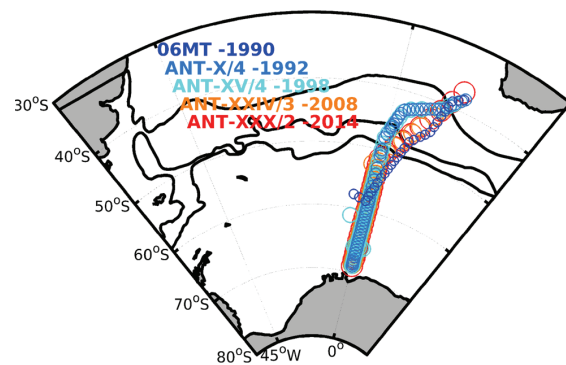
Fig. 3 Locations of the oceanographic sampling stations of the five cruises used in this study between 1990 and 2014. The black contours represent the mean positions of the Subtropical Front, Subantarctic Front, and Antarctic Polar Front (from north to south), respectively (Orsi et al. 1995)

acceptable data quality. This resulted in the selection of 10 GLODAPv2 cruises plus ANT-XXX/2 (Table S1) for our quality control. Note that the GLODAPv2 data were already adjusted by the GLODAPv2 team, but we locally refine the quality control to check the consistency of the new 2014 cruise data with reference to the GLODAPv2 dataset.

As a first quality check, we plotted the histogram of the datasets in the Antarctic Intermediate Water and compared it to GLODAPv2 climatological data (Lauvset et al. 2016) at a latitude/depth range of 38–50°S/200–700 m following Aoki et al. (2003). This analysis revealed that the silicic acid data of the cruise ANT-XXX/2 shows some abnormal high values (Fig. 4). These abnormal values were located between 40 and 42°S (white gap in Fig. 5). The anomalies of very high silicic acid concentrations for this cruise occurred from the surface to a depth of 3000 m. This analysis suggests that these silicic acid values are unrealistic and thus we discard these data points. We rejected the 2014 silicic acid data because the mean AAIW value would be strongly biased by this lack of data.

In the second step, we applied a more rigorous quality control similar to van Heuven et al. (2011). We extracted all parameters, namely DIC, A_T, NO_3^-, PO_4^{3-}, H_4SiO_4, O_2, and salinity in the range of the lWDW/uWSDW between the latitudes of 57 and 66°S and 800–2200 m depth. We then linearly regressed each parameter against the potential temperature (θ) values ranging between − 0.4 to 0.2 °C in the lWDW/uWSDW as in van Heuven et al. (2011). We determined the intercept at $\theta = 0$°C from the regression analyses. We obtained the required adjustment for each cruise by taking either the difference or the ratio between the mean intercept of all cruises and the intercept of each individual cruise. Additive adjustments based on the difference of the intercepts were applied for salinity, DIC,
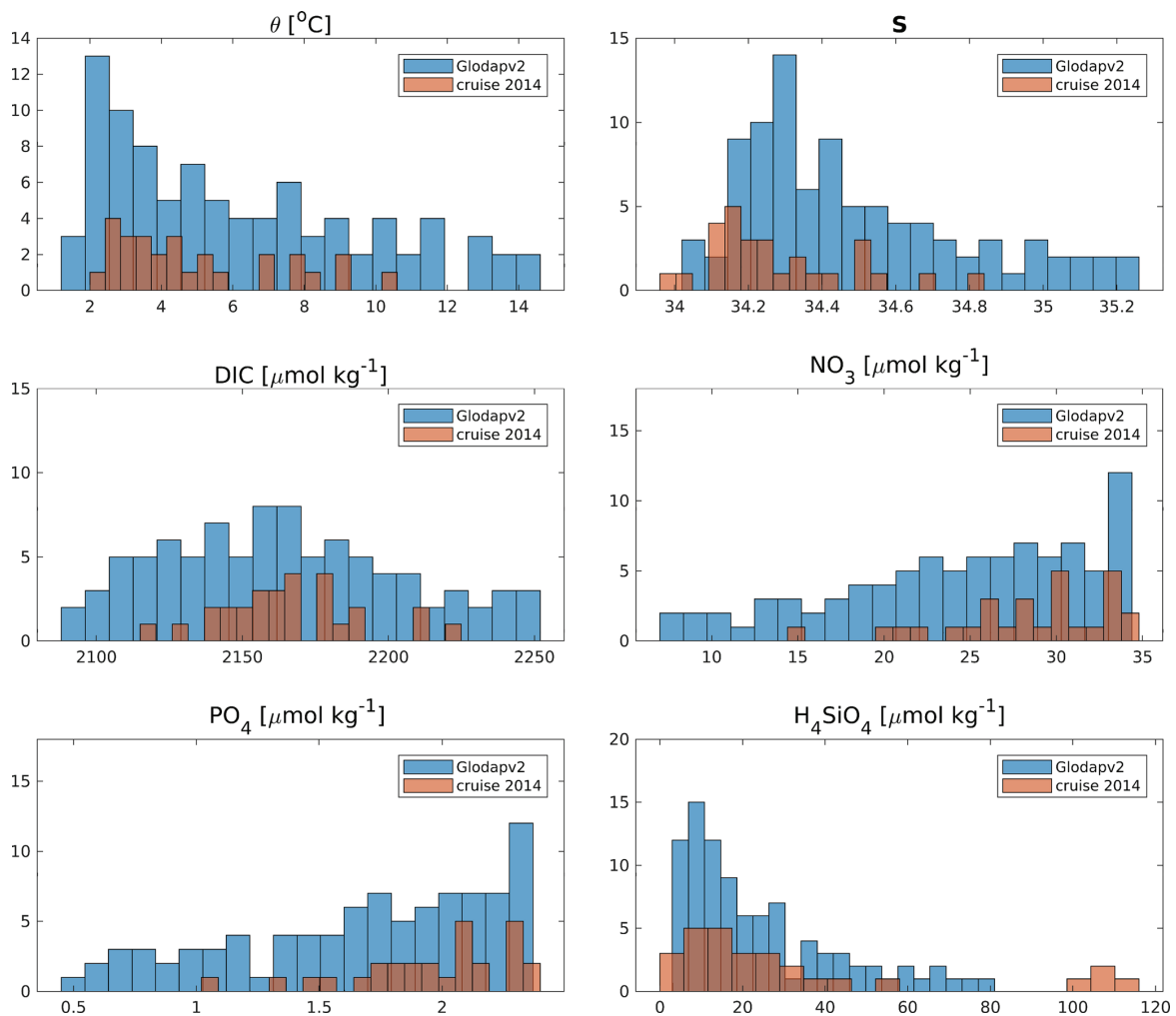
Fig. 4 Histogram showing the frequency distribution of observed values. The *y*-axis shows the number of observations between 200 and 700 m of the AAIW of a certain range of values as given on the *x*-axis.

The GLODAPv2 climatology is shown in blue and the cruise 2014 (ANT-XXX/2) is shown in orange

and A_T, and multiplicative adjustments based on the ratio were applied for nutrients and O_2 prior to further analyses to have optimal consistency among all cruises (van Heuven et al. 2011). The data from all 11 cruises showed consistent relationships with θ for all biogeochemical parameters selected within the lWDW/uWSDW water mass. Only the adjustments of the five selected cruises for the AAIW analysis are shown in this study (Table 1).

In general, we found and applied small adjustments that are in most cases below the minimum adjustment limits defined by GLODAPv2 (0.005 for salinity, 2% for nutrients, 4 μmol kg^{-1} for DIC and 6 μmol kg^{-1} for A_T and 1% for oxygen, Olsen et al. 2016). This confirms the high-quality

of the global GLODAPv2 quality control and applying these adjustments assures consistency of our dataset also on a regional level.

We then interpolated all cruise data onto a common grid assuming the longitude of all data is 0°E. For the gridding, we use a spacing of 0.5° in latitude and we use 46 vertical layers with 50 m thickness from the surface to 500 m, 100 m from 600 to 1500 m, and 200 m thickness from 1700 to the bottom. We assumed that the bottom topography is the same for all cruises.

For the gridding of the datasets, we used the simple objective mapping interpolation method as did van Heuven et al. (2011). The advantage of this method is that it

Fig. 5 Sections (0–1500 m)
along the Prime Meridian from
Polarstern ANT-XXX/2: neutral
density (γ_n), salinity (S),
potential temperature (θ),
dissolved inorganic carbon
(DIC), total alkalinity (A_T),
nitrate (NO_3^-), phosphate
(PO_4^{3-}), silicic acid (H_4SiO_4),
and apparent oxygen utilization
(AOU). Gray dots indicate
sampling stations. The deep
sections (1501 m to bottom) are
shown in Fig. S2
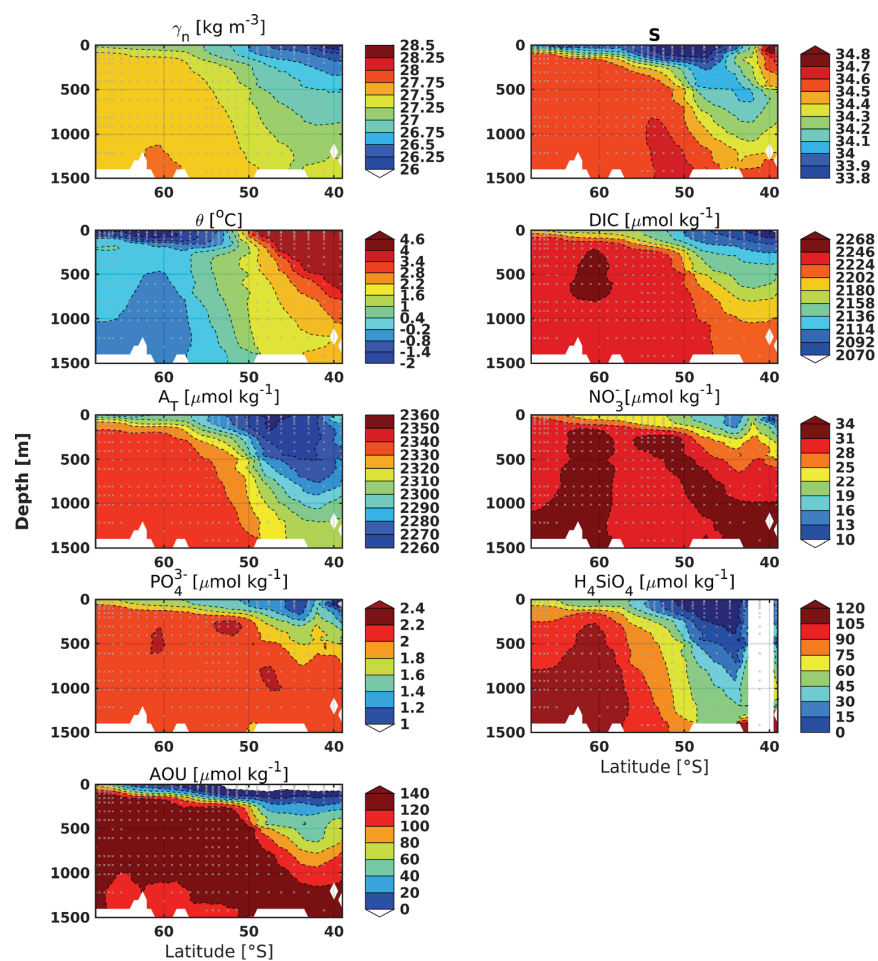
assigns equal weight to all cruises by resampling all data
of interest onto a common grid. This avoids the overrep-
resentation of those cruises that have more observations.
The core routine is the "obana.m" function, which does
the actual gridding and is part of the datafun toolbox
available on http://mooring.ucsd.edu/software/matlab/doc/
toolbox/datafun/index.html.

The apparent oxygen utilization (AOU) was calculated
from dissolved oxygen, temperature, and salinity using the
constants of Weiss (1970). Using the quality-controlled,
gridded data, we evaluated the decadal variability of θ,
salinity, nutrients, DIC, and AOU in the AAIW, which is
here defined by the neutral density range of $27 < \gamma_n < 27.4$
(Sloyan and Rintoul 2001) and latitude/depth range of 42–
50°S/ 200–700 m (Fig. 2). We limit our analysis to the depth
at 700 m which is the lower limit of AAIW in most years
(Fig. S1).

The mean and standard deviation of each variable was
calculated for the whole water mass in all years. A time
trend analysis was performed of the cruise mean values
using the ordinary linear least squares fit. In addition, we
measured inter-annual variability by the inter-annual range
(IAR) that we define as follows:

$$\text{IAR} = \max(|\overline{\overline{X}} - \overline{X}_k|), \tag{1}$$

where $\overline{X}_k$ is the mean of each cruise specified by the index
k and $\overline{\overline{X}}$ is the overall mean of all cruises. This measure
is similar to the standard deviation in the sense that the
standard deviation calculates the mean of all differences
between the overall mean and the mean of each individual
cruise ($\text{STD} = \text{mean}(|\overline{\overline{X}} - \overline{X}_k|)$) whereas the IAR calculates
the maximum of these differences. We prefer the IAR over
the STD as the STD tends to underestimate the deviation
from the mean if the data is not normally distributed.

3 Results

3.1 Sections of the cruise ANT-XXX/2 (2014)

The distributions of nitrate, phosphate, silicic acid, A_T, DIC, salinity, potential temperature (θ), apparent oxygen utilization (AOU) and neutral density (γ_n) along the Prime Meridian section for the cruise ANT-XXX/2 (2014) are shown in Fig. 5.

In the region north of 50°S, silicic acid shows a very strong vertical gradient with near-surface values below 1.5 μmol kg^{-1} to values of 130 μmol kg^{-1} at 4000 m (Fig. 5 and Fig. S2). NO_3^-, PO_4^{3-}, DIC, and AOU show low values at the surface ($NO_3^- < 10$ μmol kg^{-1}, $PO_4^{3-} < 0.75$ μmol kg^{-1}, DIC < 2066 μmol kg^{-1}, AOU < 100 μmol kg^{-1}) and in the inflowing North Atlantic Deep water ($NO_3^- < 26$ μmol kg^{-1}, $PO_4^{3-} < 1.8$ μmol kg^{-1}, DIC < 2200 μmol kg^{-1}, AOU < 110 μmol kg^{-1}). High concentrations of nitrate, phosphate, DIC, and AOU are found in the UCDW between 1100 and 1200 m ($NO_3^- > 34$ μmol kg^{-1}, $PO_4^{3-} > 2.4$ μmol kg^{-1}, DIC > 2272.5 μmol kg^{-1}, AOU > 140 μmol kg^{-1}).

South of 50°S, nutrients, AOU, DIC, and A_T show minima at the surface, maxima beneath it, and then they decrease monotonically toward the bottom. However, the values are higher and more homogeneous than those north of 50°S for the same depths (Fig. S2, Hoppema et al. 1998, Weiss et al. 1979). The distributions of density, salinity, potential temperature, nutrients, AOU, alkalinity, and DIC of the cruise ANT-XXX/2 comply with the hydrographic features observed during previous cruises (Fig. S3 to S6).

3.2 Carbon and nutrient variability in the AAIW along the Prime Meridian

We analyzed the time series of the overall water mass properties in the AAIW (neutral density range of $27 < \gamma_n < 27.4$) with respect to inter-annual variability (Figs. 6 and 7). Application of a linear regression to the cruise mean values yielded significant negative trends (level of significance $\alpha = 0.05$) for θ and salinity, and significant positive trends for DIC, NO_3^-, and AOU.

We found significant linear increases of 7 ± 4 μmol kg^{-1} decade^{-1} for DIC and 0.8 ± 0.6 μmol kg^{-1} decade^{-1} for NO_3^- (Fig. 7). The AOU increased over time (1.6 ± 0.7 μmol kg^{-1} decade^{-1}, Fig. 7) in line with the increase of macronutrients. In contrast, we found significant negative trends of -0.16 ± 0.1 °C decade^{-1} for θ and -0.03 ± 0.02 decade^{-1} for salinity (Fig. 6). The linear trend of phosphate is not significant but it is interesting to note that the maximum and minimum concentration for each cruise are monotonically increasing with the exception of the 1998
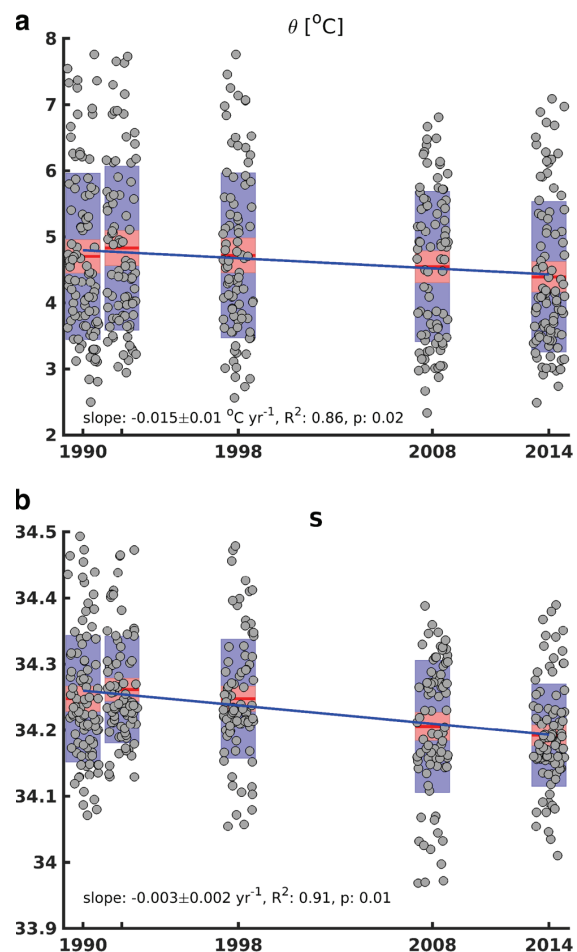
Fig. 6 Time series from 1990 to 2014 of gridded **a** potential temperature (θ) and **b** salinity (S) data in the core of AAIW here defined by the neutral density range $27 < \gamma_n < 27.4$ (Sloyan and Rintoul 2001). The red horizontal line represents the mean for each cruise. The light red bar represents the 95% confidence interval for the mean. The violet color indicates plus/minus one standard deviation. Non-overlapping confidence intervals indicate significant differences between means at the 5% level of significance. The raw data are shown as gray circles, with random horizontal dispersion introduced to improve the visibility of the data points. Time trends have been estimated by linear regression of cruise mean values against time. The significant trends are indicated by blue solid lines. The slope and p-value shown in the figure are for the trend which is calculated from the five average values of the individual cruises

data. The same is true for nitrate which in addition shows a linear positive trend of the means.

We also conducted this analysis along the density ranges of 27–27.1, 27.1–27.2, 27.2–27.3, and 27.3–27.4 (Fig. S7 to 10, respectively). In general, DIC, NO_3^-, θ, and S change consistently in the different neutral density ranges (Fig. S7
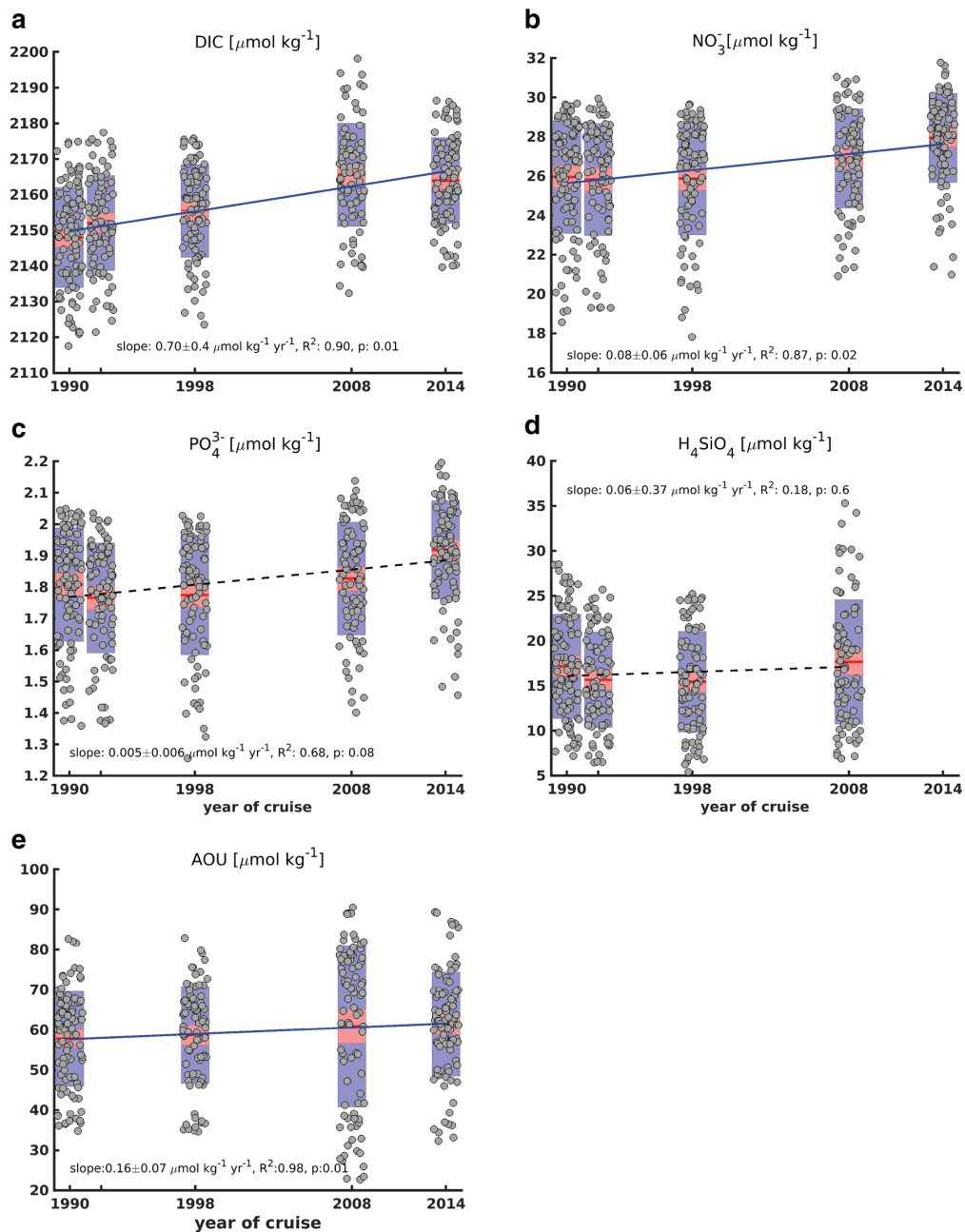
Fig. 7 Time series from 1990 to 2014 of gridded **a** dissolved inorganic carbon (DIC), **b** nitrate (NO_3^{3-}), **c** phosphate (PO_4^{3-}) and **d** silicic acid (H_4SiO_4) and **e** Apparent Oxygen Utilization (AOU) data in the core of AAIW here defined by the neutral density range $27 < \gamma_n < 27.4$ (Sloyan and Rintoul 2001). The red horizontal line represents the mean for each cruise. The light red bar represents the 95% confidence interval for the mean. The violet color indicates plus/minus one standard deviation. Non-overlapping confidence intervals indicate significant differences between means at the 5% level of significance. The raw data are shown as gray circles, with random horizontal dispersion introduced to improve the visibility of the data points. Time trends (μmol kg^{-1} year^{-1}) of DIC, NO_3^-, PO_4^{3-}, H_4SiO_4, and AOU have been estimated by linear regression of cruise mean values against time. The significant trends are indicated by blue solid lines and the dashed black lines represent statistically insignificant trends. The slope and p-value shown in the figure are for the trend which is calculated from the five average values of the individual cruises

to 10). The largest changes occurred in the γ_n interval of 27–27.1 (Fig. S7).

The overall mean of the potential temperature $\overline{\overline{\theta}}$ was 4.76 °C, with an IAR of 0.19 °C. The overall mean of salinity $\overline{\overline{S}}$ was 34.25, with an IAR of 0.03. The overall mean of dissolved inorganic carbon concentration, $\overline{\overline{DIC}}$, was 2157.1 μmol kg^{-1}, with an IAR of 10.4 μmol kg^{-1}.

The overall mean of nitrate concentration, $\overline{\overline{NO_3^-}}$, was 26.5 μmol kg^{-1}, with an IAR of 1.6 μmol kg^{-1}, equal to about 6% of the overall mean. PO_4^{3-} varied similarly, with an IAR of 0.12 μmol kg^{-1}, equal to about 6.6% of the overall mean of 1.82 μmol kg^{-1}. The correlation coefficient between $\overline{NO_3^-}$ and $\overline{PO_4^{3-}}$ is 0.92, suggesting that NO_3^- and PO_4^{3-} varied together with a mean molar ratio of 16:1. We found that the overall mean of AOU concentration, $\overline{\overline{AOU}}$, was 59.72 μmol kg^{-1}, with an IAR of 1.7 μmol kg^{-1}.

H_4SiO_4 showed larger inter-annual variability. The overall mean of silicic acid concentration, $\overline{\overline{H_4SiO_4}}$, was 17.4 μmol kg^{-1}, with an IAR of 1.9 μmol kg^{-1}, equal to about 11% of the overall mean. The IAR of H_4SiO_4 is based on only four cruises (1990, 1992, 1998, and 2008).

Of all years, the lowest concentrations of NO_3^- (<18 μmol kg^{-1}), PO_4^{3-} (<1.4 μmol kg^{-1}), and H_4SiO_4 (<6 μmol kg^{-1}) were observed during the year 1998.

4 Discussion

We analyzed the inter-annual variability of nutrients, DIC, AOU, temperature, and salinity in the AAIW of the Atlantic sector of the SO, north of 50° S along the Prime Meridian. The principal findings are (i) significant positive trends of DIC, NO_3^-, and AOU and negative trends of salinity and temperature in the AAIW and (ii) strong inter-annual variability of H_4SiO_4.

Substantial changes in nutrients, DIC, and AOU were also observed in other sectors of the SO (Iida et al. 2013; Ayers and Strutton 2013; Pardo et al. 2017) and in the subtropical Indian Ocean (Álvarez et al. 2011). Our estimates of IAR of nutrients are lower than the standard deviations of nutrients for another mode water mass (Subantarctic Mode Water, SAMW) in the Pacific and Australian sectors of the SO (Ayers and Strutton 2013). This suggests that either the variability is lower for Atlantic AAIW than for Pacific and Australian SAMW or that these differences arise due to differences in spatial and temporal data coverage.

Based on our results, $\overline{\overline{DIC}}$ concentrations in the AAIW increased at a rate of 0.70 ± 0.4 μmol kg^{-1} year^{-1} ($\Delta DIC_{observed}$ = 17.5 ± 10 μmol kg^{-1} in 25 years) and

$\overline{\overline{NO_3^-}}$ increased at a rate of 0.08 ± 0.06 μmol kg^{-1} year^{-1} (2 ± 1.5 μmol kg^{-1} in 25 years).

We estimated the theoretical DIC increase solely caused by the atmospheric CO_2 increase in the source water of the AAIW that we define as 50–53°S/0–100 m. The atmospheric CO_2 increase of 44.75 ppm between 1990 and 2014 at a given Revelle factor of 14.2 in 1990 would result in a theoretical ΔDIC_{ant} of 19 μmol kg^{-1} in this area. This is an upper estimate for anthropogenic carbon in the AAIW as time has passed since the AAIW has last been in contact with the atmosphere. Note that the mean DIC concentration in the source region (50–53°S/0–100 m) was 2134 μmol kg^{-1} in 1990 and 2156 μmol kg^{-1} in 2014, i.e., it has actually increased by 22 μmol kg^{-1} according to our observations. This finding together with the significant increase in NO_3^- suggests that other mechanisms are involved as well. The DIC increase might be the result of positive and negative contributions to the change that partly compensate each other.

As a second approach to separate the anthropogenic carbon from other effects, we estimated the expected overall mean natural carbon change consistent with the change in $\overline{NO_3^-}$ concentration based on the Redfield ratios of C:N:P = 106:14:1 for the Atlantic sector of the SO north of the APF (De Baar et al. 1997), which are slightly different from the classical ratios (Redfield 1963). An increase in $\overline{NO_3^-}$ at a rate of 0.08 ± 0.06 μmol kg^{-1} year^{-1} would result in an increase in DIC of 0.61 ± 0.45 μmol kg^{-1} year^{-1} ($\Delta DIC_{Redfield}$ = 15.3 ± 11.3 μmol kg^{-1} in 25 years). We, therefore, consider two possible scenarios to explain the change in DIC based on the best estimate of $\Delta DIC_{Redfield}$ (15.3 μmol kg^{-1}) and on the lower estimate of $\Delta DIC_{Redfield}$ (4 μmol kg^{-1}) within the $\Delta DIC_{Redfield}$ uncertainty.

In the first scenario ($\Delta DIC_{Redfield}$ = 15.3 μmol kg^{-1}), the difference of 2.2 μmol kg^{-1} between $\Delta DIC_{observed}$ and $\Delta DIC_{Redfield}$ represents the anthropogenic carbon that was taken up from the atmosphere and transported into the AAIW. This means that approximately 85% of the change in DIC observed could be explained by circulation or primary production changes and 15% by the uptake of anthropogenic carbon.

In the second scenario ($\Delta DIC_{Redfield}$ = 4 μmol kg^{-1}), the difference between $\Delta DIC_{observed}$ and $\Delta DIC_{Redfield}$ of 13.5 μmol kg^{-1} represents the anthropogenic carbon. In that case, approximately 25% of the change in DIC observed could be explained by circulation or primary production changes and 75% by the uptake of anthropogenic carbon.

Our theoretical estimate of ΔDIC_{ant} of 19 μmol kg^{-1} based on the atmospheric CO_2 increase suggests that the true $\Delta DIC_{Redfield}$ is likely at the lower end of the range. Also, we found that the amplitude of DIC change that varies spatially between 0.2 and 1.2 μmol kg^{-1} year^{-1}

between 44 and 50° S in the period 1990 to 2012 (Fig. S11) compares well with the amplitude of anthropogenic carbon change (0.4–1.2 μmol kg^{-1} year^{-1}) estimated by Tanhua et al. (2017). All these observations suggest that the more probable scenario is the one where 75% of the DIC change are explained by anthropogenic carbon uptake.

We consider two possible mechanisms that could explain the observed trends and variability of nutrients and the non-anthropogenic part of DIC (25%) in the AAIW: (1) an increase in upwelling, northward transport, and subduction rate and (2) a change in biological uptake of nutrients in the source waters of the AAIW and in organic matter remineralization.
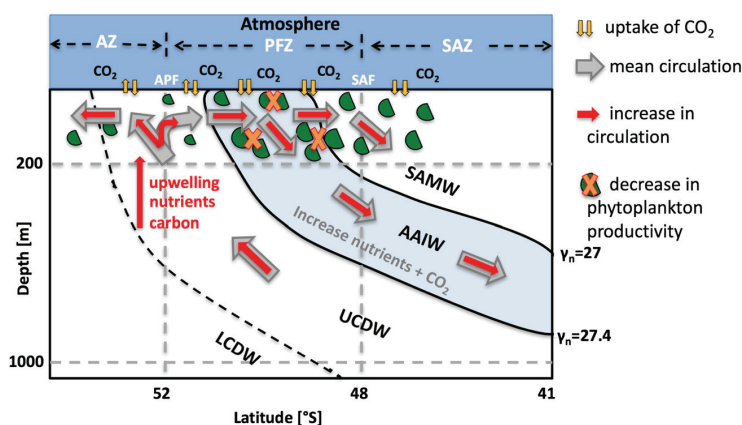
A schematic representation of the proposed mechanisms that could explain the changes in nutrients and DIC concentration in the AAIW is displayed in Fig. 8.

(1)   Increase in upwelling, northward transport, and subduc-
      tion rate:
      The non-anthropogenic part of the DIC increase as
      well as the nitrate increase in the AAIW could be
      related to the positive trend in the Southern Annular
      Mode (SAM) since the 1990s (Thompson et al. 2011)
      characterized by a southward shift and intensifica-
      tion of subpolar westerly winds. The strengthening
      of winds leads to stronger upwelling of carbon diox-
      ide and nutrient-rich Upper Circumpolar Deep Water
      (UCDW) (Whitworth and Nowlin 1987) and subse-
      quently to enhanced northward Ekman transport and
      subduction of AAIW (Downes et al. 2011). Enhanced
      upwelling of carbon is directly linked to stronger

transport of carbon into the ocean interior north of the Antarctic Polar Front (Hauck et al. 2013).

The hypothesis of an increase in upwelling is sup-ported by the decrease in potential temperature (-0.15 ± 0.1 °C decade^{-1}) that could be related to the increase in the subduction rate (Downes et al. 2011). This is in line with the findings of Tanhua et al. (2017) who reported a speed-up of ventilation in the upper intermediate waters of the Atlantic sector of the SO between 1998 and 2012 based on the analysis of transient tracers (SF$_6$/CFC-12). The increase of nitrate due to stronger upwelling of nutrient-rich deep water is in accord with Hoppema et al. (2015) who reported an increase in nutri-ent concentration in the surface waters of the Weddell Sea between 1996 and 2011 and linked the changes observed in nutrients to the increase in upwelling. Also, Pardo et al. (2017) conclude that biogeochemical change in the Southern Ocean south of Tasmania between 1995 and 2011 supports a scenario of intensification of upwelling caused by an increase in westerly winds. The increase in AOU could also be in line with the hypothesis of increased upwelling (Pardo et al. 2017) based on the assumption that the low-oxygen upwelled water does not fully equilibrate with the atmosphere before being subducted as AAIW. But this scenario is at odds with a slowdown of the overturning circulation that was suggested by DeVries et al. (2017). The fresh-ening (-0.03 ± 0.02 decade^{-1} change in salinity) can be explained by the increase in net precipitation in the subpolar regions of the Southern Hemisphere (Skliris et al. 2014; Durack and Wijffels 2010).

Fig. 8 Schematic representation of the proposed mechanisms that could explain the changes in nutrients and DIC concentration in the AAIW (neutral density range of 27 $< \gamma_n <$ 27.4). Gray arrows represent the mean state of the upper-ocean overturning circula-tion. The smaller and red arrows represent the first hypothesis: an increase in the upper-ocean overturning circulation The orange crosses represent the second hypothesis: a decrease in phytoplankton pro-ductivity. AZ = Antarctic Zone; PFZ = Polar Frontal Zone; SAZ = Subantarctic Zone; APF = Antarctic Polar Front; and SAF = Sub-antarctic Front. AAIW = Antarctic Intermediate Water; SAMW = Subantarctic Mode Water; UCDW = Upper Circompolar Deep Water; and LCDW = Lower Circompolar Deep Water

(2) Change in biological uptake of nutrients in the source waters of the AAIW and in organic matter remineralization:

Decreasing productivity in the source region of the AAIW may well explain the increasing nutrient concentrations observed in the AAIW core.

An increase in nitrate concentration in the AAIW could be caused by an increase in remineralization of particulate or dissolved organic carbon or could as well be caused by the decrease in nitrate uptake by phytoplankton in the surface source water of the AAIW. In the first case, larger remineralization would imply more oxygen consumption, which can be measured by apparent oxygen utilization (AOU). Indeed, we found that AOU showed a significant positive trend along with nutrients (Fig. 7).

The time trends of C:N:P (140:16:1) are approximately in line with the Redfield ratios. The time trend of AOU:C (1:4.4) is much smaller than expected from stoichiometric ratios (1:1.5, Anderson and Sarmiento 1994). Changes in remineralization would more lead to changes in AOU following known stoichiometry (Redfield 1963; Anderson and Sarmiento 1994). Changes in surface productivity might not necessarily lead to accompanying change in oxygen due to air-sea exchange. This suggests that the changes in surface productivity dominate over remineralization.

Decreased nutrient uptake by phytoplankton would imply that primary production also decreased. Kahru et al. (2017) indeed found a significant decreasing trend of the annual maximum monthly average net primary production (NPP) between 2011 and 2016 of overall -23% in a domain of $\pm 25°$ longitude around the Prime Meridian and between $52°S$ and $40°S$ based on satellite observations. However, there was no significant trend before 2011. A decrease in NPP in AAIW source water would lead to an increase in amounts of residual nutrients in the surface ocean which are then transported to AAIW via subduction. This hypothesis, however, cannot explain trends in temperature and salinity that are apparent in our datasets.

We revealed a stronger inter-annual variability of H_4SiO_4 concentration as compared to the other macronutrients, which was similarly found for the Pacific and Australian SAMW (Ayers and Strutton 2013). The high IAR of H_4SiO_4 does not surprise because north of the APF zone, H_4SiO_4 shows a stronger horizontal gradient than other macronutrients (nitrate and phosphate) and silicic acid concentration could limit diatom productivity (Laubscher et al. 1993; Conkright et al. 1994). Of all years, 1998 is the year during which nutrient concentrations were particularly low. H_4SiO_4 values as low as 6 μmol kg^{-1} were observed which can be limiting to some diatom species and could be related to the intense phytoplankton bloom occurring in the APF zone (Laubscher et al. 1993; Moore and Abbott 2000).

5 Conclusions

This study used observational data from the Prime Meridian section to investigate the inter-annual variability of nutrients, dissolved inorganic carbon (DIC), and apparent oxygen utilization (AOU) along with temperature and salinity in the Antarctic Intermediate Water (AAIW) between 1990 and 2014. We found significant positive trends in DIC, nitrate, and AOU, and negative trends in temperature and salinity in the AAIW.

These observations support a scenario of an increase in the upwelling of nutrients in the Antarctic divergence due to the intensification of westerlies linked to a positive trend in SAM. This would go along with an increase in the northward Ekman transport of the cold nutrient-rich surface waters until they get subducted and form AAIW. This suggests that the Atlantic sector has experienced an increased upper-ocean overturning in contrast to the global analysis of DeVries et al. (2017).

Stronger remineralization and a decrease in net primary production (NPP) might have contributed to the biogeochemical changes that we observed. However, the decrease in net primary production (NPP) observed in the AAIW source region that would lead to an increase in amounts of residual nutrients in the surface ocean could have contributed to the trends we observed in nitrate only since 2011. As this would not alter hydrographic properties, it cannot be the sole explanation.

We suggest that about 75% of the increase in DIC could be explained by the increase in anthropogenic carbon uptake in the source waters of the AAIW and 25% due to circulation and potentially production changes. Further studies and longer time series are needed to shed light on the relative contribution of these two mechanisms to the observed changes.

The changes we observed in the AAIW have the potential to significantly impact downstream low latitude primary productivity and carbon cycle over long timescales (Sarmiento et al. 2004; Ayers and Strutton 2013).

References

Álvarez M, Tanhua T, Brix H, Lo Monaco C, Metzl N, McDonagh EL, Bryden HL (2011) Decadal biogeochemical changes in the subtropical Indian Ocean associated with Subantarctic Mode Water. J Geophys Res 116:C09016. https://doi.org/10.1029/2010JC006475

Anderson LA, Sarmiento JL (1994) Redfield ratios of remineralization determined by nutrient data analysis. Glob Biogeochem Cycles 8(1):65–80

Aoki S, Yoritaka M, Masuyama A (2003) Multidecadal warming of subsurface temperature in the Indian sector of the Southern Ocean. J Geophys Res 108:8081. https://doi.org/10.1029/ 2000JC000307, C4

Ayers JM, Strutton PG (2013) Nutrient variability in subantarctic mode waters forced by the southern annular mode and ENSO. Geophys Res Lett 40(13):3419–3423. https://doi.org/10.1002/grl.50638

Boebel O (ed) (2015) The expedition PS89 of the research vessel POLARSTERN to the Weddell Sea in 2014/2015. Berichte zur Polar- und Meeresforschung= Reports on polar and marine research. Alfred-Wegener-Institut, Bremerhaven, Germany. https://doi.org/10.2312/BzPM_0689_2015

Bryden HL, Longworth HR, Cunningham SA (2005) Slowing of the Atlantic meridional overturning circulation at 25° N. Nature 438(7068):655–657. https://doi.org/10.1038/nature04385

Carpenter JH (1965) The accuracy of the Winkler method for dissolved oxygen analysis. Limnol Oceanogr 10(1):135–140. https://doi.org/10.4319/lo.1965.10.1.0135

Chipman DW, Takahashi T, Breger D, Sutherland SC, Kozyr A, Gaslightwala AF (1994) Carbon dioxide, hydrographic, and chemical data obtained during the R/V Meteor cruise 11/5 in the South Atlantic and Northern Weddell Sea areas (WOCE sections A-12 and A-21). Tech. rep., Oak Ridge National Lab., TN (United States). Carbon Dioxide Information Analysis Center; Columbia Univ., Palisades. Lamont-Doherty Earth Observatory. https://doi.org/10.2172/10191502

Conkright ME, Levitus S, Boyer TP (1994) World Ocean Atlas: 1994 Volume 1 Nutrients, U.S. Department of Commerce, NOAA, Washington DC, U.S.A.

De Baar HJW, Buma AGJ, Nolting RF, Cadée GC, Jacques G, Tréguer PJ (1990) On iron limitation of the Southern Ocean: experimental observations in the Weddell and Scotia Seas. Mar Ecol Prog Ser 65:105–122. http://www.jstor.org/stable/24846120

De Baar HJW, Van Leeuwe MA, Scharek R, Goeyens L, Bakker KMJ, Fritsche P (1997) Nutrient anomalies in Fragilariopsis kerguelensis blooms, iron deficiency and the nitrate/phosphate ratio (A. C. Redfield) of the Antarctic Ocean. Deep-Sea Res II Top Stud Oceanogr 44(1):229–260. https://doi.org/10.1016/S0967-0645(96)00102-6

de las Heras MM, Schlitzer R (1999) On the importance of intermediate water flows for the global ocean overturning. J Geophys Res Oceans 104(C7):15515–15536. https://doi.org/10.1029/1999JC900102

DeVries T, Holzer M, Primeau F (2017) Recent increase in oceanic carbon uptake driven by weaker upper-ocean overturning. Nature 542(7640):215–218. https://doi.org/10.1038/nature21068

Dickson AG (2010) Standards for ocean measurements. Oceanography 23(3):34–47. https://doi.org/10.5670/oceanog.2010.22

Downes SM, Budnick AS, Sarmiento JL, Farneti R (2011) Impacts of wind stress on the Antarctic Circumpolar Current fronts and associated subduction. Geophys Res Lett 38:L11605. https://doi.org/10.1029/ 2011GL047668

Driemel A, Fahrbach E, Rohardt G, Beszczynska-Möller A, Boetius A, Budéus G, Cisewski B, Engbrodt R et al (2017) From pole to pole: 33 years of physical oceanography onboard R/V Polarstern. Earth Syst Sci Data 9:211–220. https://doi.org/10.5194/essd-9-211-2017

Durack PJ, Wijffels SE (2010) Fifty-year trends in global ocean salinities and their relationship to broad-scale warming. J Clim 23(16):4342–4362. https://doi.org/10.1175/2010JCLI3377.1

Gordon AL (1981) South Atlantic thermocline ventilation. Deep-Sea Res A Oceanogr Res Pap 28(11):1239–1264. https://doi.org/10.1016/0198-0149(81)90033-9

Grasshoff K, Ehrhardt M, Kremling K (1983) Methods of seawater analysis. Verlag Chemie, Weinheim, p 419

Gruber N, Gloor M, Mikaloff Fletcher SE, Doney SC, Dutkiewicz S, Follows MJ, Gerber M, Jacobson AR, Joos F, Lindsay K et al (2009) Oceanic sources, sinks, and transport of atmospheric CO_2. Glob Biogeochem Cycles 23(GB1005). https://doi.org/10.1029/2008GB003349

Hanawa K, Talley LD (2001) Mode waters. Int Geophys Ser 77:373–386. https://doi.org/10.1016/S0074-6142(01)80129-7

Hauck J, Völker C, Wang T, Hoppema M, Losch M, Wolf-Gladrow DA (2013) Seasonally different carbon flux changes in the Southern Ocean in response to the southern annular mode. Glob Biogeochem Cycles 27(4):1236–1245. https://doi.org/10.1002/2013GB004600

Hoppema M (2004a) Weddell Sea is a globally significant contributor to deep-sea sequestration of natural carbon dioxide. Deep-Sea Res I Oceanogr Res Pap 51(9):1169–1177. https://doi.org/10.1016/j.dsr.2004.02.011

Hoppema M (2004b) Weddell Sea turned from source to sink for atmospheric CO_2 between pre-industrial time and present. Glob Planet Chang 40(3):219–231. https://doi.org/10.1016/j.gloplacha.2003.08.001

Hoppema M, Fahrbach E, Schröder M, Wisotzki A, De Baar HJW (1995) Winter-summer differences of carbon dioxide and oxygen in the Weddell Sea surface layer. Mar Chem 51(3):177–192. https://doi.org/10. 1016/0304-4203(95)00065-8

Hoppema M, Fahrbach E, Richter KU, De Baar HJW, Kattner G (1998) Enrichment of silicate and CO_2 and circulation of the bottom water in the Weddell Sea. Deep-Sea Res I Oceanogr Res Pap 45(11):1797–1817. https://doi.org/10.1016/S0967-0637(98)00029-6

Hoppema M, Bakker K, van Heuven SMAC, van Ooijen JC, De Baar HJW (2015) Distributions, trends and inter-annual variability of nutrients along a repeat section through the Weddell Sea (1996–2011). Mar Chem 177:545–553. https://doi.org/10.1016/j.marchem.2015.08.007

Iida T, Odate T, Fukuchi M (2013) Long-term trends of nutrients and apparent oxygen utilization south of the polar front in Southern Ocean intermediate water from 1965 to 2008. PloS one 8(8):e71,766. https://doi.org/10.1371/journal.pone.0071766

Kahru M, Lee Z, Mitchell BG (2017) Contemporaneous disequilibrium of bio-optical properties in the Southern Ocean. Geophys Res Lett 44:2835–2842. https://doi.org/10.1002/2016GL072453

Khatiwala S, Primeau F, Hall T (2009) Reconstruction of the history of anthropogenic CO_2 concentrations in the ocean. Nature 462(7271):346–349. https://doi.org/10.1038/nature08526

Klatt O, Roether W, Hoppema M, Bulsiewicz K, Fleischmann U, Rodehacke C, Fahrbach E, Weiss RF, Bullister JL (2002) Repeated CFC sections at the Greenwich Meridian in the Weddell Sea. J Geophys Res Oceans 107(C4). https://doi.org/10.1029/2000JC000731

Landschützer P, Gruber N, Haumann FA, Rödenbeck C, Bakker DCE, Van Heuven S, Hoppema M, Metzl N, Sweeney C, Takahashi T et al (2015) The reinvigoration of the Southern Ocean carbon sink. Science 349(6253):1221–1224. https://doi.org/10.1126/science.aab2620

Laubscher RK, Perissinotto R, McQuaid CD (1993) Phytoplankton production and biomass at frontal zones in the Atlantic sector of the Southern Ocean. Polar Biol 13(7):471–481

Lauvset SK, Key RM, Olsen A, van Heuven S, Velo A, Lin X, Schirnick C, Kozyr A, Tanhua T, Hoppema M, Jutterström S, Steinfeldt R, Jeansson E, Ishii M, Perez FF, Suzuki T, Watelet S (2016) A new global interior ocean mapped climatology: the 1° × 1° GLODAP version 2. Earth Syst Sci Data 8:325–340. https://doi.org/10.5194/essd-8-325-2016

Le Quéré C, Rödenbeck C, Buitenhuis ET, Conway TJ, Langenfelds R, Gomez A, Labuschagne C, Ramonet M, Nakazawa T, Metzl N et al (2007) Saturation of the Southern Ocean CO_2 sink due to recent climate change. Science 316(5832):1735–1738. https://doi.org/10.1126/science.1136188

Le Quéré C, Andrew RM, Canadell JG, Sitch S, Korsbakken JI, Peters GP, Manning AC, Boden TA, Tans PP, Houghton RA et al (2016) Global carbon budget 2016. Earth Syst Sci Data 8(2):605–649. https://doi.org/10.5194/essd-8-605-2016

Marinov I, Gnanadesikan A, Toggweiler JR, Sarmiento JL (2006) The Southern Ocean biogeochemical divide. Nature 441(7096):964–967. https://doi.org/10.1038/nature04883

Marshall GJ (2003) Trends in the Southern Annular Mode from observations and reanalyses. J Clim 16(24):4134–4143. https://doi.org/10.1175/1520-0442(2003)016<4134:TITSAM>2.0.CO;2

Martin JH, Gordon RM, Fitzwater SE (1990) Iron in Antarctic waters. Nature 345(6271):156–158

Metzl N, Brunet C, Jabaud-Jan A, Poisson A, Schauer B (2006) Summer and winter air–sea CO_2 fluxes in the Southern Ocean. Deep-Sea Res I Oceanogr Res Pap 53(9):1548–1563. https://doi.org/10.1016/j.dsr.2006.07.006

Mintrop L, Pérez FF, González-Dávila M, Santana-Casiano JM, Körtzinger A (2000) Alkalinity determination by potentiometry: intercalibration using three different methods. Ciencias Marinas 26(1):23–37

Mitchell BG, Brody EA, Holm-Hansen O, McClain C, Bishop J (1991) Light limitation of phytoplankton biomass and macronutrient utilization in the Southern Ocean. Limnol Oceanogr 36(8):1662–1677. https://doi.org/10.4319/lo.1991.36.8.1662

Moore JK, Abbott MR (2000) Phytoplankton chlorophyll distributions and primary production in the Southern Ocean. J Geophys Res 105(C12):28709–28722. https://doi.org/10.1029/1999JC000043

Morrison AK, Frölicher TL, Sarmiento JL (2015) Upwelling in the Southern Ocean. Phys Today 68(1):27–32. https://doi.org/10.1063/PT.3.2654

Nelson DM, Smith W (1991) Sverdrup revisited: critical depths, maximum chlorophyll levels, and the control of Southern Ocean productivity by the irradiance-mixing regime. Limnol Oceanogr 36(8):1650–1661. https://doi.org/10.4319/lo.1991.36.8.1650

Olsen A, Key RM, van Heuven S, Lauvset SK, Velo A, Lin X, Schirnick C, Kozyr A, Tanhua T, Hoppema M, Jutterström S, Steinfeldt R, Jeansson E, Ishii M, Pérez FF, Suzuki T (2016) The Global Ocean Data Analysis Project version 2 (GLODAPv2)—an internally consistent data product for the world ocean. Earth Syst Sci Data 8:297–323. https://doi.org/10.5194/essd-8-297-2016

Orsi AH, Whitworth T, Nowlin WD (1995) On the meridional extent and fronts of the Antarctic Circumpolar Current. Deep-Sea Res I Oceanogr Res Pap 42(5):641–673. https://doi.org/10.1016/0967-0637(95)00021-W

Orsi AH, Johnson GC, Bullister JL (1999) Circulation, mixing, and production of Antarctic Bottom Water. Prog Oceanogr 43(1):55–109. https://doi.org/10.1016/S0079-6611(99)00004-X

Pardo PC, Tilbrook B, Langlais C, Trull TW, Rintoul SR (2017) Carbon uptake and biogeochemical change in the Southern Ocean, south of Tasmania. Biogeosciences 14(22):5217–5237

Peterson RG, Whitworth T (1989) The Subantarctic and Polar Fronts in relation to deep water masses through the southwestern Atlantic. J Geophys Res Oceans 94(C8):10817–10838. https://doi.org/10.1029/JC094iC08p10817

Redfield AC (1963) The influence of organisms on the composition of seawater. The Sea 2:26–77

Rintoul SR, Hughes CW, Olbers D (2001) The Antarctic circumpolar current system. In: Siedler G, Church J, Gould J (eds). Academic Press, New York, pp 271–302. https://doi.org/10.1016/S0074-6142(01)80124-8

Sabine CL, Feely RA, Gruber N, Key RM, Lee K, Bullister JL, Wanninkhof R, Wong C, Wallace DW, Tilbrook B et al (2004) The oceanic sink for anthropogenic CO_2. Science 305(5682):367–371. https://doi.org/10.1126/science.1097403

Salt LA, van Heuven SMAC, Claus ME, Jones EM, de Baar HJW (2015) Rapid acidification of mode and intermediate waters in the southwestern Atlantic Ocean. Biogeosciences 12(5):1387–1401. https://doi.org/ 10.5194/bg-12-1387-2015

Sarmiento JL, Gruber N, Brzezinski MA, Dunne JP (2004) High-latitude controls of thermocline nutrients and low latitude biological productivity. Nature 427(6969):56–60. https://doi.org/10.1038/nature02127

Skliris N, Marsh R, Josey SA, Good SA, Liu C, Allan RP (2014) Salinity changes in the World Ocean since 1950 in relation to changing surface freshwater fluxes. Climate dynamics 43(3–4):709–736. https://doi.org/10.1007/s00382-014-2131-7

Sloyan BM, Rintoul SR (2001) Circulation, renewal, and modification of Antarctic Mode and Intermediate Water. J Phys Oceanogr 31(4):1005–1030. https://doi.org/10.1175/1520-0485(2001)031<1005:CRAMOA>2.0.CO;2

Talley LD (1996) Antarctic intermediate water in the South Atlantic. In: Wefer G, Berger WH, Siedler G, Webb DJ (eds) The South Atlantic. Springer, Berlin, pp 219–238

Talley LD (2013) Closure of the global overturning circulation through the Indian, Pacific, and Southern Oceans: schematics and transports. Oceanography 26(1):80–97

Tanhua T, Hoppema M, Jones EM, Stöven T, Hauck J, González Dávila M, Santana-Casiano M, Álvarez M, Strass VH (2017) Temporal changes in ventilation and the carbonate system in the Atlantic sector of the Southern Ocean. Deep-Sea Res II Top Stud Oceanogr 138:26–38. https://doi.org/10.1016/j.dsr2.2016.10.004

Thompson DW, Solomon S, Kushner PJ, England MH, Grise KM, Karoly DJ (2011) Signatures of the Antarctic ozone hole in Southern Hemisphere surface climate change. Nat Geosci 4(11):741–749. https://doi.org/10.1038/NGEO1296

van Heuven SMAC, Hoppema M, Huhn O, Slagter HA, De Baar HJW (2011) Direct observation of increasing CO_2 in the Weddell Gyre along the Prime Meridian during 1973–2008. Deep-Sea Res II Top Stud Oceanogr 58(25):2613–2635. https://doi.org/10.1016/j.dsr2.2011. 08.007

van Heuven SMAC, Hoppema M, Jones EM, de Baar HJW (2014) Rapid invasion of anthropogenic CO_2 into the deep circulation of

the Weddell Gyre. Philos Trans R Soc Lond A: Math Phys Engi Sci 372(2019):20130,056. https://doi.org/10.1098/rsta.2013.0056

Weiss RF (1970) The solubility of nitrogen, oxygen and argon in water and seawater. Deep-Sea Res 17:721–735

Weiss RF, Östlund HG, Craig H (1979) Geochemical studies of the Weddell Sea. Deep Sea Res A Oceanogr Res Pap 26(10):1093–1120. https://doi.org/10.1016/0198-0149(79)90059-1

Wetzel P, Winguth A, Maier-Reimer E (2005) Sea-to-air CO_2 flux from 1948 to 2003: a model study. Global Biogeochem Cycles 19:GB2005. https://doi.org/10.1029/2004GB002339

Whitworth T, Nowlin WD (1987) Water masses and currents of the Southern Ocean at the Greenwich Meridian. J Geophys Res Oceans 92(C6):6462–6476. https://doi.org/10.1029/JC092iC06p06462

Wunsch C, Heimbach P (2006) Estimated decadal changes in the North Atlantic meridional overturning circulation and heat flux 1993–2004. Journal of Physical Oceanography 36(11):2012–2024. https://doi.org/10.1175/JPO2957.1

Affiliations

Essowè Panassa[1] [ID] · **J. Magdalena Santana-Casiano[2]** · **Melchor González-Dávila[2]** · **Mario Hoppema[1]** · **Steven M.A.C van Heuven[3]** · **Christoph Völker[1]** · **Dieter Wolf-Gladrow[1]** · **Judith Hauck[1]**

J. Magdalena Santana Casiano
magdalena.santana@ulpgc.es

Melchor González-Dávila
melchor.gonzalez@ulpgc.es

Mario Hoppema
mario.hoppema@awi.de

Steven M.A.C van Heuven
svheuven@gmail.com

Christoph Völker
christoph.voelker@awi.de

Dieter Wolf-Gladrow
dieter.wolf-gladrow@awi.de

Judith Hauck
judith.hauck@awi.de

[1]   Alfred Wegener Institute, Helmholtz Centre for Polar and Marine Research, Am Handelshafen 12, 27570 Bremerhaven, Germany

[2]   Instituto de Oceanografía y Cambio Global. Universidad de Las Palmas de Gran Canaria, Campus de Tafira, 35017, Las Palmas de Gran Canaria, Spain

[3]   Royal Netherlands Institute for Sea Research, 1790 AB Den Burg, The Netherlands

Supplementary Information

1 **Supplementary Material of the manuscript**
2 **"Variability of nutrients and carbon dioxide in the**
3 **Antarctic Intermediate Water between 1990 and**
4 **2014"**

5 **Essowè Panassa · J. M. Santana**
6 **Casiano · M. González Dávila · M.**
7 **Hoppema · S. M.A.C. van Heuven · C.**
8 **Völker · D. Wolf-Gladrow · J. Hauck**

9 the date of receipt and acceptance should be inserted later

10 **Contents of this file**

11 1. Figures S1 to S11
12 2. Table S1

13 **Introduction**

14 This supplementary material contains:

15 1) a summary table of all cruises used for calculating the adjustments we
16 applied to reach consistency between all data sets (Table S1).

17 2) the AAIW water masses of the five cruises (1990, 1992, 1998, 2008 and
18 2014) as selected within the neutral density range of $27 < \gamma_n < 27.4$ (Fig. S1).

19 3) the deep section plots (1501 m to bottom) for the cruise 2014 (ANT-
20 XXX/2) of neutral density, salinity, potential temperature, dissolved inorganic
21 carbon, total alkalinity, nitrate, phosphate, silicic acid and Apparent Oxygen
22 Utilization (AOU, Fig. S2).

23 4) the full section plots of neutral density, salinity, potential temperature,
24 dissolved inorganic carbon, total alkalinity, nitrate, phosphate, silicic acid and
25 Apparent Oxygen Utilization (AOU) for the cruises from 1990, 1992, 1998 and
26 2008 (Fig. S3 to S6).

27 5) Fig. S7 to Fig. S10 show the time series from 1990 to 2014 of potential
28 temperature, salinity, DIC, nitrate, phosphate, silicic acid and Apparent Oxy-
29 gen Utilization (AOU) variability in the AAIW in the different neutral density
30 ranges of 27-27.1, 27.1-27.2, 27.2-27.3 and 27.3-27.4, respectively.

Alfred Wegener Institute Helmholtz Centre for Polar and Marine Research
Am Handelshafen 12
27570 Bremerhaven
Germany
Tel.: +49(471)4831-1450
Fax: +49(471)4831-1149
E-mail: essowe.panassa@awi.de

2   Panassa et al.

31   6) Fig. S11 shows the inferred time rates of change for gridded dissolved
32   inorganic carbon (DIC) over the period of 1990 to 2012. For this trend cal-
33   culation, we used the cruises 1990, 1992, 1998 and the cruise 2012 data (AN-
34   TXXVIII/3; expocode 06AQ20120107; 7 January to 11 March 2012). The lat-
35   ter sampled only between the latitude range of 44-50°S north of the Antarctic
36   Polar Front (APF). Because there is no data south of the APF, we could
37   not apply a correction. The data of the 2012 cruise are available at CDIAC:
38   http://cdiac.ornl.gov/ftp/oceans/CLIVAR/
39   A12_06AQ20120107/.

Table S1 Relevant details of the 11 cruises used in this study: expocode, cruise, research vessel, availability of data and use of Certified Reference Material (CRM). The data of all cruises were extracted from the GLODAPv2 product, except the 2014 cruise data (ANT-XXX/2). X=data is available and passed quality control and NA=not available or failed quality control. Only cruises 1990, 1992, 1998, 2008 and 2014 from the eleven cruises sampled data north of 50°S along the Prime Meridian, other cruises have only data south of 50°S.

Expocode	Cruise	Vessel	SAL	DIC	A_T	NO_3^-	PO_4^{3-}	H_4SiO_4	O_2	Reference	CRMs
06AQ19860627	ANT-V/2-3	Polarstern	X	X	NA	X	X	X	X	GLODAPv2	No
06MT19900123	06MT	Meteor	X	X	NA	X	X	X	X	GLODAPv2	No
06AQ19920521	ANT-X/4	Polarstern	X	X	NA	X	X	X	X	GLODAPv2	No
06AQ19960317	ANT-XIII/4	Polarstern	X	X	NA	X	X	X	X	GLODAPv2	No
06AQ19980328	ANT-XV/4	Polarstern	X	X	NA	X	X	X	X	GLODAPv2	Yes
06AQ20021124	ANT-XX/2	Polarstern	X	X	NA	X	NA	NA	X	GLODAPv2	Yes
06AQ20050122	ANT-XXII/3	Polarstern	X	X	NA	X	X	X	X	GLODAPv2	Yes
06AQ20071128	ANT-XXIV/2	Polarstern	NA	X	X	NA	NA	NA	NA	GLODAPv2	Yes
06AQ20080210	ANT-XXIV/3	Polarstern	X	X	X	X	X	X	X	GLODAPv2	Yes
06AQ20101128	ANT-XXVII/2	Polarstern	NA	X	X	X	X	X	X	GLODAPv2	Yes
06AQ20141202	ANT-XXX/2	Polarstern	X	X	X	X	X	X	X	This work	Yes
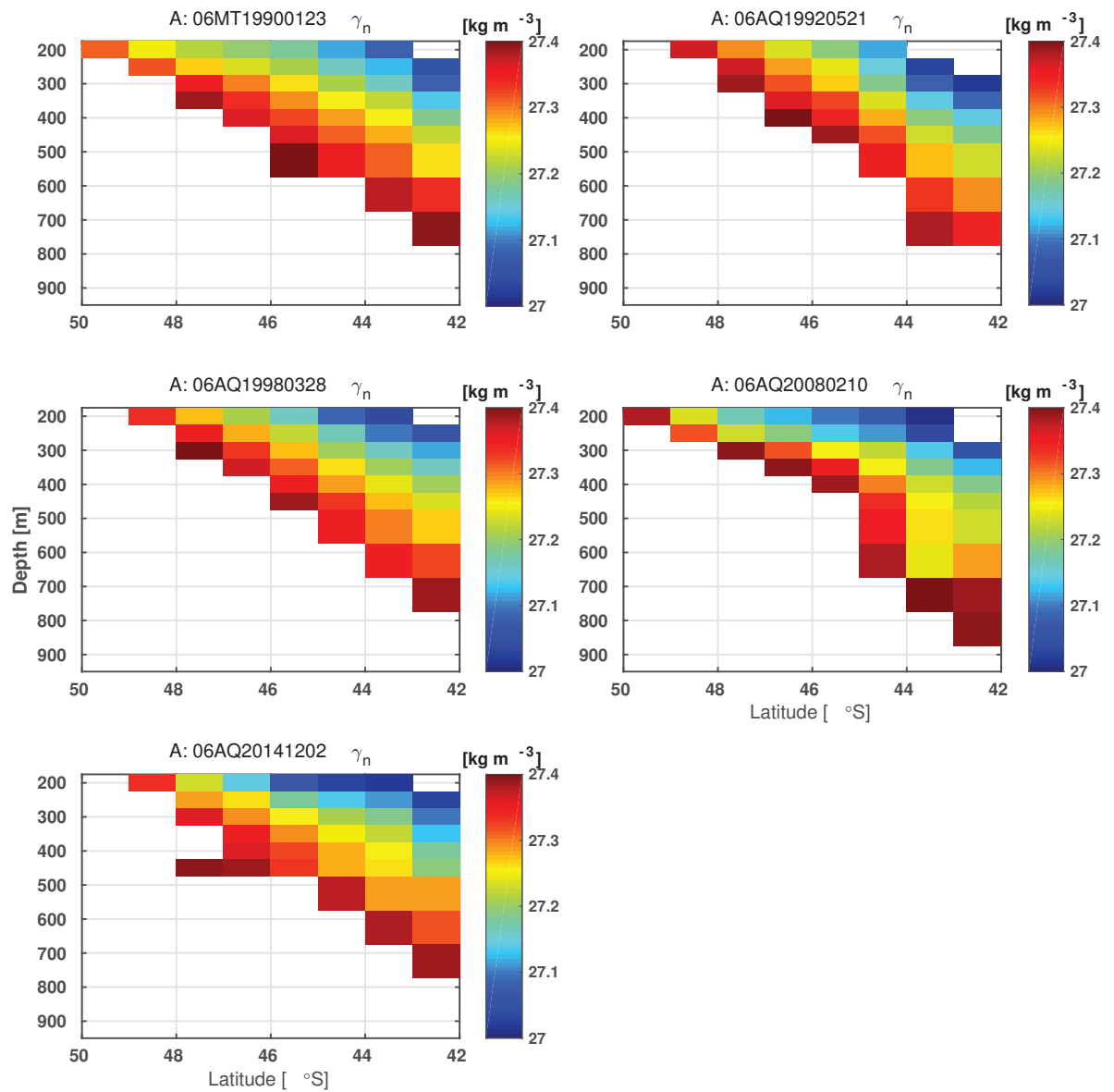
Fig. S1 AAIW water masses of the cruises (1990, 1992, 1998, 2008 and 2014) as selected within the neutral density range of $27 < \gamma_n < 27.4$.
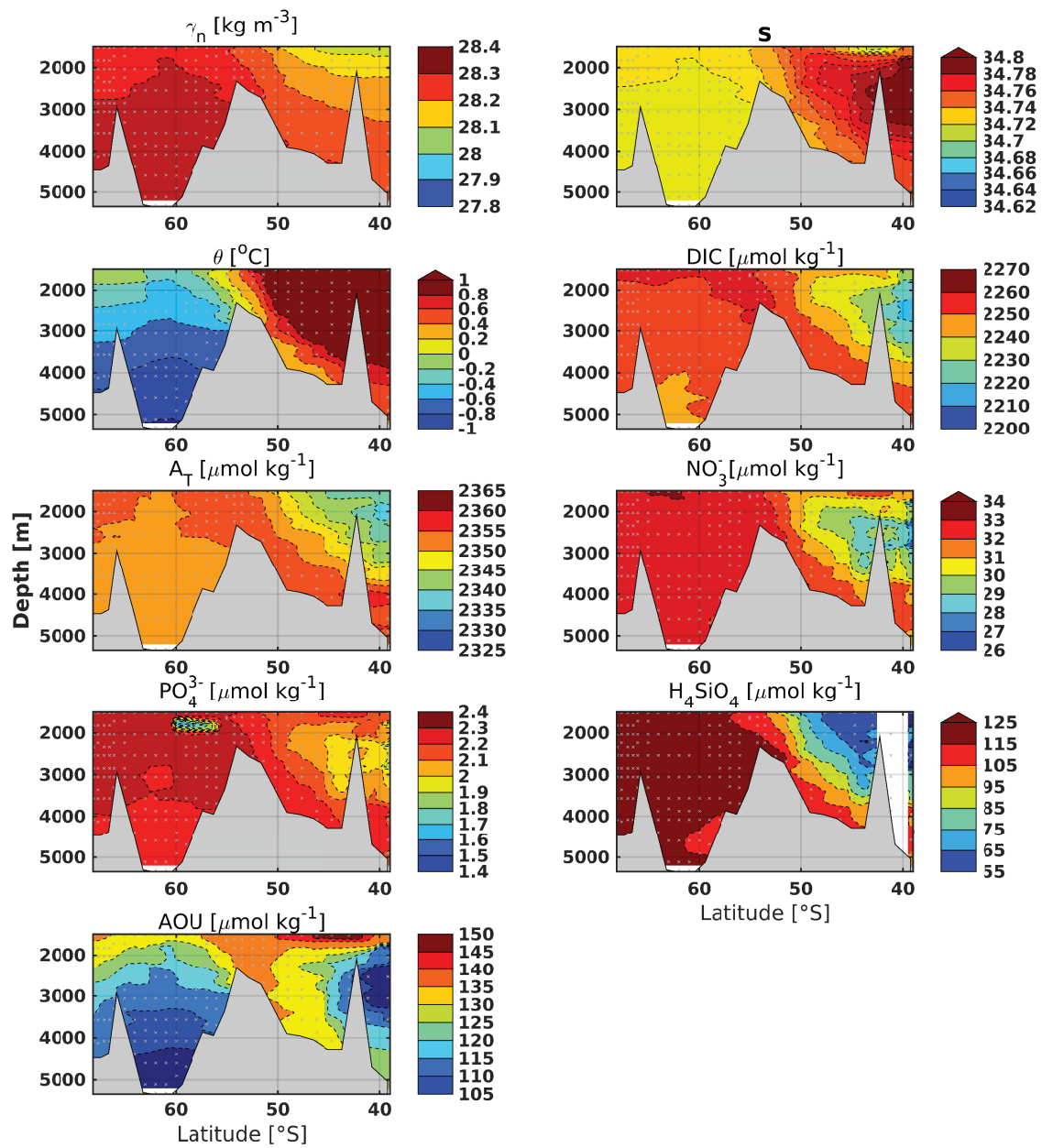
Fig. S2 Sections (1501-6000 m) along the Prime Meridian from Polarstern ANT-XXX/2 (2014): neutral density neutral density (γ_n), salinity (S), potential temperature (θ), dissolved inorganic carbon (DIC), total alkalinity (A_T), nitrate (NO_3), phosphate (PO_4), silicic acid (H_4SiO_4) and Apparent Oxygen Utilization (AOU). Grey dots indicate sampling stations.
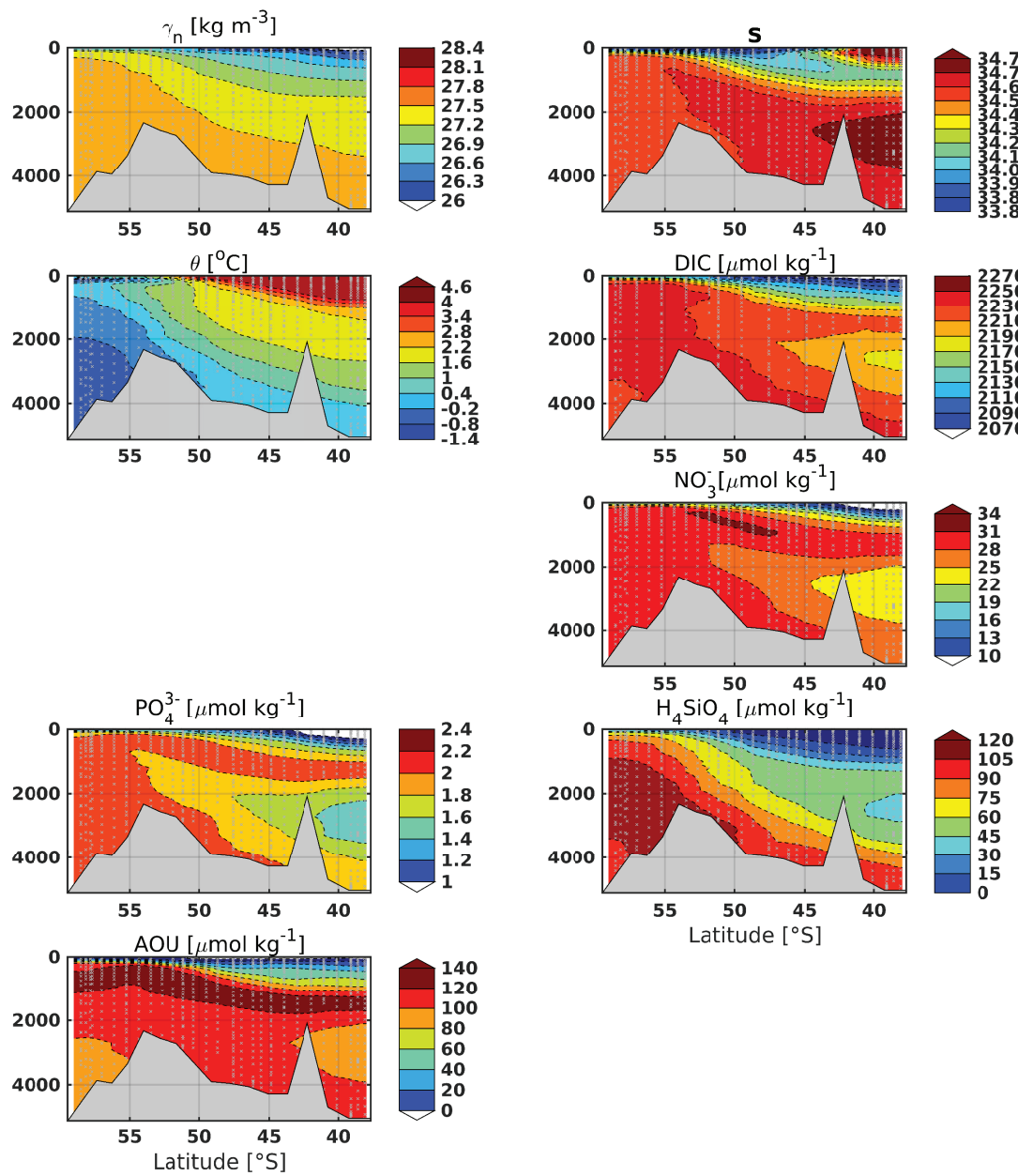
Fig. S3 Sections along the Prime Meridian from Meteor 06MT (1990): neutral density neutral density (γ_n), salinity (S), potential temperature (θ), dissolved inorganic carbon (DIC), nitrate (NO$_3$), phosphate (PO$_4$), silicic acid (H$_4$SiO$_4$) and Apparent Oxygen Utilization (AOU). Grey dots indicate sampling stations.
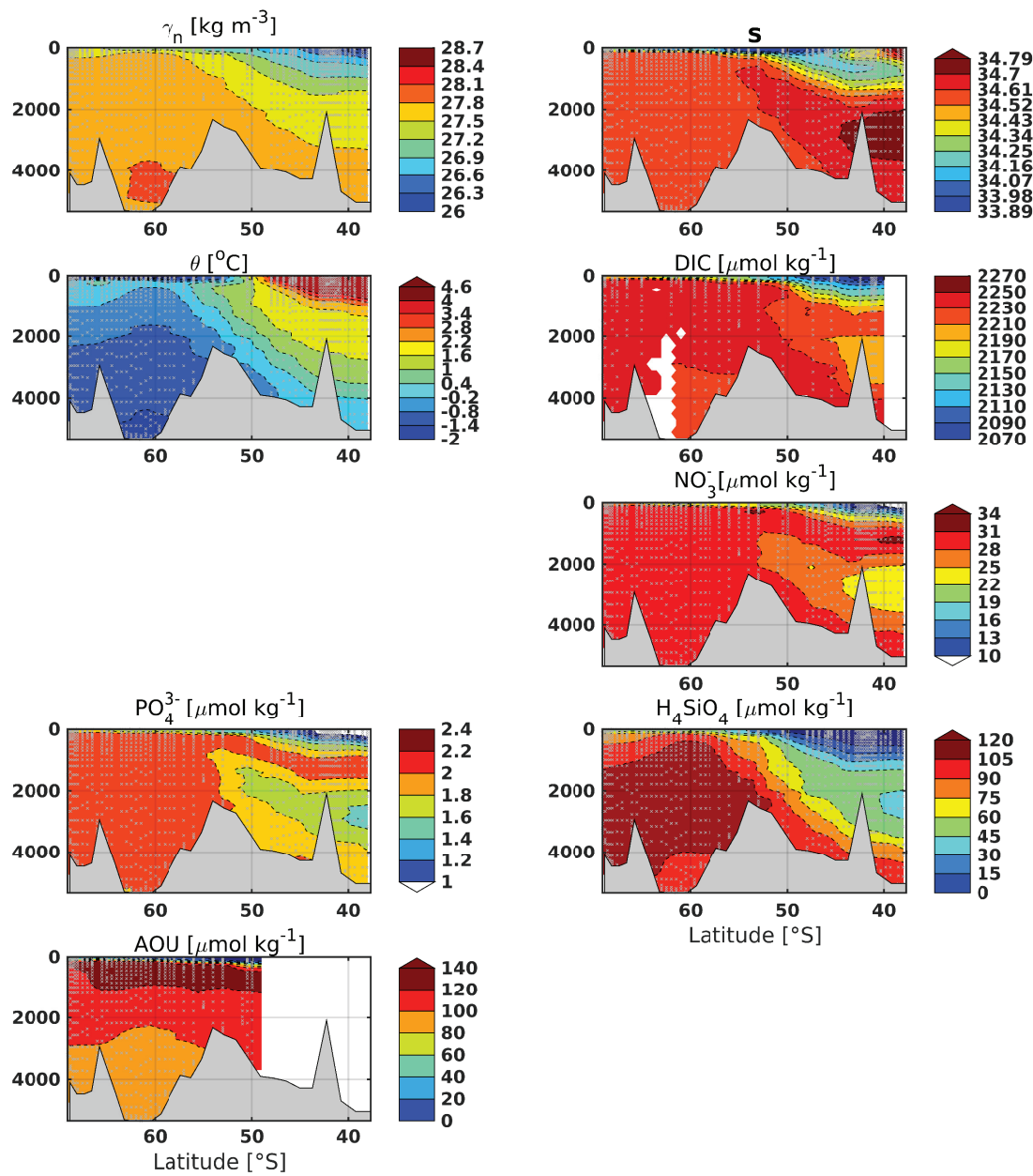
Fig. S4 Sections along the Prime Meridian from Polarstern ANT-X/4 (1992): neutral density neutral density (γ_n), salinity (S), potential temperature (θ), dissolved inorganic carbon (DIC), nitrate (NO_3), phosphate (PO_4), silicic acid (H_4SiO_4) and Apparent Oxygen Utilization (AOU). Grey dots indicate sampling stations.
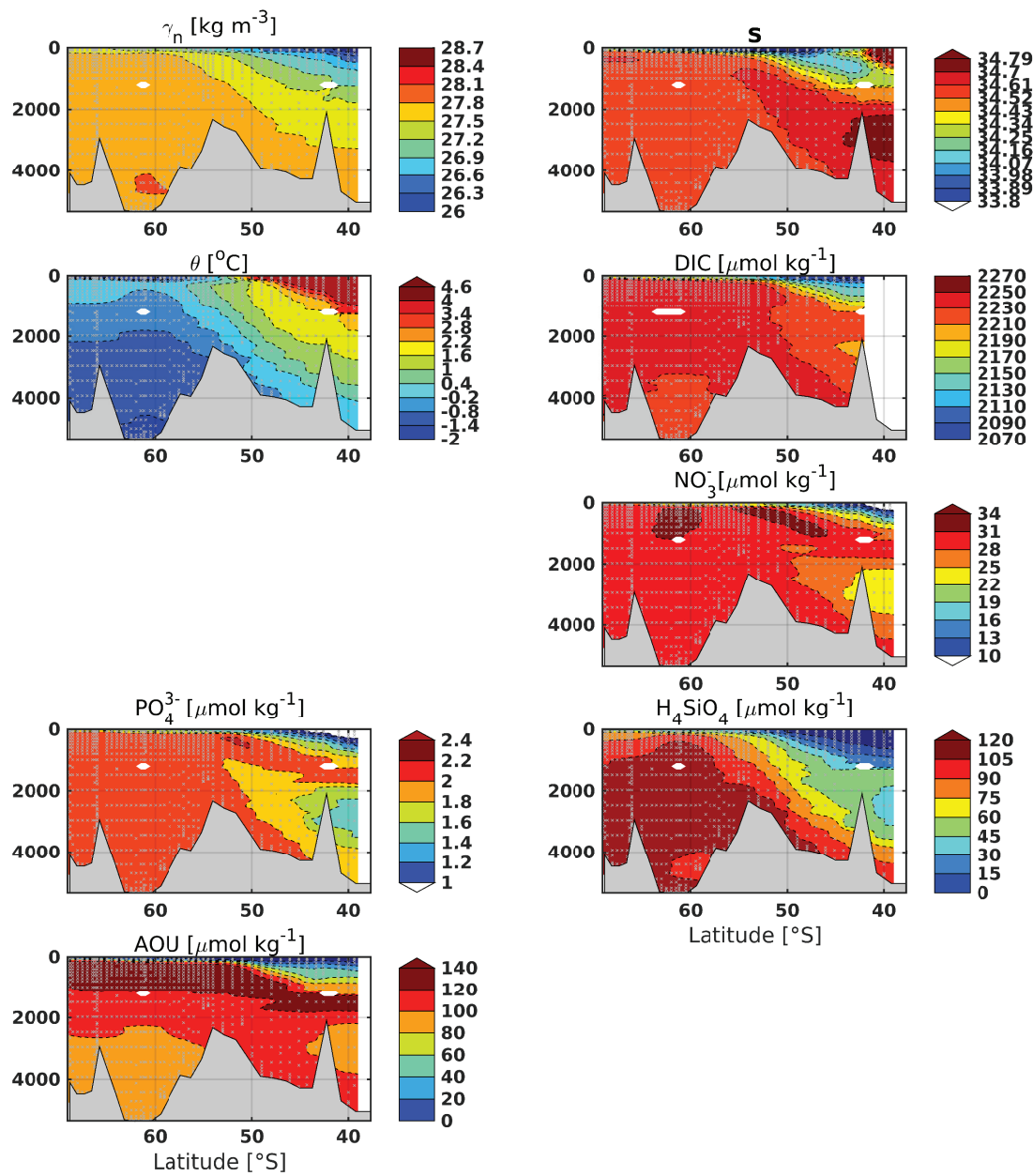
Fig. S5 Sections along the Prime Meridian from Polarstern ANT-XV/4 (1998): neutral density neutral density (γ_n), salinity (S), potential temperature (θ), dissolved inorganic carbon (DIC), nitrate (NO$_3$), phosphate (PO$_4$), silicic acid (H$_4$SiO$_4$) and Apparent Oxygen Utilization (AOU). Grey dots indicate sampling stations.
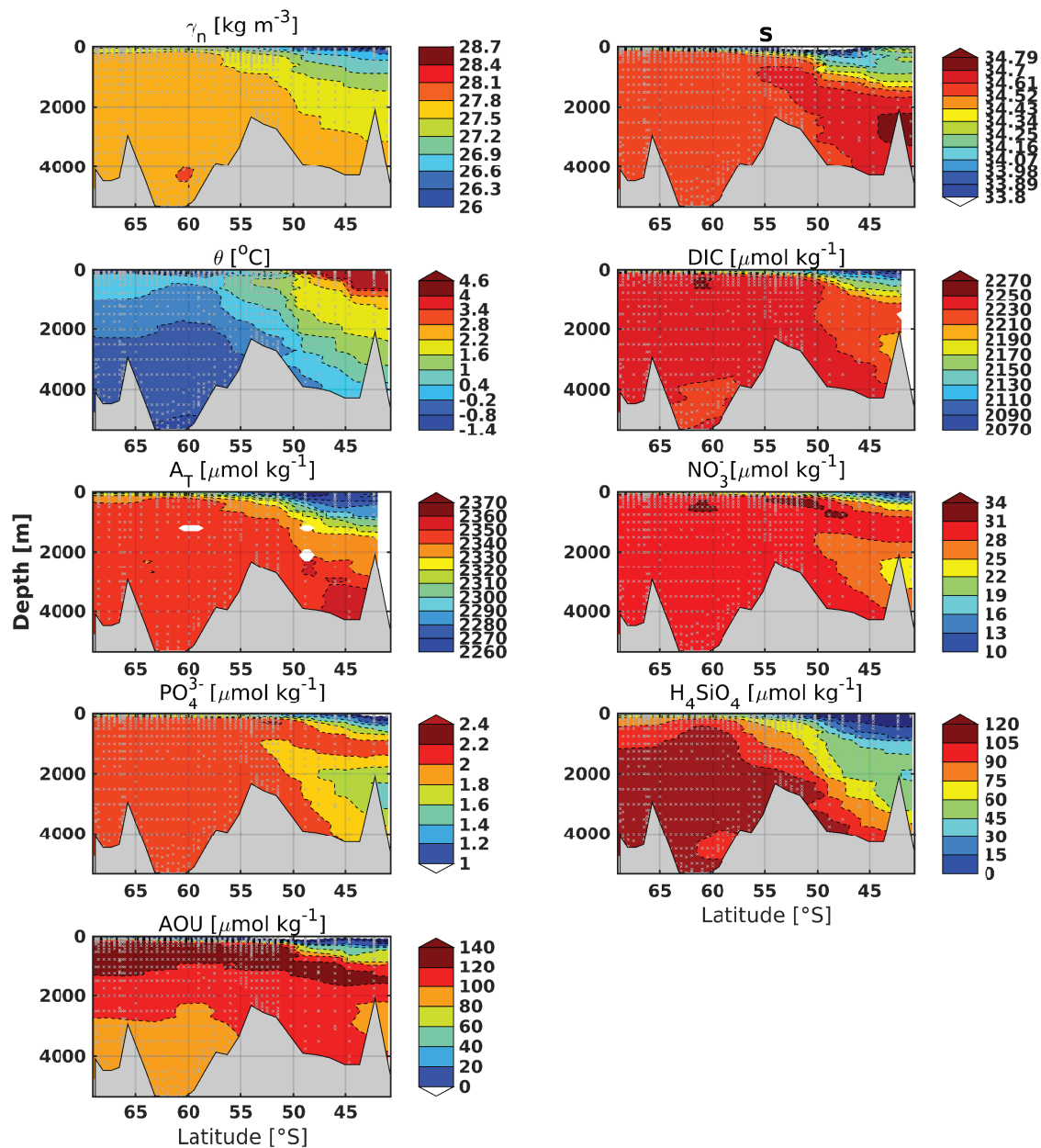
Fig. S6 Sections along the Prime Meridian from Polarstern ANT-XXIV/3 (2008): neutral density neutral density (γ_n), salinity (S), potential temperature (θ), dissolved inorganic carbon (DIC), total alkalinity (A_T), nitrate (NO_3), phosphate (PO_4), silicic acid (H_4SiO_4) and Apparent Oxygen Utilization (AOU). Grey dots indicate sampling stations.
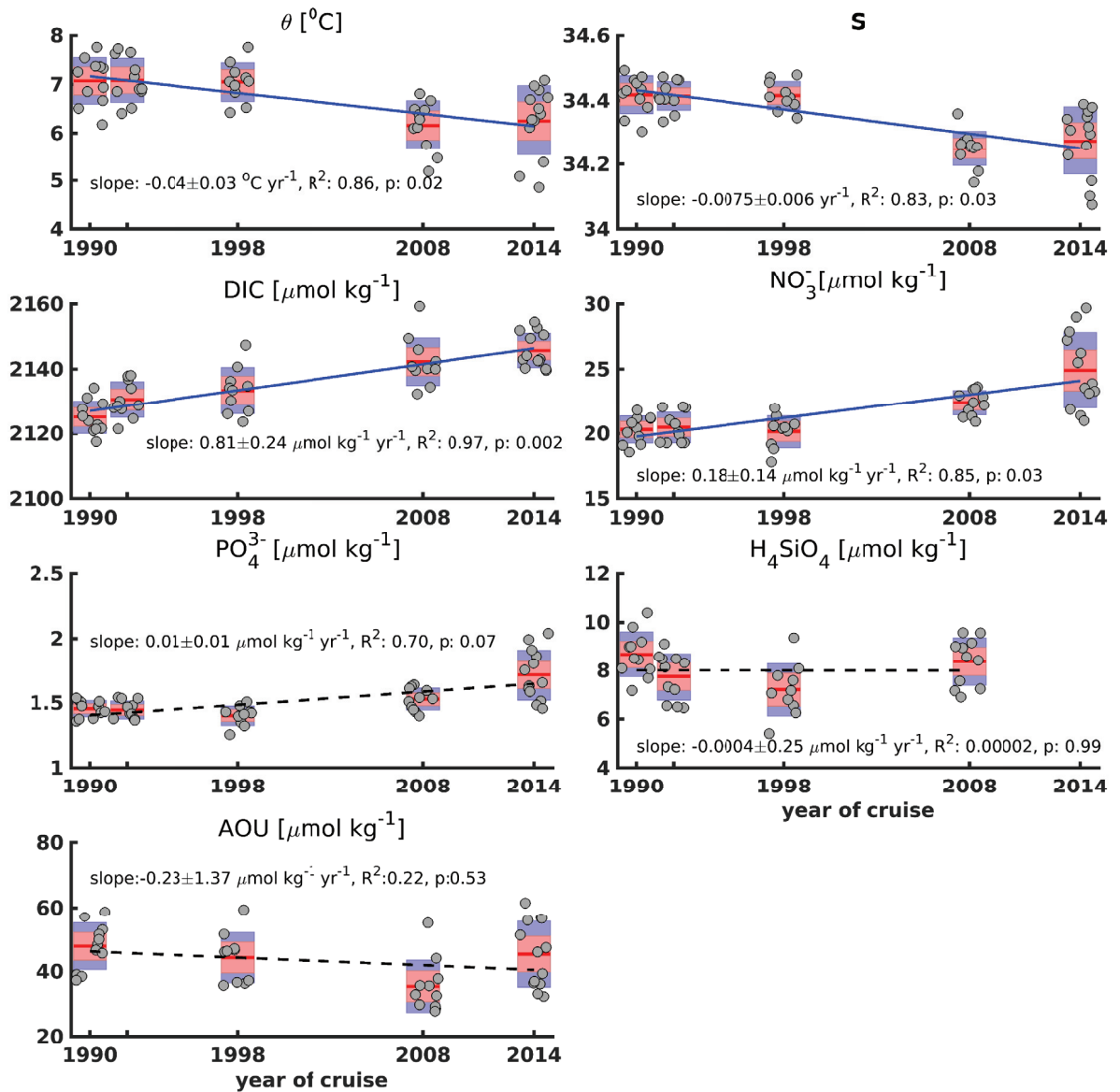
Fig. S7 Time series from 1990 to 2014 of gridded potential temperature (θ), salinity (S), dissolved inorganic carbon (DIC), nutrient (NO_3^-, PO_4^{3-} and H_4SiO_4) and Apparent Oxygen Utilization (AOU) variability in the neutral density range $27 < \gamma_n <= 27.1$. The red horizontal line represents the mean for each cruise. The light red bar represents the 95% confidence-interval for the mean. The violet color indicates plus/minus one standard deviation. Non-overlapping confidence intervals indicate significant differences between means at the 5% level of significance. The raw data are shown as gray circles, with random horizontal dispersion introduced to improve the visibility of the data points. Time trends (μmol kg^{-1} yr^{-1}) of DIC, NO_3^-, PO_4^{3-}, H_4SiO_4 and AOU have been estimated by linear regression of cruise mean values against time. The significant trends are indicated by blue solid lines and the dashed black lines represent statistically insignificant trends. The slope and p-value shown in the figure are for the trend which is calculated from the five average values of the individual cruises.

Fig. S8 Time series from 1990 to 2014 of gridded potential temperature (θ), salinity (S), dissolved inorganic carbon (DIC), nutrient (NO_3^-, PO_4^{3-} and H_4SiO_4) and Apparent Oxygen Utilization (AOU) variability in the neutral density range $27.1 < \gamma_n <= 27.2$. The red horizontal line represents the mean for each cruise. The light red bar represents the 95% confidence-interval for the mean. The violet color indicates plus/minus one standard deviation. Non-overlapping confidence intervals indicate significant differences between means at the 5% level of significance. The raw data are shown as gray circles, with random horizontal dispersion introduced to improve the visibility of the data points. Time trends (μmol kg^{-1} yr^{-1}) of DIC, NO_3^-, PO_4^{3-}, H_4SiO_4 and AOU have been estimated by linear regression of cruise mean values against time. The significant trends are indicated by blue solid lines and the dashed black lines represent statistically insignificant trends. The slope and p-value shown in the figure are for the trend which is calculated from the five average values of the individual cruises.

Fig. S9 Time series from 1990 to 2014 of gridded potential temperature (θ), salinity (S), dissolved inorganic carbon (DIC), nutrient (NO_3^-, PO_4^{3-} and H_4SiO_4) and Apparent Oxygen Utilization (AOU) variability in the neutral density range $27.2 < \gamma_n <= 27.3$. The red horizontal line represents the mean for each cruise. The light red bar represents the 95% confidence-interval for the mean. The violet color indicates plus/minus one standard deviation. Non-overlapping confidence intervals indicate significant differences between means at the 5% level of significance. The raw data are shown as gray circles, with random horizontal dispersion introduced to improve the visibility of the data points. Time trends (μmol kg^{-1} yr^{-1}) of DIC, NO_3^-, PO_4^{3-}, H_4SiO_4 and AOU have been estimated by linear regression of cruise mean values against time. The significant trends are indicated by blue solid lines and the dashed black lines represent statistically insignificant trends. The slope and p-value shown in the figure are for the trend which is calculated from the five average values of the individual cruises.

Fig. S10 Time series from 1990 to 2014 of gridded potential temperature (θ), salinity (S), dissolved inorganic carbon (DIC), nutrient (NO_3^-, PO_4^{3-} and H_4SiO_4) and Apparent Oxygen Utilization (AOU) v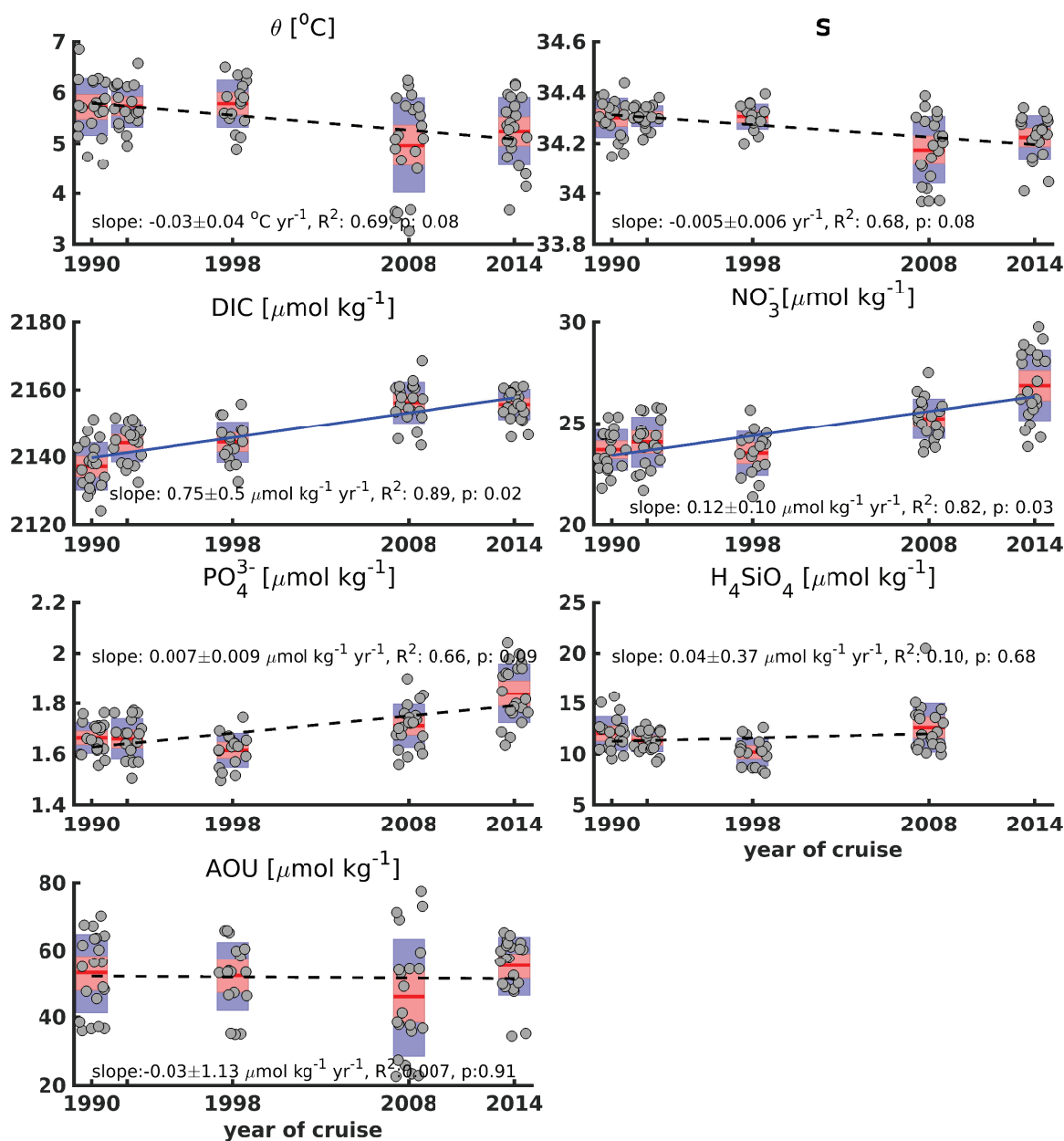ariability in the neutral density range $27.3 < \gamma_n < 27.4$. The red horizontal line represents the mean for each cruise. The light red bar represents the 95% confidence-interval for the mean. The violet color indicates plus/minus one standard deviation. Non-overlapping confidence intervals indicate significant differences between means at the 5% level of significance. The raw data are shown as gray circles, with random horizontal dispersion introduced to improve the visibility of the data points. Time trends ($\mu mol\ kg^{-1}\ yr^{-1}$) of DIC, NO_3^-, PO_4^{3-}, H_4SiO_4 and AOU have been estimated by linear regression of cruise mean values against time. The significant trends are indicated by blue solid lines and the dashed black lines represent statistically insignificant trends. The slope and p-value shown in the figure are for the trend which is calculated from the five average values of the individual cruises.
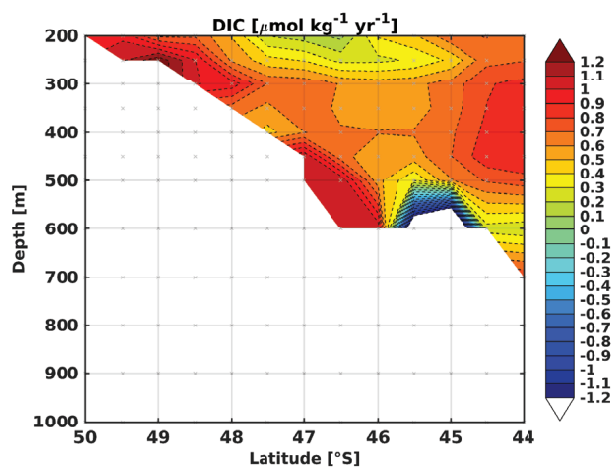
Fig. S11 Inferred time rates of changes for gridded dissolved inorganic carbon (DIC; μmol kg^{-1} yr^{-1}) in the core of AAIW here defined by the neutral density range $27 < \gamma_n < 27.4$ along the Prime Meridian in the latitude range of 44-50°S. The trend was estimated from the period of 1990-2012.

Chapter 4

Drivers of interannual variability of summer Mixed Layer Depth in the Southern Ocean between 2002-2011

Drivers of interannual variability of summer Mixed Layer Depth in the Southern Ocean between 2002-2011

E. Panassa[1], C. Völker[1], D. Wolf-Gladrow[1] and J.Hauck[1]

[1] Alfred Wegener Institute Helmholtz Centre for Polar and Marine Research, Am Handelshafen 12, 27570 Bremerhaven, Germany

Abstract   Climate change projections indicate that there will be warming and an intensification of westerly winds in the Southern Ocean (SO) in the future. These two forcings potentially have opposing effects on the depth of the surface mixed layer. Here, we investigate how changes in atmospheric surface air temperature (SAT) and zonal wind speed (uwind) impact mixed-layer depth (MLD) in the SO (south of 30°S) during summer, the season of main biological activity. We use gridded MLD data from observations and atmospheric reanalysis data of uwind and SAT in the SO to assess summer MLD variability and its potential drivers. With a model-based sensitivity experiment, we quantify the relative contributions of uwind versus SAT forcing on the summer MLD in the decade 2002-2011. Wind-induced changes dominate over temperature-induced changes of the MLD between 2002 and 2011. We find a positive trend of summer MLD in the Antarctic Zone (AZ) of the Atlantic and Indian Ocean sectors. Our model-based sensitivity study suggests that the summer MLD shows a zonally asymmetric response to recent atmospheric forcing. In the Pacific and Australian sectors, cooling and intensification of uwind jointly result in a deepening of the mixed layer. In the Atlantic and Indian sectors, the MLD responds differently north and south of the Antarctic Polar Front (APF). A deepening south of the APF is caused by the increase in uwind whereas the decrease in uwind and warming act in concert to result in a shoaling of the MLD north of the APF.

4.1 Introduction

The Southern Ocean (SO) is a key region for the global carbon cycle and the climate system (*Marshall and Speer*, 2012; *Frölicher et al.*, 2015). It takes up about 40% of the total anthropogenic carbon that enters the ocean (*Khatiwala et al.*, 2009; *Gruber et al.*, 2009) and is responsible for about 80% of upwelling of nutrient-rich deep waters (*Lumpkin and Speer*, 2007; *Talley*, 2013). The cycling of carbon in this region depends on mixed-layer (ML) dynamics, wind-driven Ekman transport and eddy fluxes (*Verdy et al.*, 2007; *Sallée et al.*, 2012; *Sabine et al.*, 2004). ML variability controls the availability of light and nutrients for phytoplankton in spring and summer as well as the grazing pressure by zooplankton (*Carranza and Gille*, 2015; *Fauchereau et al.*, 2011; *Venables and Moore*, 2010; *Llort et al.*, 2015). Phytoplankton productivity, in turn, is a main driver of the Southern Ocean CO_2 uptake in spring and summer (*Lenton et al.*, 2013).

Over the last decades, observational evidence has revealed a strengthening of the westerly winds in the SO, which is supported by model studies (*Marshall*, 2003; *Thompson et al.*, 2011; *Swart and Fyfe*, 2012). This is related to the positive trend in the Southern Annular Mode (SAM) index in response to the complex interaction between the stratospheric ozone depletion and the increase in the atmospheric greenhouse gas concentrations (*Thompson et al.*, 2011; *Lee and Feldstein*, 2013; *Abram et al.*, 2014). The positive trend in the SAM is expected to induce stronger summer wind stress (*Thompson et al.*, 2011; *Fogt et al.*, 2009), suggesting that the effect of summer wind forcing might dominate over buoyancy forcing with respect to summer mixed layer depth (MLD) variability. With the exception of the SAM trend, recent changes in the high-latitude Southern Hemisphere surface climate can largely be explained by internal climate variability (*Jones et al.*, 2016b).

The Southern Ocean MLD is highly sensitive to climate change and variability (*Sallée et al.*, 2010a; 2013; *Hauck et al.*, 2015). It is, however, not clear how the effects of the global warming signal (increased stratification *Gille*, 2008) and the wind signal (decreased stratification *Thompson et al.*, 2011), that occur simultaneously in the SO, will impact mixed layer (ML) dynamics in the future (*Hauck et al.*, 2015). It is therefore critical to understand recent effects of wind intensification and temperature trend and variability on ML dynamics.

The positive trend in the SAM has led to zonally-asymmetric anomalies in MLD caused by heat-flux anomalies associated with SAM (*Sallée et al.*, 2010a). On longer time scales, we might expect global warming to have a stronger effect on the summer MLD than the SAM signal. While SO warming is projected to significantly shoal the summer MLD in the subtropical zone in simulations of the 21st century, a suite of eight models disagrees about the sign of MLD change south of 44°S (*Hauck et al.*, 2015).

During summer, the mixed layer depth in the Southern Ocean is relatively shallow (MLD < 90 m) compared to other seasons because high irradiance and comparatively low wind stress lead to stratification. Strong wind events (summer storms), however, can destabilize the water column profoundly and deepen the ML, which consequently leads to enhanced nutrient (Fe, Si, or nitrate depending on the region) supply from subsurface waters to the euphotic zone and increased phytoplankton productivity (*Carranza and Gille*, 2015). Mechanisms that drive the summer ML variability in the SO were explored at the subseasonal timescale (*Carranza and Gille*, 2015).

ML deepening is caused mainly by wind-induced mixing, surface cooling, and/or Ekman pumping driven by the wind stress curl (*Carranza and Gille*, 2015). The physical mechanisms that link the changes in wind speed with those in MLD are the turbulent kinetic energy input through the generation and breaking of waves (*Denman*, 1973). In contrast, temperature impacts MLD by changing the density gradient. The effect of Ekman pumping can change the stratification through the input of denser water.

In this study, we analyse the summer MLD variability in the period 2002-2011 and attempt to unravel whether this variability is dominantly driven by wind or buoyancy forcing. The period 2002-2011 is characterized by a positive phase of the SAM index (*Jones et al.*, 2016b), which corresponds to a positive trend in zonal wind speed.

We chose to focus on the summer season because (1) the SAM trend is strongest in summer (*Fogt et al.*, 2009; *Thompson et al.*, 2011), and (2) the CO_2 uptake in the SO is a balance between outgassing in winter and uptake in summer when biology draws down CO_2 (*Lenton et al.*, 2013). Biological production might respond to changes in MLD in the future and it is neither understood whether the wind or the warming signal will be the dominant, driver nor how the variability in the summer MLD will affect the light and nutrient availability in the future (*Hauck et al.*, 2015).

We analyse the decade 2002-2011 because of an insufficient amount of Argo data before 2002, which consequently has very low spatial coverage in the SO (*Cabanes et al.*, 2013). This period was also used to assess the reinvigoration of the SO carbon sink (*Landschützer et al.*, 2015) and to investigate the potential connection between summer MLD and chlorophyll variability at sub-seasonal time scales (*Carranza and Gille*, 2015). We therefore focus on the period 2002-2011 in the context of strong interannual to decadal variability (*Jones et al.*, 2016b; *Landschützer et al.*, 2015; *DeVries et al.*, 2017). While this time-series is not long enough to identify a trend caused by climate change (*Jones et al.*, 2016b), it serves as a case study on a period characterized by a positive phase of the SAM index and a positive trend in wind speed. The changes are not necessarily related to climate change but are interpreted as a signal of interannual to decadal variability.

In the first part of our study, we analysed a global dataset derived from observations

and remote sensing of summer MLD and its potential drivers (zonal wind speed, near-surface air temperature). In the second part of our study we combined observations with a model-derived sensitivity analysis of MLD to quantified the relative contributions of wind and air temperature forcing on the MLD variability.

4.2 Data and methods

4.2.1 Atmospheric variables

We used the monthly ECMWF ERA-Interim reanalysis for the period 2002-2011 of 10 m zonal surface wind speed (*Dee et al.*, 2011) and 2 m near-surface air temperature (SAT). These are all available on http://www.ecmwf.int/en/research/climate-reanalysis/ era-interim with a spatial resolution of 1°x1°.

   We used the climatological CORE2 atmospheric forcing fields (*Large and Yeager*, 2009) for our model simulation. This data set includes six-hourly fields of zonal and meridional wind speed, near-surface air temperature, specific humidity, sea-level pressure, short- and longwave radiation and monthly precipitation.

4.2.2 Ocean variables

We used monthly surface gridded sea surface temperature (SST) fields from ECMWF ERA-Interim reanalysis available on http://www.ecmwf.int/en/research/climate-reanalysis /era-interim. This data set has a spatial resolution of 1°x1° and we used the period of 2002 to 2011.

   We used also monthly observations of CORA4.0 gridded 3D fields and raw individual profile data of in-situ temperature and salinity from the CORIOLIS database received from the MyOcean Service Desk (http://www.myocean.eu/). The CORA4.0 dataset is from a variety of instruments, mainly from Argo floats, Expendable Bathythermoghraphs (XBT), conductivity-temperature-depth (CTD) and expendable CTD (XCTD) probes, moorings, buoys and sensors mounted on marine mammal. The quality control and the sequence of processing of this dataset is fully described in *Cabanes et al.* (2013). The spatial resolution is 0.5° in longitude and latitude, and the profiles were vertically interpolated on 152 standard levels from the ocean surface to 2000 m, the maximum depth reached by Argo floats (5 m resolution from surface at the depth of 100 m; 10 m resolution from 100 m to 800 m, and 20 m resolution from 800 m to 2000 m *Cabanes et al.*, 2013). The CORA4.0 dataset covers the period from 1990 to 2012 from which we extracted

the period 2002-2011. The pre-2002 period was not analysed because of the low spatial coverage of the observations.

For the mixed-layer depth calculation, we computed the potential density from the raw and gridded CORA4.0 temperature and salinity fields. We chose to use CORA4.0 gridded temperature and salinity fields assuming that the objective analysis methodology (*Bretherton et al.*, 1976) used for the gridding of the CORA4.0 dataset is robust. The analysis of variability and the ten-year trend would be flawed by using a time-series with major gaps. The mixed layer depth is defined as the depth z at which the potential density difference $\Delta\sigma(z) = \sigma(z) - \sigma(z_0)$ exceeds a specific threshold value, in our case 0.03 kg m^{-3} (*de Boyer Montégut et al.*, 2004) with $z_0 = 10$ m being the reference depth. For the model MLD calculation, we applied the same density criterion as in the analysis of the CORA4.0 data.

4.2.3 Statistical analyses

For each monthly time series of the variables, namely MLD, zonal wind speed (uwind), and near-surface air temperature (SAT) from observations, we estimated the mean seasonal cycle of the period 2002-2011 at each grid point and subtracted this mean seasonal cycle from the data to obtain the anomaly. We further only used the summer months (December, January and February) for the following analysis. Then at each grid-point of the anomaly fields we performed the following analyses:

(1) A linear regression model was applied to the anomaly data over time using the non-parametric Sen Slope estimator method (*Gilbert*, 1987), following the example of *Kahru et al.* (2009). The Sen Slope estimator method which uses the median slope of all lines through pairs of sample points was preferred over the simple least square regression because the Sen Slope method is robust (insensitive to outliers).

(2) MLD (response variable) was regressed against the potential physical drivers uwind and SAT (predictors) using multiple linear regression (MLR) analysis including the interaction between the uwind and SAT and all quadratic terms (Eq. 4.3, supplementary material). Taking into account the interaction and quadratic terms in our MLD regression model increased the percentage of variance explained slightly (Figure 4.10, supplementary material). However, the additional terms also increased the complexity of the regression model. The Akaike Information Criterion (AIC; *Akaike*, 1973) provides a measure of the optimality of models in the sense of a trade-off between the model complexity (measured by the number of model parameters, including the variance of the additive normal noise) and the goodness-of-fit (measured by the logarithm of the maximum likelihood for the data). Models with lower AIC are more optimal. However, if the magnitude of the dif-

ference in AIC is less than 2 the difference is not significant and one should go for the simpler model. In most of the Southern Ocean, the AIC of the more complex model (with interactions) is larger than that of the simpler model (no interactions, no quadratic terms; Figure 4.11, supplementary material) or the magnitude of the difference in AIC is less than 2. We therefore in the main text show the regression model with no interaction and quadratic terms:

$$\text{MLD} = \beta_0 + \beta_1 * \text{uwind} + \beta_2 * \text{SAT} + \xi \qquad (4.1)$$

where β_0 represents the model intercept, β_1 and β_2 represent the regression coefficient slopes of MLD onto uwind, SAT, and ξ represents the residual.

4.2.4   Ocean model

We used the Massachusetts Institute of Technology general circulation model (MITgcm, *Marshall et al.*, 1997). The model solves the primitive equations under the Boussinesq approximation and is discretized on a latitude-longitude-depth Arakawa C-grid. Our computational domain is nearly global but excludes the Arctic Ocean (cut-off at 80°N). The latitudinal resolution varies from 0.38° to 2° with the higher resolution in the Southern Ocean and around the equator. The longitudinal resolution is constantly 2°. In the vertical, we use 30 vertical layers with 10 m thickness at the surface and the thickness increases gradually with depth to a 500 m thickness to a maximum depth of 5700 m. The model uses the Gent-McWilliams eddy parameterization (*Gent and McWilliams*, 1990), sea-ice dynamics and thermodynamics (*Losch et al.*, 2010) and the nonlocal K-Profile parameterization (KPP) boundary layer mixing scheme (*Large et al.*, 1994) for the vertical mixing within the mixed layer. The physical model set-up is the same as in (*Hauck et al.*, 2013; 2016).

4.2.5   Sensitivity experiments

In the following, we describe our approach to evaluate the relative impacts of zonal wind speed and buoyancy forcing on summer MLD with a set of sensitivity experiments using the MITgcm. We followed a two-step approach, in which we first used the model to estimate the sensitivities of MLD to both wind and buoyancy forcing separetely. In a second step we multiplied this sensitivity with the observed trends of atmospheric variables to gain insights into the potential change in MLD. The advantage of this approach is that, albeit based on a linearization, it is causal, rather than just based on empirical correlation only, as our data analysis (section 4.2.3). It is thus better able to separate how much each driver contributes to the MLD trend in the decade 2002-2011.

To estimate the sensitivity of MLD to changes in the zonal wind speed (uwind) or near-surface air temperature (SAT), we first performed a control run with no perturbation applied to simulate oceanic temperature and salinity fields. The model was started from a 100 year spin-up as in *Hauck et al.* (2016) and run for four years. We ran the model by prescribing climatological atmospheric forcing fields from CORE2 (i.e. air temperature, zonal and meridional components of wind speed, sea-level pressure, specific humidity, solar radiation and precipitation). We used bulk formulae (*Large and Yeager*, 2004) to calculate heat and freshwater fluxes from these forcing fields and from the modeled ocean state.

We perturbed the atmospheric side, namely either near-surface air temperature or zonal wind speed in sensitivity experiments to change atmospheric heat and fresh water fluxes and to investigate their separate impact on the MLD. The sensitivity runs are identical to the control run, except that we increased either uwind by 0.9 m s^{-1} (10% of SO maximum zonal wind), or SAT by 0.2 K at every grid point south of 30°S. The perturbation fields were applied separately during the summer season (December, January and February) only and we repeated this perturbation for the summer months of the following two years. This yields three different perturbed MLD fields from three different years for each variable perturbed.

To obtain the MLD sensitivity fields ($\alpha = \frac{\partial \mathrm{MLD}}{\partial \mathrm{uwind}}$, $\theta = \frac{\partial \mathrm{MLD}}{\partial \mathrm{SAT}}$) that represent the effect of each driver on the MLD change, respectively, we calculated the difference between the average of the perturbed MLD fields and the average of the control MLD fields and divided these model MLD anomaly fields by the applied perturbation for each year ($\frac{\partial \mathrm{MLD}}{\partial \mathrm{driver}} = \frac{\mathrm{MLD}_{\mathrm{perturbed}} - \mathrm{MLD}_{\mathrm{control}}}{\mathrm{perturbation}}$). In the following, we used the average of the model-derived MLD-sensitivity fields from the three summer seasons.

Finally, we combined the model-derived MLD-sensitivity fields to atmospheric forcing changes with the observed trends of these drivers. To do so, we linearized the summer MLD trend over the period 2002-2011 by multiplying the averaged MLD sensitivity field with the observed trend of the respective driver:

$$\Delta \mathrm{MLD} = \frac{\partial \mathrm{MLD}}{\partial \mathrm{uwind}} \Delta \mathrm{uwind} + \frac{\partial \mathrm{MLD}}{\partial \mathrm{SAT}} \Delta \mathrm{SAT} + \xi \qquad (4.2)$$

Here Δuwind and ΔSAT represent the trends of observed uwind and SAT over the period 2002-2011, respectively, which were all derived from ERA-Interim reanalysis data (zonal wind speed and near-surface air temperature), while the partial derivatives are the model-derived fields of MLD sensitivities (coefficient of linearization). ξ represents the residual term and ΔMLD is the observed MLD trend.

We chose to perturb zonal wind speed (rather than total wind speed) as the zonal component constitutes the largest part of the wind speed on monthly timescales in the

Southern Ocean and thereby has a major share in the MLD response. The zonal component is predicted to become stronger in the future (*Thompson et al.*, 2011) whereas the meridional component is smaller and not predicted, to the best of our knowledge, to change in the future. We found that regressions of zonal and of total wind speed on MLD have similar patterns and amplitudes (not shown) and we conclude that the results of our sensitivity experiments are insensitive to whether one chooses zonal or total wind speed.

We also performed the sensitivity experiment with a perturbed precipitation field $(2 \cdot 10^{-9}$ m s^{-1}, 10% of SO mean precipitation). The contribution of precipitation to the MLD trend reaches at most $2.7 \cdot 10^{-6}$ m year^{-1}, which is 6 orders of magnitude lower than the MLD trends we estimated from uwind or SAT. Therefore, we neglect the effect of precipitation in the following.

4.3 Results

4.3.1 Variability of mixed layer depth, zonal wind speed and air temperature
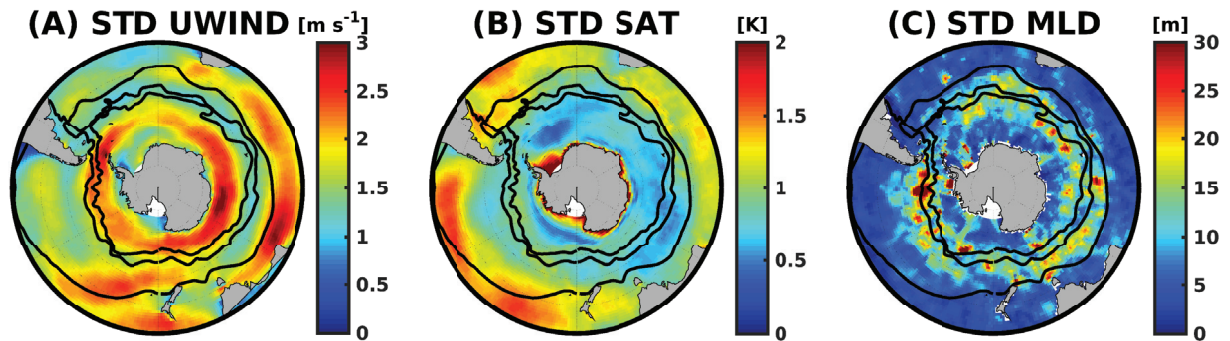
Figure 4.1: Standard deviation for the period 2002-2011 of the summer (A) zonal wind speed (uwind) from the ERA-Interim reanalysis (*Dee et al.*, 2011), (B) near-surface air temperature (SAT) from the ERA-Interim reanalysis and (C) mixed layer depth [MLD] from the CORA4.0 dataset (*Cabanes et al.*, 2013). The black contours represent the mean positions of the STF, SAF and APF (from north to south), respectively (*Orsi et al.*, 1995).

Maps of the standard deviation of summer zonal wind speed (uwind), near-surface air temperature (SAT) and MLD are shown in Figure 4.1 for the period of 2002-2011. Summer uwind exhibits the highest variability (2 to 3 m s^{-1}; approximately 10% of the mean) in the Antarctic Zone (AZ, south of the Antarctic Polar Front, APF) and in the Subtropical Zone (STZ, north of the Subtropical Front, STF) of the Indian sector of the SO (Figure

4.1A). In contrast, the variability of SAT is lowest in the AZ. Although the variability in SAT is strong (> 1.5 K, Figure 4.1B) in the STZ of the Atlantic and Pacific sectors and close to the Antarctic coast, the MLD in these regions shows weak variability (< 10 m; Figure 4.1C). In contrast, relatively strong MLD variability (15 to 30 m) occurs in the ACC region and the AZ. In the following we intend to unravel whether this variability contains a significant linear trend and whether we can relate the variability of summer MLD to the variability in uwind and SAT.

4.3.2   Linear trend analysis
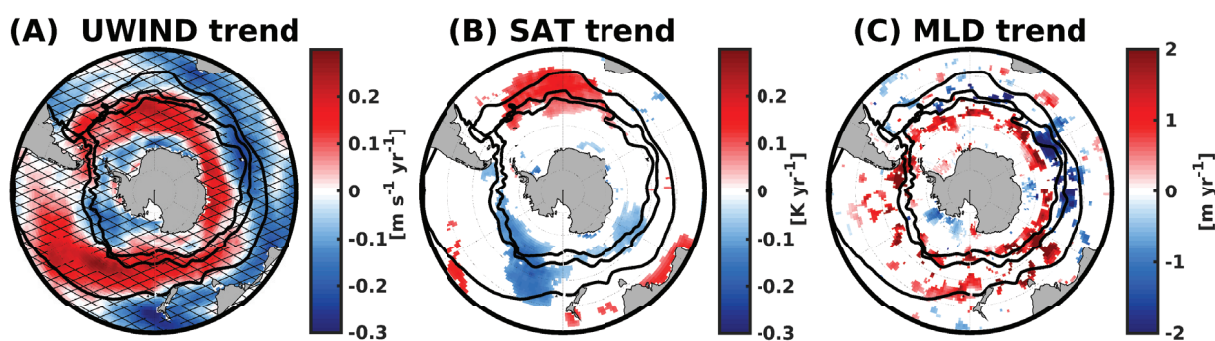
Figure 4.2: Summer trend for the period 2002-2011 of (A) the zonal wind speed (uwind) from the ERA-Interim reanalysis (*Dee et al.*, 2011), (B) 2 m near-surface air temperature (SAT) from the ERA-Interim reanalysis, (C) mixed layer depth (MLD) from the CORA4.0 dataset (*Cabanes et al.*, 2013). The wind speed trends that are not significant on the 95% level are overlain with hatching to show the tendency despite the dominance of interannual variability. The black contours represent the mean positions of the STF, SAF and APF (from north to south), respectively (*Orsi et al.*, 1995). Only significant trends on the 95% confidence level are shown for SAT and MLD.

Summer trend maps of zonal wind speed (uwind), near-surface air temperature (SAT) and MLD are shown in Figure 4.2 for the period of 2002-2011. A strong positive trend in uwind (up to 0.2 m s^{-1} year^{-1}) occurs in the Pacific sector of the Subantarctic Zone (SAZ, between the Subantarctic Front, SAF, and Subtropical Front, STF, Figure 4.2A). The Cross-Calibrated Multi-Platform (CCMP, *Atlas et al.*, 2011) winds show similar trends to ERA-Interim (Figure not shown). A significant positive trend in SAT occurs in the ACC region of the Atlantic sector and a negative trend is located south of the SAF of the Australian sector. A significant decrease in SAT of up to 0.1 K yr^{-1} is observed in one patch spanning the Polar Frontal Zone (PFZ, between the Antarctic Polar Front, APF, and SAF), SAZ and AZ of the Pacific Ocean (Figure 4.2B). The trend in sea surface temperature (SST; Figure 4.12, supplementary material) shows a similar pattern as that

in SAT, however, it shows a warming trend close to the Antarctic coast in contrast to SAT.

There is a significant and positive trend of the MLD in the AZ of the Atlantic and Indian sectors. Some patches of significant positive trends occur also in the Pacific and Indian sectors of the PFZ, and SAZ (Figure 4.2C). A significant negative trend occurs in the ACC region of the Indian sector.

The regions of strong ML deepening (regionally up to 2 m year^{-1}) co-occur with the regions where we observe a strong increase in uwind and fit partially with the zones where significant cooling occurs in the near-surface atmosphere. In the next section we test whether the variability in uwind and SAT can explain the MLD variability.

4.3.3   Multiple linear regression analysis (MLR)
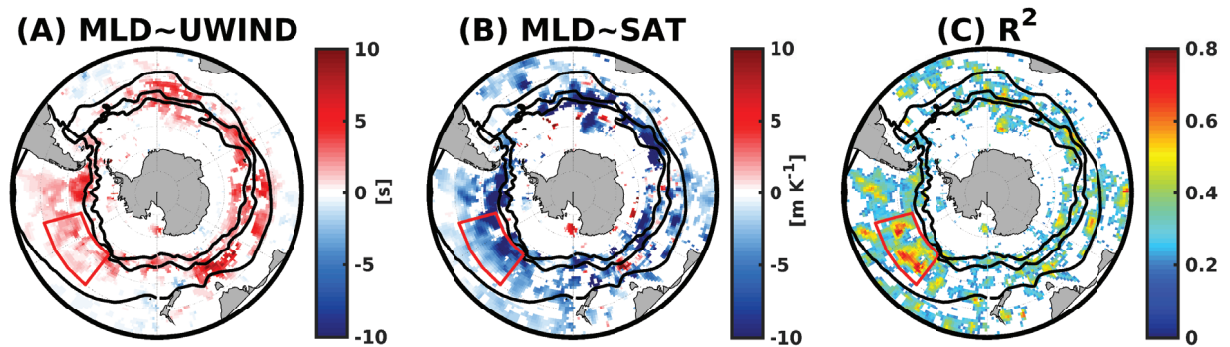
Figure 4.3: Shown are the regression coefficients of the multi linear regression of observed MLD anomalies during summer months against anomalies during summer months of zonal wind speed (uwind) and near-surface air temperature (SAT) anomalies [A and B, respectively]. In (C), we show the explained variance in MLD variability from both uwind and SAT variability (r-square). Only significant regression coefficients on the 95% level are shown. The black contours represent the mean positions of the STF, SAF and APF (from north to south), respectively (*Orsi et al.*, 1995). The red box shown in the figure represents the areas where we integrated uwind, SAT and MLD anomalies over time, respectively, and quantified their temporal relationship as a time-series (Figure 4.4).

In this section, we investigate the impact of summer zonal wind speed (uwind) and near-surface air temperature (SAT) variability on the observed summer MLD variability in the period of 2002 to 2011 by regressing the MLD anomalies against the uwind and SAT anomalies.

We find that MLD anomalies are positively correlated with uwind in the ACC region (Figure 4.3A). This signal extends further north to the STF in the eastern Pacific sector.

An increase of the MLD of $2-5$ m in the ACC region is associated with a 1 m s^{-1} increase in uwind. In contrast, MLD anomalies are negatively correlated with SAT (Figure 4.3B). A decrease of the MLD of $5-10$ m is associated with a 1 K increase in SAT. Only few patches show an increase of MLD when SAT increases. The regions, where the regression coefficients of MLD against uwind and against SAT are significant, overlap widely, but the regression coefficients have different signs. The combined effect of uwind and SAT on the MLD can explain up to 80% of its variability (Figure 4.1C). The highest values of explained variability in MLD ($R^2 > 0.4$) occur in the SAZ of the central and eastern Pacific sector. Generally more than 40% of the MLD variability are explained by uwind and SAT in the ACC region.
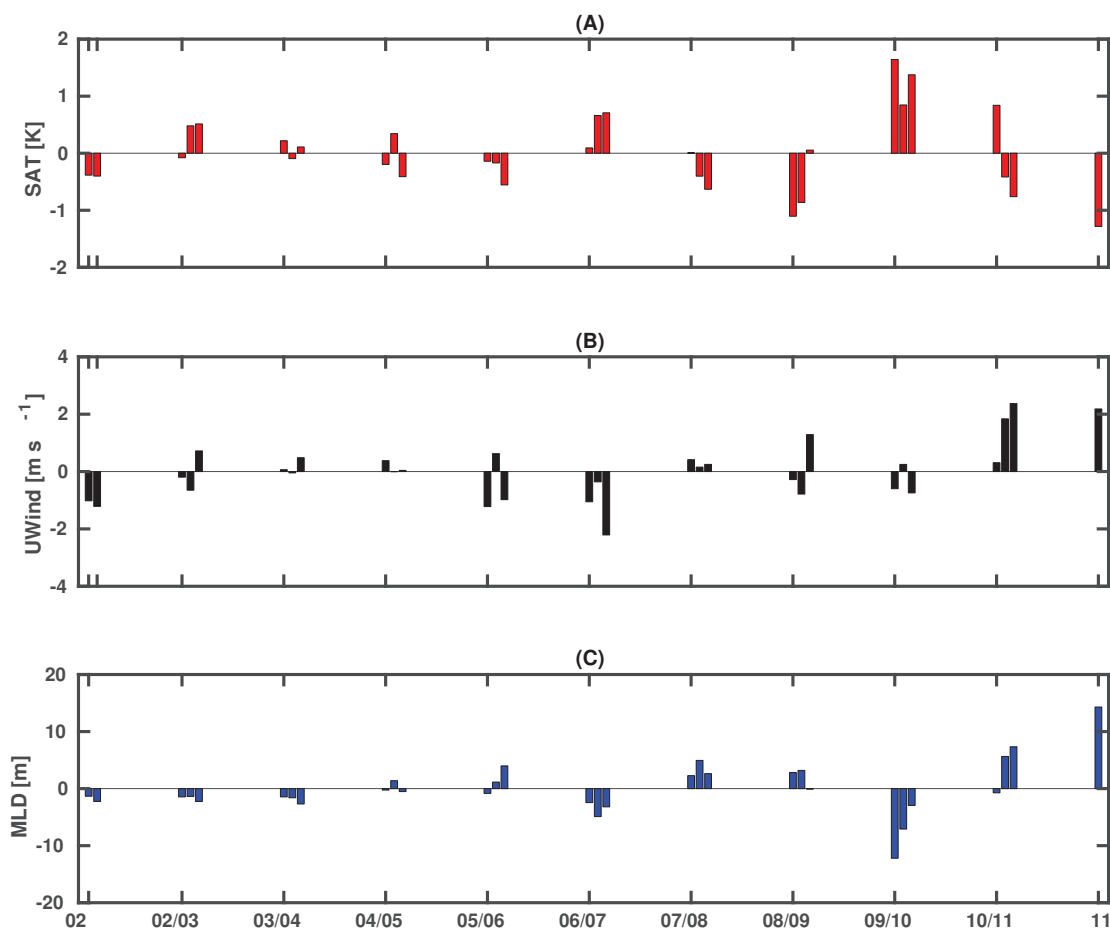
Figure 4.4: Shown are summer monthly (December to February) area-weighted anomalies of (A) near-surface air temperature (SAT, red bar), (B) zonal wind speed (uwind, black bar) and (C) the observed MLD (blue bar) in the central Pacific defined in the box (142 - 105°W, 55 - 40°S). In the central Pacific the correlation between anomalous MLD and uwind is 0.55, while the correlation between anomalous MLD and SAT is -0.80. The x-axis refers to summer months (DJF) from January 2002 to December 2011. The labels refer to the year.

We also examined the relationship between the time-series of the spatially averaged MLD, uwind, and SAT anomalies in one region where we found the largest coefficients of determination (R^2) in the central Pacific sector (40-55°S, 142-105°W, the box is shown in Figure 4.3). In this region, MLD has a negative regression coefficient with respect to SAT and a 5.5 m deepening of the MLD is associated with a 1 K decrease in SAT (correlation is $R = -0.80$, Figure 4.4A and Figure 4.4C). In contrast, MLD has a positive regression coefficient with respect to uwind and an increase of the MLD of 2.5 m is associated with a 1 m s^{-1} increase in uwind (correlation is $R = 0.55$, Figure 4.4B and Figure 4.4C). Thus, an anomalously deep MLD is associated with anomalously strong uwind and low SAT. The variability in SAT alone can explain about 64% of the variability in the MLD in this region, whereas, only 30% of the variability in MLD is explained by uwind alone. When taking into account both effects uwind and SAT, we can explain about 74% of MLD variability. Note that the two effects do not add up.

4.3.4 Linearization using model sensitivity experiments

Model evaluation

How does the model reproduce the summer mean MLD, the MLD seasonal cycle, and trend in comparison to the observations?

The modeled summer mean MLD (Figure 4.5A) compares reasonably well with the observed values (profiles and gridded data, Figure 4.5B and Figure 4.5C). The spatial patterns of summer MLD are reproduced by the model with a reasonable transition between the shallow MLD south of 60°S towards Antarctica, the deep MLD in the ACC region and the shallow MLD north of the ACC (Figure 4.5). Nevertheless, the model underestimates the MLD seasonal amplitude in the ACC region.

The climatological seasonal cycles of the MLD averaged south of 30°S from the model and from observations (gridded and individual profiles) are shown in Figure 4.5D. Similar patterns are observed for the MLD seasonal cycle derived from profile and gridded data (correlation coefficient $R = 0.99$, p-value for correlation different from zero <0.05, N=12). The MLD seasonal cycle from gridded data is approximately 10 m too shallow compared to the one calculated from individual profiles from January to May and 20 m too shallow between June and December. This is in line with the finding of *de Boyer Montégut et al.* (2004) that the MLD is 25% too shallow when the MLD is calculated using gridded temperature and salinity fields. The model (red dashed line) simulates the observed MLD seasonal cycle (from profiles, black solid line) reasonably well (correlation coefficient $R = 0.98$, p-value <0.05, N=12). However, the model MLD seasonal cycle is too shallow during summer and autumn (on average by 17 m between December and May) and too

deep in winter and spring (on average by 25 m between June and November) compared to the observations (profile data). There is no phase shift between the maxima and minima of modeled and observed seasonal cycles. The deepest MLD is found in September and the shallowest in January. The amplitude of the modeled seasonal cycle (155 m) is larger than the amplitudes of the MLD seasonal cycles calculated from observations (profile data: 103 m and gridded data: 91 m). This anomaly is common for general circulation models and is particularly pronounced in the SO. It has been suggested that this discrepancy could be caused by insufficiencies of the vertical mixing parameterization that general circulation models commonly use (*Huang et al.*, 2012; *Sen Gupta et al.*, 2009), or by an excess freshwater flux (*Sallée et al.*, 2013).
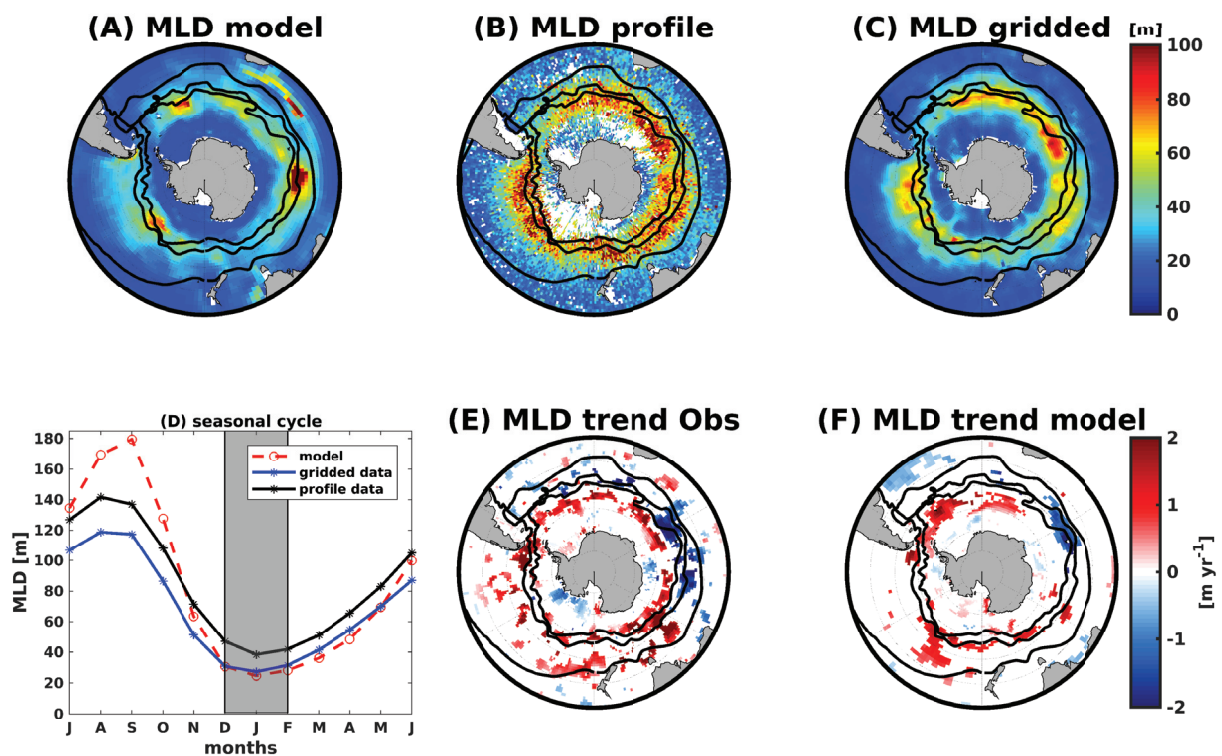
Figure 4.5: Mean summer (DJF) mixed layer depth (MLD), from (A) model and observations: (B) profile data averaged in 1x1° bins and (C) from gridded data, (D) MLD seasonal cycle (average south of 30°S) from model (red dashed line) and observations (from individual temperature and salinity profiles = black solid line; from gridded temperature and salinity data = blue solid line) in the period 2002-2011. In (D) summer season (DJF) is emphasized in the gray transparent band. Trends in summer of: (E) the mixed layer depth from observations (*Cabanes et al.*, 2013) and (F) from the model over the same period 2002-2011. The model was forced by the interannual varying atmospheric NCEP/NCAR surface wind fields (*Kalnay et al.*, 1996). Only significant trends on the 95% level are shown. The black contours represent the mean positions of the STF, SAF and APF (from north to south), respectively (*Orsi et al.*, 1995).

As an additional check of the model, we also calculated the summer MLD trend from a hindcast simulation with the same model set-up using the same methodology as for the observational data. We analysed output from a century-scale simulation where the model is forced by historic atmospheric CO_2 concentrations (*Le Quéré et al.*, 2016) and interannual varying atmospheric NCEP/NCAR forcing fields (*Kalnay et al.*, 1996). The model is spun-up from 1900 to 1947 and we ran the model for 69 years, from 1948 to 2016. This model simulation was submitted to the Global Carbon Budget 2017 and is the same physical set-up as in the Global Carbon Budget 2016 (*Le Quéré et al.*, 2016). The comparison of the modeled MLD trend (Figure 4.5F) to the observed one (Figure 4.5E) in the period 2002-2011 shows that the model is able to reproduce the pattern and amplitude of the observed trend in MLD. However, the model shows a smaller number of significant pixels with MLD deepening in the Indian Ocean south of the APF as in the observations.

4.4   Sensitivity experiments using the MITgcm

What drives the trend in MLD?

In the following, we attempt to unravel whether wind or buoyancy forcing is responsible for the observed summer MLD trend over the decade 2002-2011. We combine model results and observations to estimate the relative impacts of summer zonal wind speed and near-surface air temperature changes on the summer MLD as explained in section 4.2.5. This approach allows us to go beyond regression analysis and to derive causal relationships.

4.4.1   MLD trend caused by wind changes

The MLD sensitivity to uwind perturbation $\alpha = \frac{\partial \text{MLD}}{\partial \text{uwind}}$ is generally positive and it is highest ($\alpha > 20$ s) in the ACC region. It is close to zero south of 60°S and north of 35°S (Figure 4.6A). A strong positive trend in uwind occurs in the the PFZ and SAZ of the Pacific sector and in the AZ of the Atlantic and Indian sectors (Figure 4.6B, note that this figure is the same as Figure 4.2A but it includes the non-significant parts). A negative trend is found to the north and to the south of the positive trend. The product of the MLD sensitivity to uwind perturbation (α) and the actual observed uwind trend gives an estimate of the wind-induced MLD change (Figure 4.6C). A shoaling of the ML occurs in the PFZ and the STZ of the Indian sector and in the central PFZ of the Pacific sector. This is caused by the combination of a positive sensitivity α (Figure 4.6A) and a decrease in uwind (Figure 4.6B). In contrast, an uwind-driven MLD increase occurs in the SAZ

of the Pacific sector and stretches toward the AZ of the Atlantic and Indian sectors. In these regions high positive α values co-occur with an increase in uwind (Figure 4.6C).
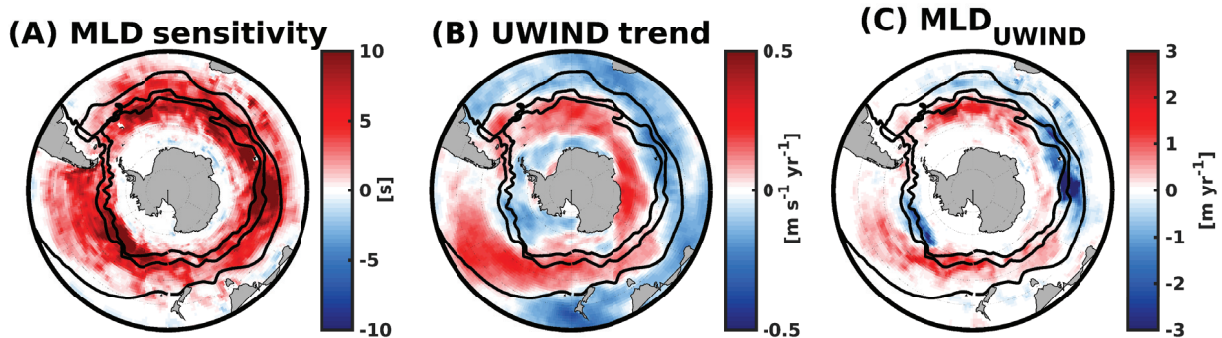
Figure 4.6: Summer MLD trend estimated from zonal wind (2002-2011). In (A), we show the modeled MLD sensitivity to zonal wind perturbation (α) ; (B) the zonal wind trends from 2002-2011 from ERA-Interim reanalysis (*Dee et al.*, 2011) and in (C) we show the corresponding summer estimated MLD tendencies obtained by multiplying the corresponding MLD sensitivity to zonal wind perturbation with the respective summer observed zonal wind trends (MLD_{UWIND}). Note the scale is different for each figure. The black contours represent the mean positions of the STF, SAF and APF (from north to south), respectively (*Orsi et al.*, 1995). Note that the observed trend (Figure 4.6B) is not masked to only show the significant parts and that this figure is the same (except for the masking) as Figure 4.2A.

4.4.2 MLD trend caused by air temperature changes

The MLD sensitivity to SAT perturbation $\theta = \frac{\partial \text{MLD}}{\partial \text{SAT}}$ is generally negative which leads to a zonally asymmetric SAT-driven MLD trend. θ is strongest ($\theta < -10$ m K^{-1}) in the ACC region of the Indian sector (Figure 4.7A). It is close to zero south of 60°S and north of 35°S. The largest decrease in SAT (< -0.1 K yr^{-1}) occurs from the AZ to the SAZ in the eastern and central Pacific sector (Figure 4.7B, note that this figure is the same as Figure 4.2B but it includes the non-significant parts). This signal extends further eastwards to Drake Passage and westwards to the Australian sector. Besides a patch in the western Indian sector, the remaining basin shows an increase in SAT. The largest increase in SAT (> 0.1 K yr^{-1}) occurs in the SAZ of the central Atlantic sector. The product of the MLD sensitivity to SAT perturbation (θ) and the actual observed SAT trend gives an estimate of the SAT-induced MLD change (Figure 4.7C). Temperature-driven ML deepening occurs in the ACC region of the Pacific and Australian sectors (red in Figure 4.7C). A temperature-driven ML shoaling occurs in the ACC region of the Atlantic and Indian sectors (blue in Figure 4.7C).
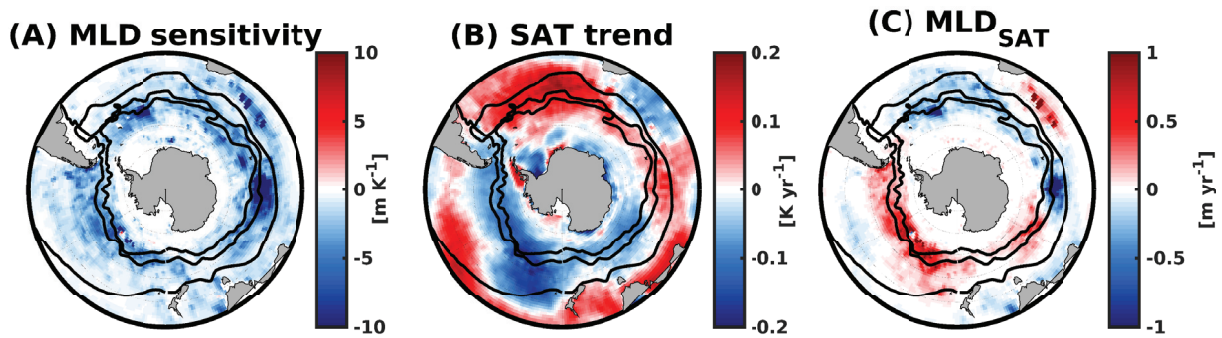
Figure 4.7: Summer MLD trend estimated from air temperature (2002-2011). In (A), we show the modeled MLD sensitivity to air temperature perturbation (θ); (B) the air temperature trends from 2002-2011 from ERA-Interim reanalysis (*Dee et al.*, 2011), and in (C) we show the corresponding summer estimated MLD tendencies obtained by multiplying the corresponding MLD sensitivity to air temperature perturbation with the respective summer observed air temperature trends (MLD$_{SAT}$). Note the scale is different for each figure. The black contours represent the mean positions of the STF, SAF and APF (from north to south), respectively (*Orsi et al.*, 1995). Note that the observed trend (Figure 4.7B) is not masked to only show the significant parts and that this figure is the same (except for the masking) as Figure 4.2B.

4.4.3 Combined effects of air temperature and wind changes on MLD

The simulated MLD trend from the sensitivity experiment captures the main characteristics of the observed MLD trend (Figure 4.8A and Figure 4.8B). The sign of the total MLD trend follows the uwind-induced MLD trend. This signal is modulated by the zonally-asymmetric SAT-induced MLD trend which is generally lower in magnitude. The uwind- and SAT-induced MLD trends reinforce each other in the Australian and western Pacific sectors, in the PFZ and SAZ of the Indian sector and in the SAZ of the Atlantic sector (Figure 4.6C and 4.7C). The uwind- and SAT-induced MLD trends oppose each other in the AZ of the Atlantic and Indian sectors in the AZ and PFZ of the eastern Pacific sector. The uwind-induced MLD trend is, however, stronger than the SAT-induced MLD trend in these regions and dominates the total response. On a Southern Ocean wide scale, uwind is the dominant factor for summer MLD variability. Temperature dominates over uwind in a few randomly distributed spots, e.g. in the coastal Weddell Sea, in the STZ of the Pacific and Indian sectors (Figure 4.9).

(A) Trend MLD obs **(B) Trend MLD estimate** **(C) Residual** [m yr^{-1}]
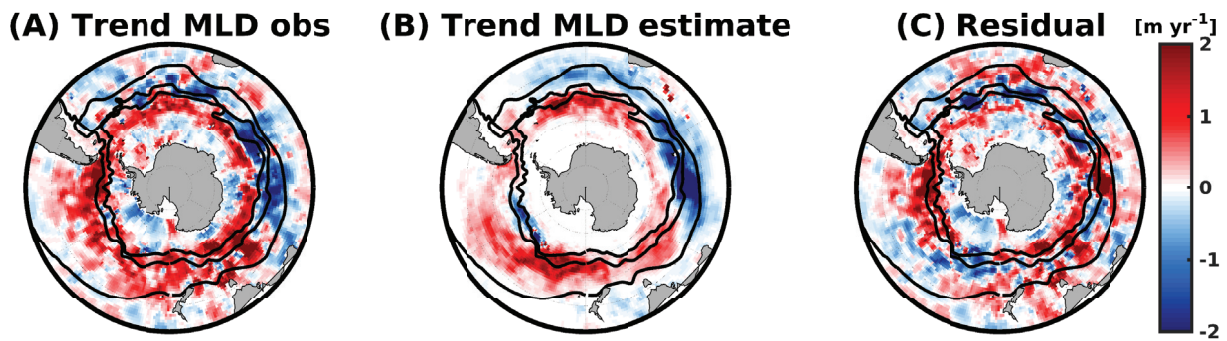
Figure 4.8: MLD trend from (A) observations, (B) from the product of model sensitivity and trends of zonal wind speed, air temperature and precipitation and (C) the residual for summer over the period of 2002-2011. The black contours represent the mean positions of the STF, SAF and APF (from north to south), respectively (*Orsi et al.*, 1995).
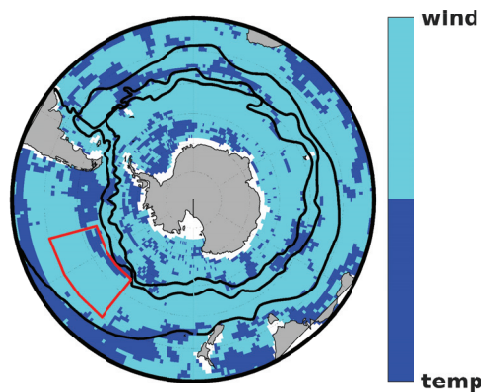
Figure 4.9: Dominance of driving forces for summer MLD. Cyan color highlights the regions where the wind effect on the MLD change dominates over temperature and the dark blue color shows the regions where the atmospheric temperature forcing on the MLD change dominates over the wind forcing. The black contours represent the mean positions of the STF, SAF and APF (from north to south), respectively (*Orsi et al.*, 1995).

4.4.4 Residual component

The residuals of the multiple linear regression (Eq. 4.2; Figure 4.8C), represents the part of observed MLD trend that is not explained by summing up the linear MLD trends from uwind and SAT. The linear model (Eq. 4.2) captures the large scale spatial features of MLD change (Figure 4.8A), nevertheless, the residuals are on the same order of magnitude as the observed MLD trend (Figure 4.8C). A large residual suggests that other drivers impact MLD that we do not consider in our model experiment, such as feedbacks to the atmospheric forcing in the ocean and non-local advection effects (*Carton et al.*, 2008). Discrepancies might also arise due to the bias existing in the modeled seasonal cycle of

the MLD (Figure 4.5A and Figure 4.5D). The modeled summer MLD is too shallow in comparison to the observation. Nonlinearities and dependencies between temperature and uwind forcing could also contribute to this residual. The combination of model results with observations gives a much smoother trend than the observations, which might also contribute to the residual.

4.5 Discussion

The strong variability in the MLD that we detect in and south of the ACC region follows a MLD deepening trend in the period 2002-2011. An exception to this is that the MLD variability observed in the PFZ and SAZ of the Indian sector follows a negative trend. The analysis of MLD variability and trend, and model sensitivity experiments agree that the change in MLD south of 65°S is insignificant. These findings are in line with a recent estimate of summer MLD variability based on daily observations between 2001 and 2011 (*Carranza and Gille*, 2015).

The MLD sensitivity to uwind perturbation in our model is stronger than the sensitivity obtained from the regression analysis (Figure 4.3A and Figure 4.6A). In contrast, the MLD sensitivity to SAT is stronger in the regression analysis than in the model (Figure 4.3B and Figure 4.7A). This discrepancy could be explained by the fact that the linear regression analysis is based on the assumption of a linear response whereas the model takes non-linearities into account. The fact that the model is capable of reproducing the MLD trend by and large suggests that the model captures the sensitivities well and that the discrepancy is caused by the errors and limitations in the assumptions associated with the multiple regressions analysis (Figure 4.8A and Figure 4.8B). This limitation of the statistical analysis might also explain the difference between MLR and model results in the Pacific box (Figure 4.4). MLR analysis suggests that the temperature effects dominate over uwind in this central Pacific box (Figure 4.4). The model sensitivity analysis suggests that indeed in the central Pacific, there are areas where temperature effect dominates over uwind effects. However, within the defined Pacific box there are more grid points where uwind effect dominates over temperature effects (Figure 4.9).

We show only zero-lag responses in our manuscript. Lags of zero to twelve months were tested in *Hauck et al.* (2013) and the authors found that the largest response of surface physical variables (current velocity, vertical advection, SST) occurred immediately (lag zero) and decreased with time. They also showed that analysing different seasons led to a much larger difference in the response variables than analysing different lag times. We also tested a lagged regression of summer MLD against zonal wind speed and SST and

found the largest response with zero lag (not shown). While longer lag times might be important for the deeper layers (*Screen et al.*, 2009; *Meredith and Hogg*, 2006), we argue that the immediate atmospheric forcing is more important than the preconditioning of the surface mixed layer in a previous season.

We found a zonal band of ML deepening which is located more to the south in the Indian and Atlantic sectors than in the Pacific. In addition we found shoaling of the MLD in the Atlantic and Indian sectors north of the areas where MLD increases. This is different from *Sallée et al.* (2010a) who found more a wave-like pattern with a zonal wave number three. *Sallée et al.* (2010a) however analysed the annual mean response, whereas we focus on the summer season because of its relevance for biology. We note that we found similar patterns to the one described in *Sallée et al.* (2010a) in autumn and winter (not shown). This suggests that the *Sallée et al.* (2010a) signal is dominated by the MLD variability in autumn and winter when the MLD and its variability are larger. Other factors that may contribute to the difference is a slightly different period of analysis and the fact that *Sallée et al.* (2010a) do a regression analysis onto SAM while we analyse the trend over time.

The MLD trend is a combination of a zonally more symmetric response to uwind and a more asymmetric response to SAT. The response of MLD to SAT is in line with warm temperature anomalies in the Atlantic and cold temperature anomalies in the Pacific (*Landschützer et al.*, 2015). The cooling in the Pacific is in line with the long-term cooling trend of SST there (*Jones et al.*, 2016b; *England et al.*, 2014). While *Landschützer et al.* (2015) hypothesize about the stabilization of the surface water in the Pacific and Atlantic sectors, our analyses indicate that there is less stratification south of the APF in the Atlantic and Indian sectors and in large parts of the Pacific sector in summer.

The pattern of the uwind-induced MLD changes in the Atlantic with a positive trend in the AZ and PFZ and negative trend in the SAZ and STZ is in line with the projected poleward shift of the wind speed and MLD maximum (*Sen Gupta et al.*, 2009) in response to a positive trend in SAM index (*Thompson et al.*, 2011; *Abram et al.*, 2014). The shoaling of the MLD in the SAZ and STZ is also supported by the increase in temperature (Figure 4.7C, *Gille*, 2008).

4.6   Conclusion

Substantial variability in summer MLD is observed in the Antarctic Circumpolar region and the Antarctic Zone. The decade 2002-2011 is a period where this MLD variability follows a MLD increasing trend in large parts of the Antarctic Zone south of the Antarctic Polar Front. There is an asymmetry between MLD changes in the Atlantic

and Indian sectors on the one hand and in the Pacific sector on the other hand. In the Pacific and Australian sectors, wind and temperature-induced MLD changes reinforce each other. In contrast, in the Antarctic Zone of the Atlantic and Indian sectors, the temperature-induced MLD trend counteracts the wind-induced MLD trend, but the wind forcing dominates. The annual mean response of the MLD to positive phases of the Southern Annular Mode (*Sallée et al.*, 2010a) differs significantly from the summer response of MLD to perturbations of atmospheric temperature and zonal wind speed. Seasonally-resolved analysis is needed to identify how environmental drivers will shape primary production in response to climate change.

References

Abram, N. J., R. Mulvaney, F. Vimeux, S. J. Phipps, J. Turner, and M. H. England (2014), Evolution of the Southern Annular Mode during the past millennium, *Nature Climate Change*, *4*(7), 564–569, doi:10.1038/NCLIMATE2235.

Akaike, H. (1973), Information theory and an extension of the maximum likelihood principle, pp. 267–281.

Atlas, R., R. N. Hoffman, J. Ardizzone, S. M. Leidner, J. C. Jusem, D. K. Smith, and D. Gombos (2011), A cross-calibrated, multiplatform ocean surface wind velocity product for meteorological and oceanographic applications, *Bulletin of the American Meteorological Society*, *92*(2), 157, doi:0.1175/2010BAMS2946.1.

Bretherton, F. P., R. E. Davis, and C. Fandry (1976), A technique for objective analysis and design of oceanographic experiments applied to MODE-73, in *Deep Sea Research and Oceanographic Abstracts*, vol. 23, pp. 559–582, Elsevier.

Cabanes, C., A. Grouazel, K. v. Schuckmann, M. Hamon, V. Turpin, C. Coatanoan, F. Paris, S. Guinehut, C. Boone, N. Ferry, et al. (2013), The CORA dataset: validation and diagnostics of in-situ ocean temperature and salinity measurements, *Ocean Science*, *9*(1), 1–18, doi: 10.5194/os-9-1-2013.

Carranza, M. M., and S. T. Gille (2015), Southern Ocean wind-driven entrainment enhances satellite chlorophyll-a through the summer, *Journal of Geophysical Research: Oceans*, *120*(1), 304–323, doi:10.1002/2014JC010203.

Carton, J. A., S. A. Grodsky, and H. Liu (2008), Variability of the oceanic mixed layer, 1960–2004, *Journal of Climate*, *21*(5), 1029–1047, doi:10.1175/2007JCLI1798.1.

de Boyer Montégut, C., G. Madec, A. S. Fischer, A. Lazar, and D. Iudicone (2004), Mixed layer depth over the global ocean: An examination of profile data and a profile-based climatology, *Journal of Geophysical Research: Oceans*, *109*(C12003), doi:10.1029/2004JC002378.

Dee, D., S. Uppala, A. Simmons, P. Berrisford, P. Poli, S. Kobayashi, U. Andrae, M. Balmaseda, G. Balsamo, P. Bauer, et al. (2011), The ERA-Interim reanalysis: Configuration and performance of the data assimilation system, *Quarterly Journal of the Royal Meteorological Society*, *137*(656), 553–597, doi:10.1002/qj.828.

Denman, K. (1973), A time-dependent model of the upper ocean, *Journal of Physical Oceanography*, *3*(2), 173–184, doi:10.1175/1520-0485(1973)003$< 0173 : ATDMOT > 2.0.CO; 2$.

DeVries, T., M. Holzer, and F. Primeau (2017), Recent increase in oceanic carbon uptake driven by weaker upper-ocean overturning, *Nature*, *542*(7640), 215–218, doi:10.1038/nature21068.

England, M. H., S. McGregor, P. Spence, G. A. Meehl, A. Timmermann, W. Cai, A. S. Gupta, M. J. McPhaden, A. Purich, and A. Santoso (2014), Recent intensification of wind-driven circulation in the Pacific and the ongoing warming hiatus, *Nature Climate Change*, *4*(3), 222–227, doi:10.1038/NCLIMATE2106.

Fauchereau, N., A. Tagliabue, L. Bopp, and P. Monteiro (2011), The response of phytoplankton biomass to transient mixing events in the Southern Ocean, *Geophysical Research Letters*, *38*(17), doi:10.1029/2011GL048498.

Fogt, R. L., J. Perlwitz, A. J. Monaghan, D. H. Bromwich, J. M. Jones, and G. J. Marshall (2009), Historical SAM variability. Part II: Twentieth-century variability and trends from reconstructions, observations, and the IPCC AR4 models, *Journal of Climate*, *22*(20), 5346–5365, doi:10.1175/2009JCLI2786.1.

Frölicher, T. L., J. L. Sarmiento, D. J. Paynter, J. P. Dunne, J. P. Krasting, and M. Winton (2015), Dominance of the Southern Ocean in anthropogenic carbon and heat uptake in CMIP5 models, *Journal of Climate*, *28*(2), 862–886, doi:10.1175/JCLI-D-14-00117.1.

Gent, P. R., and J. C. McWilliams (1990), Isopycnal mixing in ocean circulation models, *Journal of Physical Oceanography*, *20*(1), 150–155, doi:10.1175/1520-0485(1990)020$< 0150 : IMIOCM > 2.0.CO; 2$.

Gilbert, R. O. (1987), *Statistical methods for environmental pollution monitoring*, John Wiley & Sons.

Gille, S. T. (2008), Decadal-scale temperature trends in the Southern Hemisphere ocean, *Journal of Climate*, *21*(18), 4749–4765, doi:10.1175/2008JCLI2131.1.

Gruber, N., M. Gloor, S. E. Mikaloff Fletcher, S. C. Doney, S. Dutkiewicz, M. J. Follows, M. Gerber, A. R. Jacobson, F. Joos, K. Lindsay, et al. (2009), Oceanic sources, sinks, and transport of atmospheric CO_2, *Global Biogeochemical Cycles*, *23*(GB1005), 1924–9224, doi:10.1029/2008GB003349.

Hauck, J., C. Völker, T. Wang, M. Hoppema, M. Losch, and D. A. Wolf-Gladrow (2013), Seasonally different carbon flux changes in the Southern Ocean in response to the southern annular mode, *Global Biogeochemical Cycles*, *27*(4), 1236–1245, doi:10.1002/2013GB004600.

Hauck, J., C. Völker, D. Wolf-Gladrow, C. Laufkötter, M. Vogt, O. Aumont, L. Bopp, E. T. Buitenhuis, S. C. Doney, J. Dunne, et al. (2015), On the Southern Ocean CO_2 uptake and the role of the biological carbon pump in the 21st century, *Global Biogeochemical Cycles*, *29*(9), 1451–1470, doi:10.1002/2015GB005140.

Hauck, J., P. Köhler, D. Wolf-Gladrow, and C. Völker (2016), Iron fertilisation and century-scale effects of open ocean dissolution of olivine in a simulated CO_2 removal experiment, *Environmental Research Letters*, *11*(2), 024,007, doi:10.1088/1748-9326/11/2/024007.

Huang, C. J., F. Qiao, Q. Shu, and Z. Song (2012), Evaluating austral summer mixed-layer response to surface wave–induced mixing in the Southern Ocean, *Journal of Geophysical Research: Oceans*, *117*(C11), doi:10.1029/2012JC007892.

Jones, J. M., S. T. Gille, H. Goosse, N. J. Abram, P. O. Canziani, D. J. Charman, K. R. Clem, X. Crosta, C. De Lavergne, I. Eisenman, et al. (2016), Assessing recent trends in high-latitude Southern Hemisphere surface climate, *Nature Climate Change*, *6*(10), 917–926, doi:10.1038/NCLIMATE3103.

Kahru, M., R. Kudela, M. Manzano-Sarabia, and B. G. Mitchell (2009), Trends in primary production in the California Current detected with satellite data, *Journal of Geophysical Research: Oceans*, *114*(C2), doi:10.1029/2008JC004979.

Kalnay, E., M. Kanamitsu, R. Kistler, W. Collins, D. Deaven, L. Gandin, M. Iredell, S. Saha, G. White, J. Woollen, et al. (1996), The NCEP/NCAR 40-year reanalysis project, *American Meteorological Society*, *77*(3), 437–471, doi:10.1175/1520-0477(1996)077$< 0437 : TNYRP >$ $2.0.CO; 2$.

Khatiwala, S., F. Primeau, and T. Hall (2009), Reconstruction of the history of anthropogenic CO_2 concentrations in the ocean, *Nature*, *462*(7271), 346–349, doi:10.1038/nature08526.

Landschützer, P., N. Gruber, F. A. Haumann, C. Rödenbeck, D. C. Bakker, S. Van Heuven, M. Hoppema, N. Metzl, C. Sweeney, T. Takahashi, et al. (2015), The reinvigoration of the Southern Ocean carbon sink, *Science*, *349*(6253), 1221–1224, doi:10.1126/science.aab2620.

Large, W., and S. Yeager (2009), The global climatology of an interannually varying air–sea flux data set, *Climate Dynamics*, *33*(2-3), 341–364, doi:10.1007/s00382-008-0441-3.

Large, W. G., and S. G. Yeager (2004), *Diurnal to decadal global forcing for ocean and sea-ice models: the data sets and flux climatologies*, National Center for Atmospheric Research Boulder.

Large, W. G., J. C. McWilliams, and S. C. Doney (1994), Oceanic vertical mixing: A review and a model with a nonlocal boundary layer parameterization, *Reviews of Geophysics*, *32*(4), 363–403, doi:10.1029/94RG01872.

Le Quéré, C., R. M. Andrew, J. G. Canadell, S. Sitch, J. I. Korsbakken, G. P. Peters, A. C. Manning, T. A. Boden, P. P. Tans, R. A. Houghton, et al. (2016), Global carbon budget 2016, *Earth System Science Data*, *8*(2), 605, doi:10.5194/essd-8-605-2016.

Lee, S., and S. B. Feldstein (2013), Detecting ozone-and greenhouse gas–driven wind trends with observational data, *Science*, *339*(6119), 563–567, doi:10.1126/science.1225154.

Lenton, A., B. Tilbrook, R. Law, D. C. Bakker, S. C. Doney, N. Gruber, M. Hoppema, M. Ishii, N. S. Lovenduski, R. J. Matear, et al. (2013), Sea-air CO_2 fluxes in the Southern Ocean for the period 1990-2009, *Biogeosciences Discussions*, *10*, 285–333, doi:10.5194/bgd-10-285-2013.

Llort, J., M. Lévy, J.-B. Sallée, and A. Tagliabue (2015), Onset, intensification, and decline of phytoplankton blooms in the Southern Ocean, *ICES Journal of Marine Science*, *72*(6), 1971–1984, doi:10.1093/icesjms/fsv053.

Losch, M., D. Menemenlis, J.-M. Campin, P. Heimbach, and C. Hill (2010), On the formulation of sea-ice models. Part 1: Effects of different solver implementations and parameterizations, *Ocean Modelling*, *33*(1), 129–144, doi:10.1016/j.ocemod.2009.12.008.

Lumpkin, R., and K. Speer (2007), Global ocean meridional overturning, *Journal of Physical Oceanography*, *37*(10), 2550–2562, doi:10.1175/JPO3130.1.

Marshall, G. J. (2003), Trends in the Southern Annular Mode from observations and reanalyses, *Journal of Climate*, *16*(24), 4134–4143, doi:10.1175/1520-0442(2003)016$< 4134 : TITSAM >$2.0.$CO; 2$.

Marshall, J., and K. Speer (2012), Closure of the meridional overturning circulation through Southern Ocean upwelling, *Nature Geoscience*, *5*(3), 171–180, doi:10.1038/NGEO1391.

Marshall, J., A. Adcroft, C. Hill, L. Perelman, and C. Heisey (1997), A finite-volume, incompressible Navier Stokes model for studies of the ocean on parallel computers, *Journal of Geophysical Research: Oceans*, *102*(C3), 5753–5766, doi:10.1029/96JC02775.

Meredith, M. P., and A. M. Hogg (2006), Circumpolar response of Southern Ocean eddy activity to a change in the Southern Annular Mode, *Geophysical Research Letters*, *33*(16), doi:10.1029/2006GL026499.

Orsi, A. H., T. Whitworth, and W. D. Nowlin (1995), On the meridional extent and fronts of the Antarctic Circumpolar Current, *Deep Sea Research Part I: Oceanographic Research Papers*, *42*(5), 641–673, doi:10.1016/0967-0637(95)00021-W.

Sabine, C. L., R. A. Feely, N. Gruber, R. M. Key, K. Lee, J. L. Bullister, R. Wanninkhof, C. Wong, D. W. Wallace, B. Tilbrook, et al. (2004), The oceanic sink for anthropogenic CO_2, *Science*, *305*(5682), 367–371, doi:10.1126/science.1097403.

Sallée, J., K. Speer, and S. Rintoul (2010), Zonally asymmetric response of the Southern Ocean mixed-layer depth to the Southern Annular Mode, *Nature Geoscience*, *3*(4), 273–279, doi:10.1038/ngeo812.

Sallée, J.-B., R. J. Matear, S. R. Rintoul, and A. Lenton (2012), Localized subduction of anthropogenic carbon dioxide in the Southern Hemisphere oceans, *Nature Geoscience*, *5*(8), 579–584, doi:10.1038/ngeo1523.

Sallée, J.-B., E. Shuckburgh, N. Bruneau, A. Meijers, T. Bracegirdle, and Z. Wang (2013), Assessment of Southern Ocean mixed-layer depths in CMIP5 models: Historical bias and forcing response, *Journal of Geophysical Research: Oceans*, *118*(4), 1845–1862, doi:10.1002/jgrc.20157.

Screen, J. A., N. P. Gillett, D. P. Stevens, G. J. Marshall, and H. K. Roscoe (2009), The role of eddies in the Southern Ocean temperature response to the Southern Annular Mode, *Journal of Climate*, *22*(3), 806–818, doi:10.1175/2008JCLI2416.1.

Sen Gupta, A., A. Santoso, A. S. Taschetto, C. C. Ummenhofer, J. Trevena, and M. H. England (2009), Projected changes to the Southern Hemisphere ocean and sea ice in the IPCC AR4 climate models, *Journal of Climate*, *22*(11), 3047–3078, doi:10.1175/2008JCLI2827.1.

Swart, N., and J. Fyfe (2012), Observed and simulated changes in the Southern Hemisphere surface westerly wind-stress, *Geophysical Research Letters*, *39*(16), doi:10.1029/2012GL052810.

Talley, L. D. (2013), Closure of the global overturning circulation through the Indian, Pacific, and Southern Oceans: Schematics and transports, *Oceanography*, *26*(1), 80–97, doi:10.5670/oceanog.2013.07.

Thompson, D. W., S. Solomon, P. J. Kushner, M. H. England, K. M. Grise, and D. J. Karoly (2011), Signatures of the Antarctic ozone hole in Southern Hemisphere surface climate change, *Nature Geoscience*, *4*(11), 741–749, doi:10.1038/NGEO1296.

Venables, H., and C. M. Moore (2010), Phytoplankton and light limitation in the Southern Ocean: Learning from high-nutrient, high-chlorophyll areas, *Journal of Geophysical Research: Oceans*, *115*(C2), doi:10.1029/2009JC005361.

Verdy, A., S. Dutkiewicz, M. Follows, J. Marshall, and A. Czaja (2007), Carbon dioxide and oxygen fluxes in the Southern Ocean: Mechanisms of interannual variability, *Global Biogeochemical Cycles*, *21*(2), doi:10.1029/2006GB002916.

Supplementary Information

Supporting Information for "Drivers of interannual variability of summer Mixed Layer Depth in the Southern Ocean between 2002-2011"

E. Panassa[1], C. Völker[1], D. Wolf-Gladrow[1] and J.Hauck[1]

[1] Alfred Wegener Institute Helmholtz Centre for Polar and Marine Research, Am Handelshafen 12, 27570 Bremerhaven, Germany

Introduction
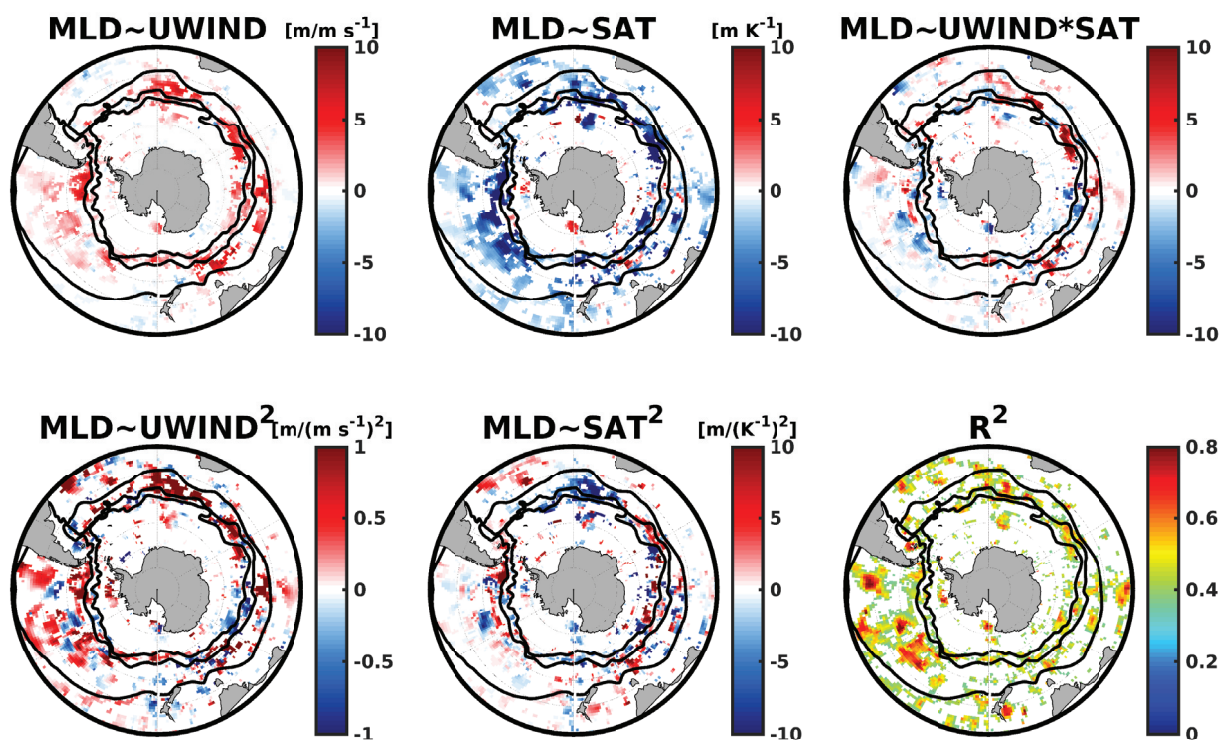
Figure 4.10: Shown are the regression coefficients of the multi linear regression with interaction of observed MLD anomalies during summer months against anomalies during summer months of zonal wind speed (uwind), near-surface air temperature (SAT), uwind*SAT, uwind^2 and SAT^2, respectively. We show also the explained variance in MLD variability (r-square). Only significant regression coefficients at the 95% confidence level are shown. The black contours represent the mean positions of the STF, SAF and APF (from north to south), respectively [Orsi et al., 1995].

The supplementary material contains:

1) the plot of the regression coefficients from the multi-linear of observed MLD anomalies during summer months against anomalies during summer months of of zonal wind

speed (uwind), near-surface air temperature (SAT) and interaction terms, uwind^2, SAT^2 and uwind*SAT (Figure 4.10). We also show in Figure 4.10, the explained variance in MLD variability from uwind, SAT variability and interaction effects (R^2). Only significant regression coefficients at the 95% confidence level are shown. The equation of the regression model is given by the Eq. 4.3:

$$\text{MLD} = \beta_0 + \beta_1 * \text{uwind} + \beta_2 * \text{SAT} + \beta_3 * (\text{uwind} * \text{SAT}) + \beta_4 * \text{uwind}^2 + \beta_5 * \text{SAT}^2 + \xi, \quad (4.3)$$

where β_0 represents the model intercept, β_1 to β_5 represent the regression coefficient slopes of MLD onto uwind, SAT, uwind*SAT, uwind^2 and SAT^2, respectively. uwind*SAT is the interaction term, uwind^2 and SAT^2 represent the quadratic terms and ξ represents the residual. Also we show in Figure 4.11 a pixel map where the AIC difference between the regression model taking into account interaction and quadratic terms and the regression model with no interaction is larger than 2.
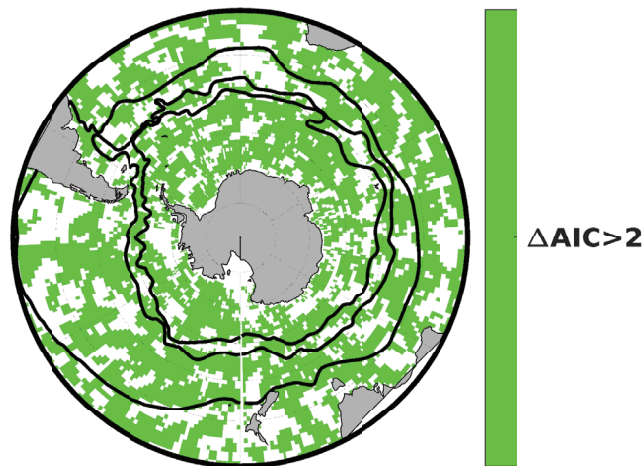
Figure 4.11: Pixel map showing the region where $\text{AIC}_{\text{interation}} - \text{AIC}_{\text{no\_interaction}} > 2$. The black contours represent the mean positions of the STF, SAF and APF (from north to south), respectively [Orsi et al., 1995].

2) the linear trend map of the sea surface temperature over the period of 2002-2011 (Figure 4.12).
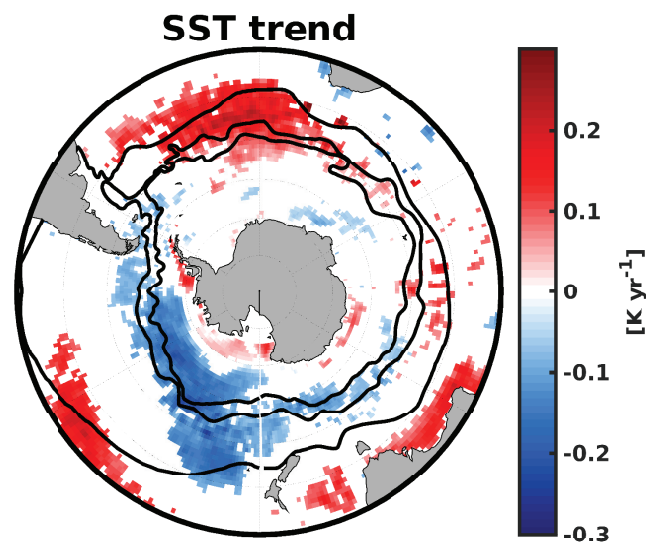
Figure 4.12: Summer trend for the period 2002-2011 of the sea surface temperature (SST) from the ERA-Interim reanalysis [Dee et al., 2011]. Only significant trends at the 95% confidence level are shown. The black contours represent the mean positions of the STF, SAF and APF (from north to south), respectively [Orsi et al., 1995].

Chapter 5

Interannual variability of carbon and nutrient subduction in the Southern Ocean

Interannual variability of carbon and nutrient subduction in the Southern Ocean

E. Panassa[1], C. Völker[1], D. Wolf-Gladrow[1] and J.Hauck[1]

[1] Alfred Wegener Institute Helmholtz Centre for Polar and Marine Research, Am Handelshafen 12, 27570 Bremerhaven, Germany

Abstract   Southern Ocean carbon and nutrient subduction and obduction rates in the period of 1958 to 2016 across the base of the winter mixed layer were assessed using an ocean biogeochemical model and were analysed with regard to the positive trend in the Southern Annular Mode (SAM) index. The time-averaged and spatially-integrated gross subduction rates of carbon and nutrients south of 30°S were estimated to be 167.7 PgC yr^{-1} (dissoloved inorganic carbon, DIC), 113.9 Tmol N yr^{-1} (dissolved inorganic nitrogen, DIN), 159.8 Tmol Si yr^{-1} (dissolved silicic acid) and 2.0 Gmol Fe yr^{-1} (dissolved Fe). This is balanced with gross obduction rates of -151.0 PgC yr^{-1}, -135.5 Tmol N yr^{-1}, -203.7 Tmol Si yr^{-1} and -2.3 Gmol Fe yr^{-1}. The variations in SAM lead to large-scale anomalies in carbon and nutrient subduction/obduction rates that are zonally symmetric. More obduction occurs south of the Antarctic Polar Front (APF), whereas more subduction occurs north of the APF in response to SAM. Positive subduction anomalies are strongest where the meridional gradient of mixed layer depth is strongest. We have also investigated the net carbon and nutrient subduction/obduction rates in the density classes of the strongest subduction/obduction. The carbon and nutrient subduction rates varied more on the interannual time scale before 1990 and followed a decadal trend since then. The net carbon and nitrate subduction rates in the highest subduction density class have increased by 3.5 TgC yr^{-1} (19%) for DIC and 2.1 Gmol yr^{-1} (25%) for nitrate over the past 69 years. In contrast, the net subduction rates of iron and silicic acid have decreased by 12.2 Kmol yr^{-1} (9%) and 0.8 Gmol yr^{-1} (18%), respectively. The negative trends are explained by the fact that silicic acid and iron can both be limiting factors for phytoplankton growth south of 30°S. In the upwelling region, the net obduction rates of carbon and nutrients increased over time. This suggests that the positive SAM over the least decades has increased upper ocean circulation in the SO. These changes in the carbon

and nutrient subduction rates might impact the carbon cycle and primary productivity in low latitudes.

5.1 Introduction

Observational based studies have revealed that about 80% of carbon-rich deep waters of the global ocean resurface in the Southern Ocean through wind-induced upwelling (*Lumpkin and Speer*, 2007; *Marshall and Speer*, 2012; *Talley*, 2013). The main physical mechanism responsible for the vertical transfer of sea water from the main thermocline to the mixed layer is known as obduction (upwelling). This upwelling supplies nutrients to the euphotic zone and closes the loop of the biological carbon pump. The return paths from the Southern Ocean to lower latitudes are via subduction of mode and intermediate waters and through export of bottom water (*Talley*, 2013). Subduction is the physical process through which a significant amount of surface water with its constituents such as carbon, nutrients, and also heat are transported back into the deep ocean across the base of the winter mixed layer (ML), where it can be stored for a longer time (*Sallée et al.*, 2010b). Both subduction and obduction play an important role for ocean circulation, redistribution of heat, carbon and nutrients and hence for the climate system.

The formation and subduction of Subantarctic Mode Water (SAMW) and Antarctic Intermediate Water (AAIW) north of the Antarctic Polar Front (APF) and Subantarctic Front (SAF; *Talley*, 2013) is the dominant pathway through which carbon and nutrient-rich waters exit the Southern Ocean and flow into the thermocline towards the low latitudes where they fuel 10 to 75% of the local primary productivity (*Sarmiento et al.*, 2004; *Palter et al.*, 2010; *Holzer and Primeau*, 2013).

The formation and transformation of SAMW and AAIW depend on surface heat and freshwater fluxes, i.e. air-sea buoyancy fluxes, on mixing processes and are modulated by wind-induced Ekman downwelling or upwelling (*Cerovečki et al.*, 2013; *Kwon*, 2013).

The maximum transfer of SAMW and AAIW from the mixed layer into the permanent thermocline occurs during late winter and early spring when the mixed layer shoals rapidly due to surface warming (*Marshall et al.*, 1993; *Kwon*, 2013). At a large scale, subduction rates of SAMW and AAIW are largely dominated by the lateral induction (horizontal advection) with an additional contribution by eddies (*Marshall et al.*, 1993; *Downes et al.*, 2009; 2010; *Sallée et al.*, 2010b; *Langlais et al.*, 2017).

Formation of SAMW and AAIW also play an important role in the uptake and sequestration of anthropogenic carbon (C_{ant}) in the SO (*Sabine et al.*, 2004; *Khatiwala et al.*, 2009; *Sallée et al.*, 2012; *Iudicone et al.*, 2016). 56% of the total anthropogenic carbon inventory in the Southern Ocean is stored in mode and intermediate waters (*Langlais et al.*, 2017). Horizontal advection is the dominant physical process (lateral induction) for the transfer of C_{ant} across the base of the winter ML (*Langlais et al.*, 2017). The intensity of the horizontal transport (subduction) of C_{ant} into the ocean interior is affected by the

variation in the depth of the winter mixed layer (*Sallée et al.*, 2012).

A recent high-resolution model study suggests that mesoscale stationary Rossby waves (SRWs) play an important role for the lateral induction term. These SRWs are generated by the interaction between the Antarctic Circumpolar Current and the bottom topography (*Langlais et al.*, 2017). Other processes, such as northward Ekman transport and mixing induced by eddies and the variation in mixed layer depth play also a significant role in the transport of C_{ant} (*Sallée et al.*, 2012; *Bopp et al.*, 2015). Diffusion contributes to the transport of anthropogenic carbon across the seasonally varying mixed layer depth (*Bopp et al.*, 2015), but part of that might be mixed back up into the mixed layer when the mixed layer deepens again in winter.

There is regional variability in the formation of mode and intermediate water masses that is shaped by the regional structure of the mean geostrophic circulation (*Jones et al.*, 2016a). Although it is usually thought that there is not much formation of SAMW in the Atlantic sector of the SO as only lighter mode waters are formed here (*Cerovečki et al.*, 2013), a relatively high amount of C_{ant} are found at the base of the winter mixed layer in the Atlantic sector (*Sallée et al.*, 2012). Also, a high interannual variability occurs in the annual mean subduction rate of SAMW which is partly controlled by the interannual variability in the winter mixed layer depth (*Kwon*, 2013).

Model studies indicate a recent increase in SAMW and AAIW subduction rates driven by the stronger westerly winds and hence wind-induced northward Ekman transport and pumping (*Downes et al.*, 2011; *Hauck et al.*, 2013). Recently, *Downes et al.* (2017) using a high-resolution model study suggested that the increase in westerlies leads to increased subduction rates, while the poleward shift of the westerlies leads to a decrease in subduction rate. The total effect (increase plus poleward shift of westerlies) leads to a reduction in subduction but *Downes et al.* (2017) state that the overall change of the subduction rate is small. These idealized experiments (*Downes et al.*, 2017) contradict earlier studies by the same author (*Downes et al.*, 2011) and this inconsistency remains unresolved. Similarly, stronger winds lead to stronger upper ocean overturning and the poleward shift to a weakening thereof (*Hogg et al.*, 2017). While stronger upwelling is linked to stronger subduction, the ocean response depends on the pattern of wind changes (strengthening and shift, *Hogg et al.*, 2017).

Future model simulations project a strengthening of westerly winds (*Thompson et al.*, 2011; *Swart and Fyfe*, 2012; *Meijers*, 2014; *Zheng et al.*, 2013), but at the same time a decrease in subduction rates by the end of the twentieth century mostly driven by the increase in surface warming and freshening (*Downes et al.*, 2009; 2010). This suggests that the future response of the subduction rate in the SAMW and AAIW density classes will depend on the balance between the global warming signal (increased stratification,

Gille, 2008) and the wind signal (decreased stratification, *Thompson et al.*, 2011) that occur simultaneously in the SO (*Hauck et al.*, 2015). A decrease in the SAMW and AAIW subduction rates would likely in the future decrease the anthropogenic carbon sequestration and reduce the transport of nutrients along with carbon to the low latitudes.

Recent studies based on observations show that significant regional changes have occurred in the water-mass properties of SAMW and AAIW and other water masses in the Southern Ocean. These changes were explained by an increase of the upwelling rate and might consequently lead to more subduction (*Hoppema et al.*, 2015; *Pardo et al.*, 2017; *Tanhua et al.*, 2017; *Panassa et al.*, 2018). What is still lacking in the literature is an overview on the sensitivity of the carbon and nutrient subduction/obduction rates to changes in the Southern Ocean wind forcing.

The main objective of this study is to investigate the interannual variability of carbon and nutrient subduction rates. While *Hauck et al.* (2013) analysed vertical fluxes across 100 m depth, we analyse the subduction rate (vertical and horizontal) across the base of the winter mixed layer with respect to interannual variability and to the response to the positive trend of the SAM index.

We present our model set-up and the steps we followed for the calculation of the subduction rate in section 5.2. In section 5.3.1, we present the temporal mean state of the volume, carbon and nutrient fluxes across the base of the winter mixed layer. In section 5.3.2, the interannual variability of volume, mixed layer, carbon and nutrient flux in response to the southern annular mode (SAM) for different seasons at zero-lag is investigated. Finally, we investigate interannual variability of carbon and nutrient subduction rates in the density classes with highest subduction and obduction, respectively, in section 5.3.2.

5.2 Data and methods

5.2.1 Model configuration

We use the Massachusetts Institute of Technology general circulation model (MITgcm, *Marshall et al.*, 1997) that is coupled to the Regulated Ecosystem Model with two phytoplankton classes (REcoM-2). REcoM-2 includes two phytoplankton functional types (diatoms and nanophytoplankton), one zooplankton and one detritus compartment, as well as inorganic and organic forms of the main nutrients (nitrate, silicic acid, and iron). For a detailed description of REcoM-2 and equations the reader is refered to *Hauck et al.* (2013). The resolution of the MITgcm set-up varies from 0.38° to 2° in latitude, with higher resolution in the Southern Ocean and around the equator and 2° in longitude, with

30 non-uniform vertical layers. The model uses the Gent-McWilliams eddy parameterization (*Gent and McWilliams*, 1990), sea-ice dynamics and thermodynamics (*Losch et al.*, 2010) and the nonlocal K-Profile parameterization (KPP) boundary layer mixing scheme (*Large et al.*, 1994) for the vertical mixing within the mixed layer.

5.2.2   Model simulation

A century-scale simulation was performed with the MITgcm model. The model was forced by historic atmospheric CO_2 concentrations (*Le Quéré et al.*, 2016) and interannual varying atmospheric NCEP/NCAR forcing fields (*Kalnay et al.*, 1996). The model was spun-up from 1900 to 1947 and we ran the model for 69 years, from 1948 to 2016. This model simulation was submitted to the Global Carbon Budget 2017 (*Le Quéré et al.*, 2017) and it only differs from the model set-up in *Hauck et al.* (2016) by changing two parameter settings, i.e nanophytoplankton chlorophyll degradation rate was set to 0.1 d^{-1} and Fe-solubility was set to 1%. From the model simulation, we saved the time-series of the following 3D fields, namely current velocities, temperature, salinity, horizontal and vertical advection of dissolved inorganic carbon, alkalinity and nutrients.

5.2.3   Calculation of subduction

To infer the annual subduction rates of water volume, carbon and nutrients into the permanent thermocline, three steps were followed:

1 - The mixed layer depth (MLD) was defined by the 0.03 kg m^{-3} density criterion (*de Boyer Montégut et al.*, 2004) with a reference depth of 10 m from the ocean surface using the potential density fields calculated from the model temperature and salinity fields. From the monthly MLD fields, we calculated the maximum MLD at every grid point.

2 - We interpolated velocities, and advection fields of carbon and nutrients in the vertical to the maximum MLD.

3 - We evaluated the water volume, nutrient and carbon annual subduction rates across the maximum MLD based on the kinematic approach of *Marshall et al.* (1993) given by the Eq. 5.1:

$$S_{ann} = -W_H - U_H \cdot \nabla H \qquad (5.1)$$

where S$_{ann}$ represents the subduction rate (given in units of m yr^{-1}), W$_H$ is the vertical component, U$_H \cdot \nabla$ H is the lateral induction term (horizontal component) and H is the maximum mixed layer depth (from the full time-series).

4 - We investigated the influence of the Southern Annular Mode (SAM) on the interannual variability of the Southern Ocean (south of 30°S) volume, nutrient and carbon subduction rates.

5 - We integrated the time series of the total fluxes (volume, carbon, and nutrients) in the density classes where net subduction (obduction) peak (Figure 5.1, black bars, subduction: $1026.5 < \sigma_\theta < 1026.7$ kg m^{-3}, obduction: $1027.3 \leq \sigma_\theta < 1027.5$ kg m^{-3}), respectively, and quantify their interannual variability between 1958 and 2016 (see section 5.3.2). The distribution of the subduction rate in density coordinates shown in Figure 5.1 is obtained from the annual mean subduction rates averaged from 1958 to 2016.
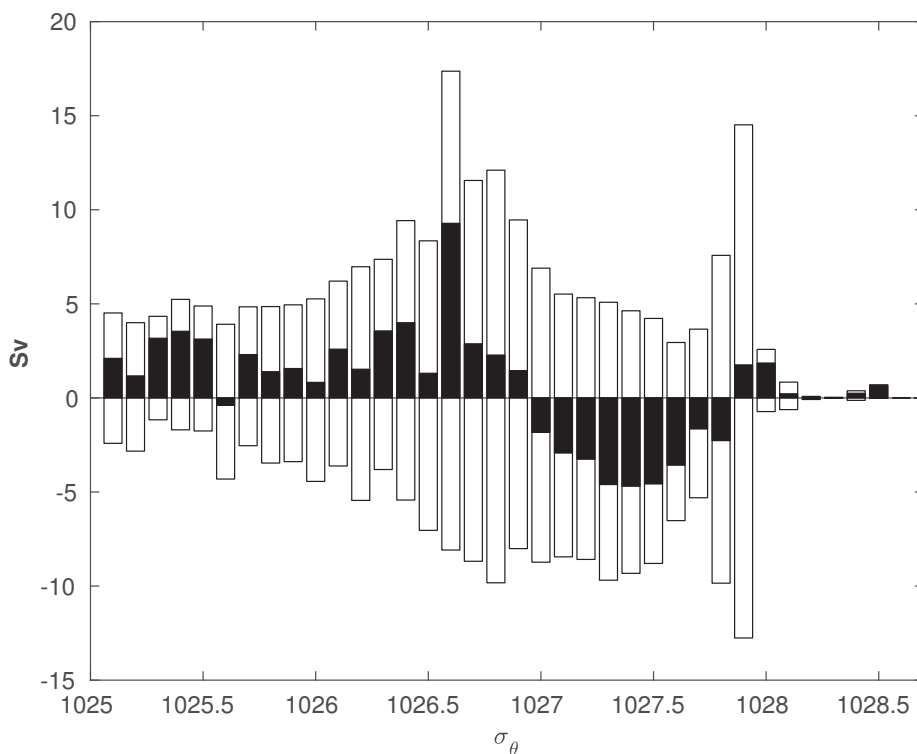
Figure 5.1: Annual mean spatially-integrated subduction/obduction rates of water volume as a function of the potential density (σ_θ, kg m^{-3}) in the Southern Ocean. White bars show the gross subduction (positive) and obduction (negative) rates and black bars show the net subduction rate.

5.2.4   Statistical analyses

To investigate the influence of the Southern Annular Mode (SAM) on the interannual variability of the Southern Ocean volume, carbon and nutrient subduction rates, we conducted a lagged regression analysis (lag of 0 to 12 months) between the monthly anomalies of the variables of study onto the monthly SAM index as in *Hauck et al.* (2013). The anomalies of the state variables of study, namely annual subduction rates of volume, car-

bon and nutrients were obtained by removing the mean seasonal cycle at each grid point of the monthly time series.

The SAM index used in this study (*Marshall*, 2003) was calculated from the station-based index of the Southern Annular Mode based on the difference of sea level pressure fields measured between 40°S and 65°S. The monthly SAM index time series started in January 1957 and is ongoing (*Marshall*, 2003). We used the time series from January 1958 to December 2016 (Figure 5.2). This dataset is available at https://climatedataguide.ucar .edu/climate-data/marshall-southern-annular-mode-sam-index-station-based. Since the 1990s SAM has shifted more often to its high-index polarity (Figure 5.2).

We refer to the summer response, when the anomaly time series of the months December, January and February were used for regression onto the SAM index, winter response when the anomaly time series of the months June, July and August were used for regression onto the SAM index and annual mean response when the whole time series was used.
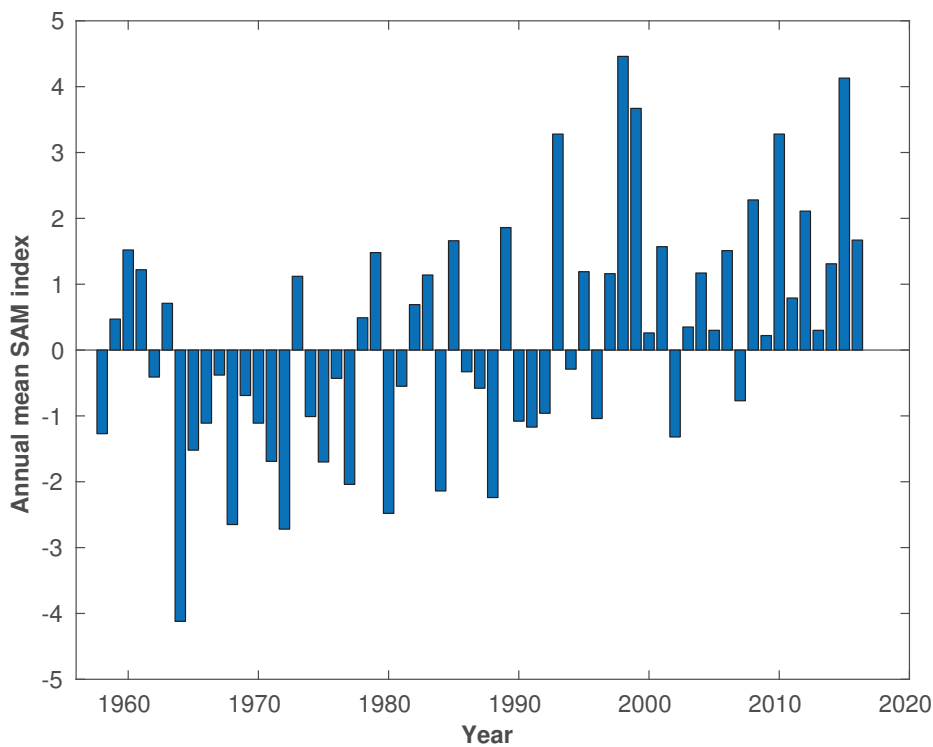
Figure 5.2: Annual mean time series of the Southern Annular Mode index from 1958 to 2016 (*Marshall*, 2003).

5.3   Results and discussion

5.3.1   Annual mean subduction of volume, carbon and nutrients
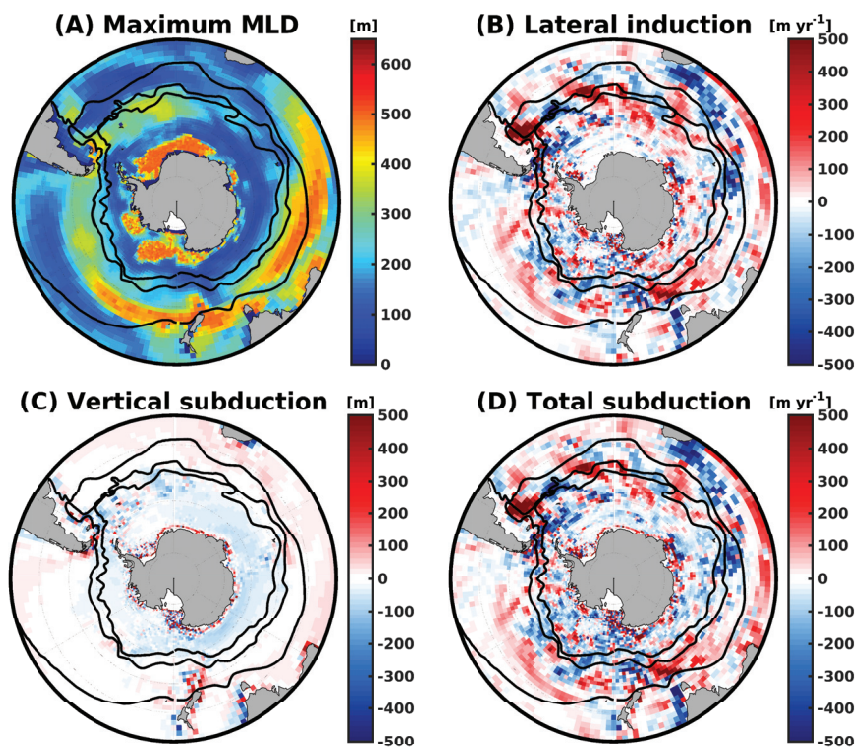
Figure 5.3: A) The maximum mixed-layer depth (MLD) calculated using the 0.03 kg m^{-3} density criterion (*de Boyer Montégut et al.*, 2004), (B) lateral induction, (C) vertical subduction and (D) the total annual mean subduction rate of water (m yr^{-1}) averaged over 1958 to 2016. We use the convention that water fluxes directed to the mixed layer are counted negatively (obduction). The black contours represent the mean positions of the STF, SAF and APF (from north to south), respectively (*Orsi et al.*, 1995).

Volume transport

The total annual physical transfer (subduction and obduction) of water volume (S_{ann}) is dominated by the lateral induction term (Figure 5.3B and D). The lateral induction term reaches transports of up to 200 m yr^{-1} in specific spots along the Antarctic Circumpolar Current (ACC; Figure 5.3B). In contrast, the vertical transport makes only a small contribution to the total subduction/obduction rates (Figure 5.3C). The net S_{ann} is characterized by large-scale obduction south of 50°S. Specifically, obduction occurs along the ACC and along the path of the Agulhas current in the Indian sector that flows southward and mixes into the ACC (Figure 5.3D). Along the ACC, regions of subduction and

obduction alternate. Wherever obduction occurs, the mixed layer deepens in the direction of the mean flow (Figure 5.3A, B and D). Similarly, subduction occurs where the mixed layer shoals in the direction of the flow. Along the coast of the Antarctic continent subduction of water masses occurs driven by the vertical subduction (Figure 5.3C and D).

The main patterns of S_{ann}, such as obduction in the Agulhas path and subduction south of Australia are consistent with *Sallée et al.* (2010b), but our estimate is more heteregenous. The magnitude of S_{ann} is consistent with the model-based estimate of *Downes et al.* (2017), but higher than the observation-based estimate of *Sallée et al.* (2010b). The integrated gross subduction rate over the SO (south of 30°S) averaged over 1958 to 2016 is estimated to be 200.6 Sv (1 Sv$= 10^6$ m^3 s^{-1}), while the integrated gross obduction rate averaged over the same period is estimated to be -177.5 Sv. The integrated gross subduction rate from our model simulation over the period of 1959 to 2006 (199.6 Sv) is consistent but slightly higher than the estimated 177.4 Sv of *Liu and Huang* (2012).

Carbon and nutrient transport

The patterns of the subduction rates of dissolved inorganic carbon, total alkalinity (Alk) and nutrients across the base of the winter mixed layer are similar to the subduction and obduction patterns of the volume transport (Figure 5.4). Strongest subduction of DIC and Alk (up to 500 mol m^{-2} yr^{-1}) occurs in the subtropical zone (north of the Subtropical Front) and in specific spots along the ACC. The spatial pattern of DIC subduction shows the same alternation of subduction and obduction as in *Lévy et al.* (2013).

The gross DIC and alkalinity subduction rates integrated over the SO (south of 30°S) averaged over 1958 to 2016 are 167.7 PgC yr^{-1} for DIC and 15.1 Pmol yr^{-1} for alkalinity. The integrated gross obduction rates averaged over the same period are -151.0 PgC yr^{-1} for DIC and -13.4 Pmol yr^{-1} for alkalinity.

The gross subduction and obduction rates are naturally larger in our model simulation forced with increasing concentration of atmospheric CO_2 than in the preindustrial simulation of *Lévy et al.* (2013). While in the preindustrial simulation net obduction of 14.3 PgC yr^{-1} occurred in the Southern Ocean south of 44°S (*Lévy et al.*, 2013), our historical simulation results in net subduction of 16.7 PgC yr^{-1} south of 30°S in accord with the change of the SO from a CO_2 source to a CO_2 sink (*Mikaloff Fletcher et al.*, 2007; *Gruber et al.*, 2009).
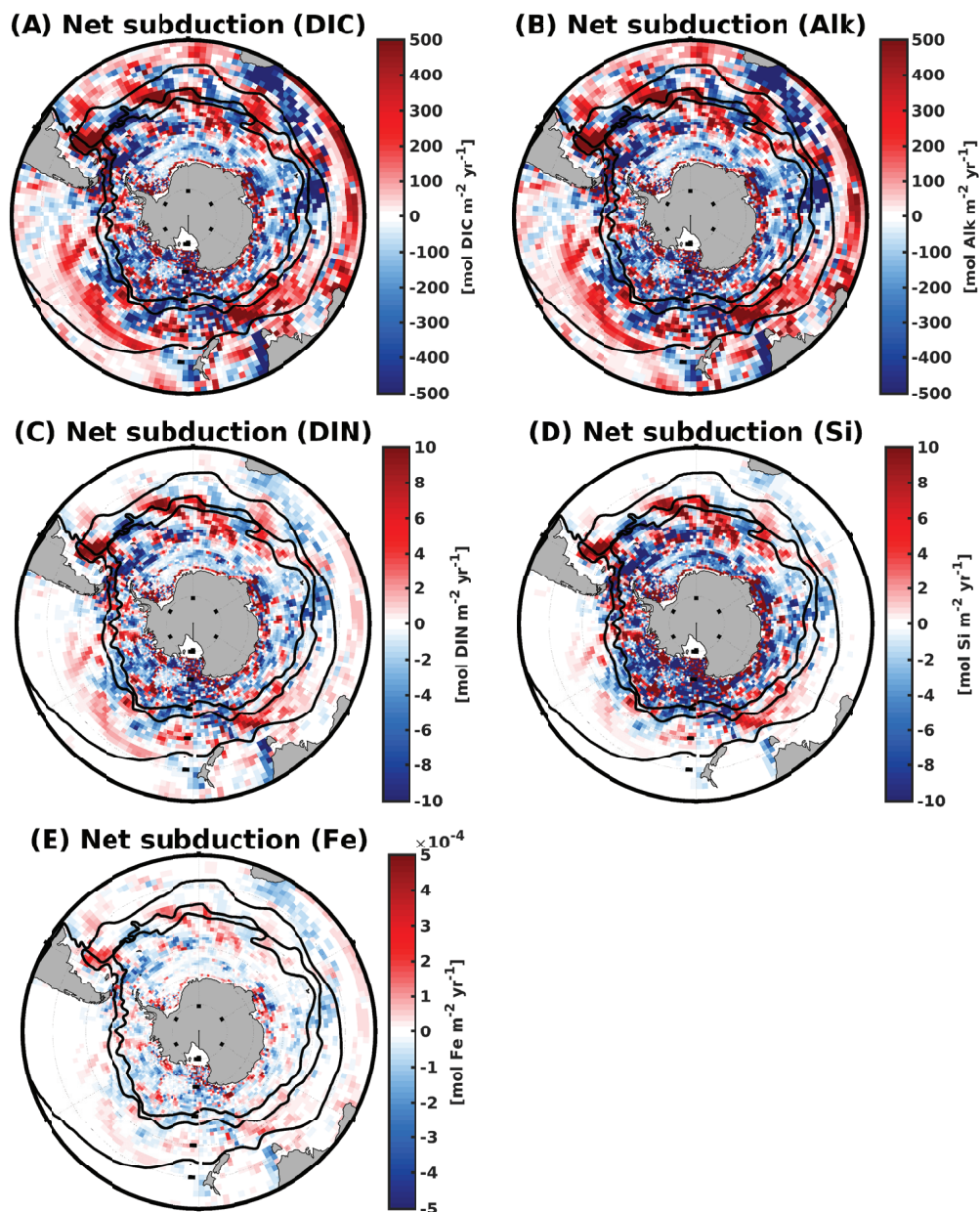
Figure 5.4: The annual mean net subduction rates of dissolved inorganic carbon (DIC), Alkalinity (Alk), dissolved nitrate (DIN), dissolved silicic acid (Si) and dissolved iron (Fe) averaged from 1958 to 2016. We use the convention that upward carbon, alkalinity, iron, dissolved nitrate and silicic acid fluxes are counted negatively (i.e., obduction). The black contours represent the mean positions of the STF, SAF and APF (from north to south), respectively (*Orsi et al.*, 1995).

The patterns of DIN, Si and Fe subduction are characterized by weak subduction and obduction rates north of the Subtropical Front whereas strong obduction rates occur south of Subantarctic Front and alternate with the subduction rates of the same magnitude (Figure 5.4C to E). Particularly Si transport is low north of STF where silicic acid is the

limiting nutrient for phytoplankton production in our model (*Hauck et al.*, 2013) and in the real world (*Laubscher et al.*, 1993; *Martínez-García et al.*, 2014; *Conkright et al.*, 1994).

The gross DIN, Si and Fe subduction rates integrated over the SO (south of 30°S) averaged over 1958 to 2016 are 113.9 Tmol yr^{-1} for DIN, 159.8 Tmol yr^{-1} for Si and 2.0 Gmol yr^{-1} for Fe. The integrated gross obduction rates averaged over the same period are -135.5 Tmol yr^{-1} for DIN, -203.7 Tmol yr^{-1} for Si and -2.3 Gmol yr^{-1} for Fe, so that there is a net flux of nutrients into the mixed layer and smaller subduction after the utilization of nutrients by primary producers.

5.3.2   Response to SAM

In the following section we only show the response of the mixed layer depth and S$_{ann}$ at zero lag because this is when the response is strongest, as was also shown by *Hauck et al.* (2013).

Figure 5.5: Regression coefficients of state variables regressed onto the SAM index. All numbers are per one unit increase in SAM index. Shown are regressions onto the SAM index of mixed-layer depth (MLD, 0 lag, first row) and water mass subduction rate (S$_{ann}$, 0 lag, second row), for the annual mean (left column), winter (middle column) and summer (right column) seasons. White areas indicate no trend or no significant correlation at the 95% confidence level. The black contours represent the mean positions of the STF, SAF and APF (from north to south), respectively (*Orsi et al.*, 1995).

Response of Southern Ocean mixed layer depth and volume transport to SAM

The patterns of variability of the mixed layer depth (MLD) and subduction rate (S_{ann}), as depicted by a regression onto the Southern Annular Mode (SAM) index are shown in Figure 5.5. The annual mean response of the MLD and S_{ann} to the SAM is more zonally symmetric for the S_{ann} than for the MLD and is dominated by the summer response. During summer the mixed layer deepens in the ACC region in the Pacific sector and south of the SAF in the Atlantic and Indian sectors with increasing SAM index (Panassa et al., in review at JGR-Oceans; Figure 5.5C). Shoaling occurs north of the SAF in the Atlantic and Indian sectors. The response of the S_{ann} to SAM shows stronger obduction south of the APF and stronger subduction north of the APF. During the winter season the signals are less clear. The strongest anomalies of the S_{ann} occur where the meridional gradient of MLD is strongest.

In this study we do not smooth the MLD and SAM time series before performing the regression analysis. This leads to slightly different response patterns as compared to *Hauck et al.* (2013) who applied an 8 months moving average to filter out variability on shorter than interannual time scales. The annual mean spatial patterns and amplitude of the response of MLD to SAM are consistent with the estimate of *Kwon* (2013).

Response of Southern Ocean carbon and nutrient subduction rates to SAM

The spatial patterns of the regression coefficients of carbon and nutrient subduction rates as regressed onto the SAM index (Figures 5.6 and 5.7) are similar to the spatial patterns of the response of the subduction rate in terms of volume transport (Figure 5.5). We see a homogeneous increase in subduction rate of DIC and Alk north of the APF. In contrast, there is an increase in the obduction rate of DIC and Alk south of the APF. The change in DIC and Alk subduction rates in response to the SAM reaches up to 50 mol m^{-2} yr^{-1} with strongest subduction rate anomalies located in the Atlantic and Indian ACC region in summer.

The response of the nutrient subduction rates to a positive SAM event is more restricted to the southern part of the Southern Ocean (Figure 5.7). An increase in obduction rate of nutrient occurs south of the APF and the northern extent to which positive subduction anomalies occur increases from silicic acid (south of 50°S) to DIN (south of 45°S) to Fe with no clear boundary in the Atlantic and Indian sectors. The response of the Fe north of STF might be related to continental dust input.
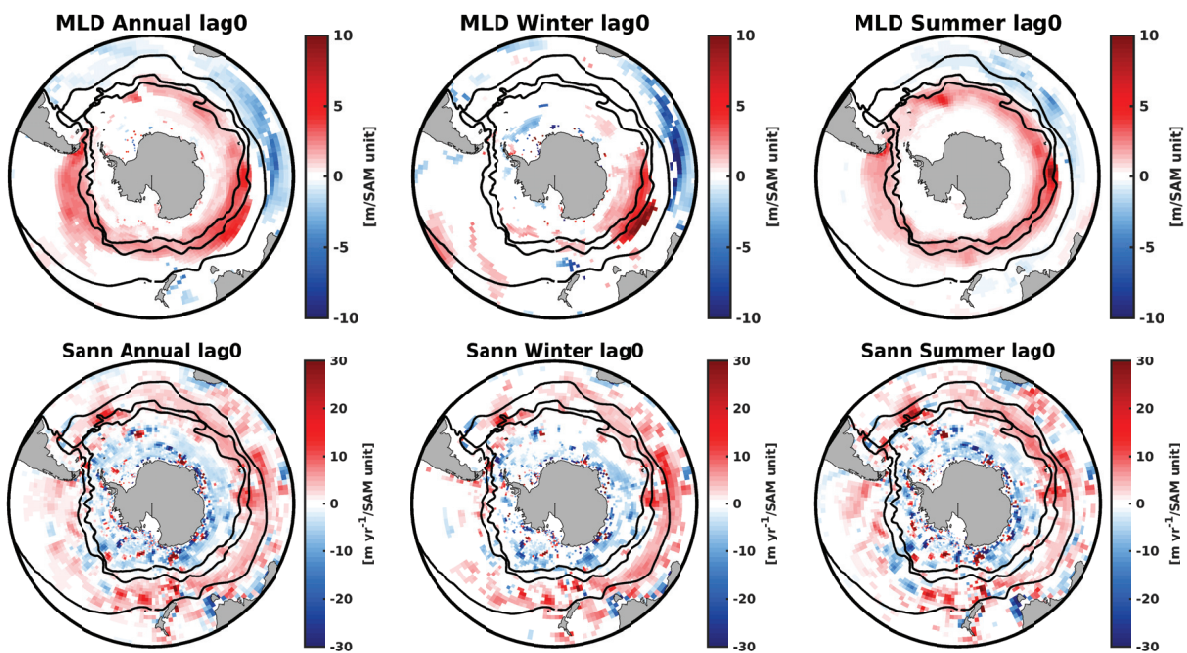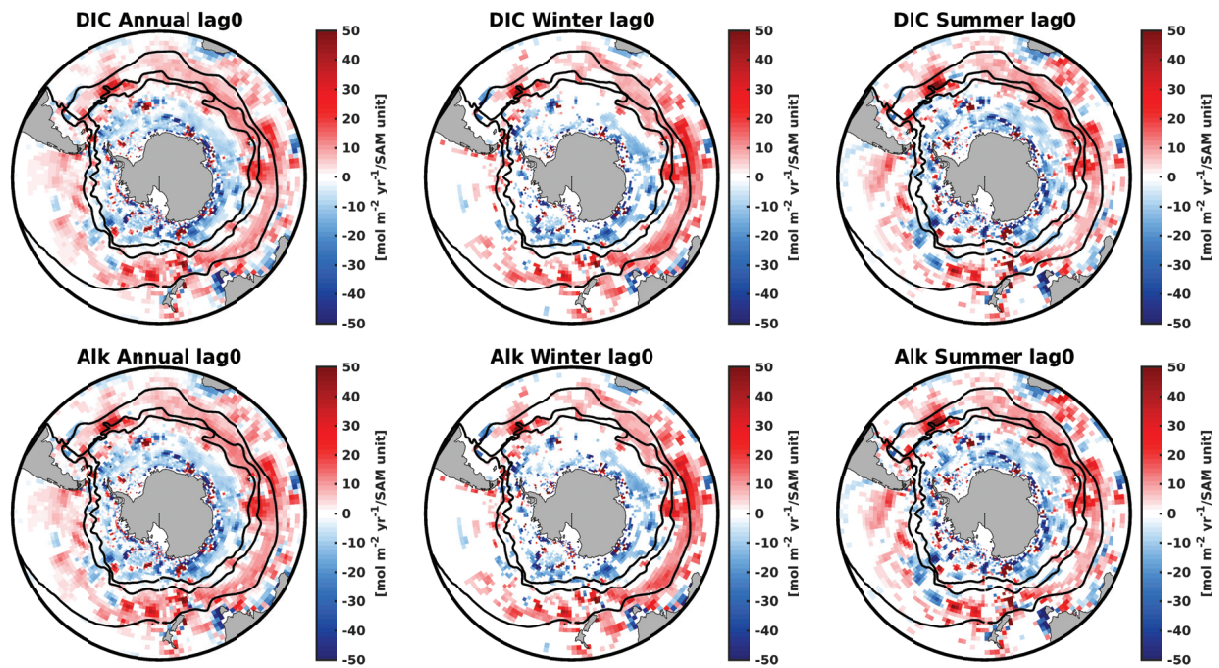
Figure 5.6: Regression coefficients of state variables regressed onto the SAM index. All numbers are per one unit increase in SAM index. Shown are regressions onto the SAM index of subduction rate of dissolved inorganic carbon (DIC, 0 lag, first row) and alkalinity (Alk, 0 lag, second row), in annual mean (left column), winter (middle column) and summer (right column) seasons. White areas indicate no trend or no significant correlation at the 95% confidence level. The black contours represent the mean positions of the STF, SAF and APF (from north to south), respectively (*Orsi et al.*, 1995).
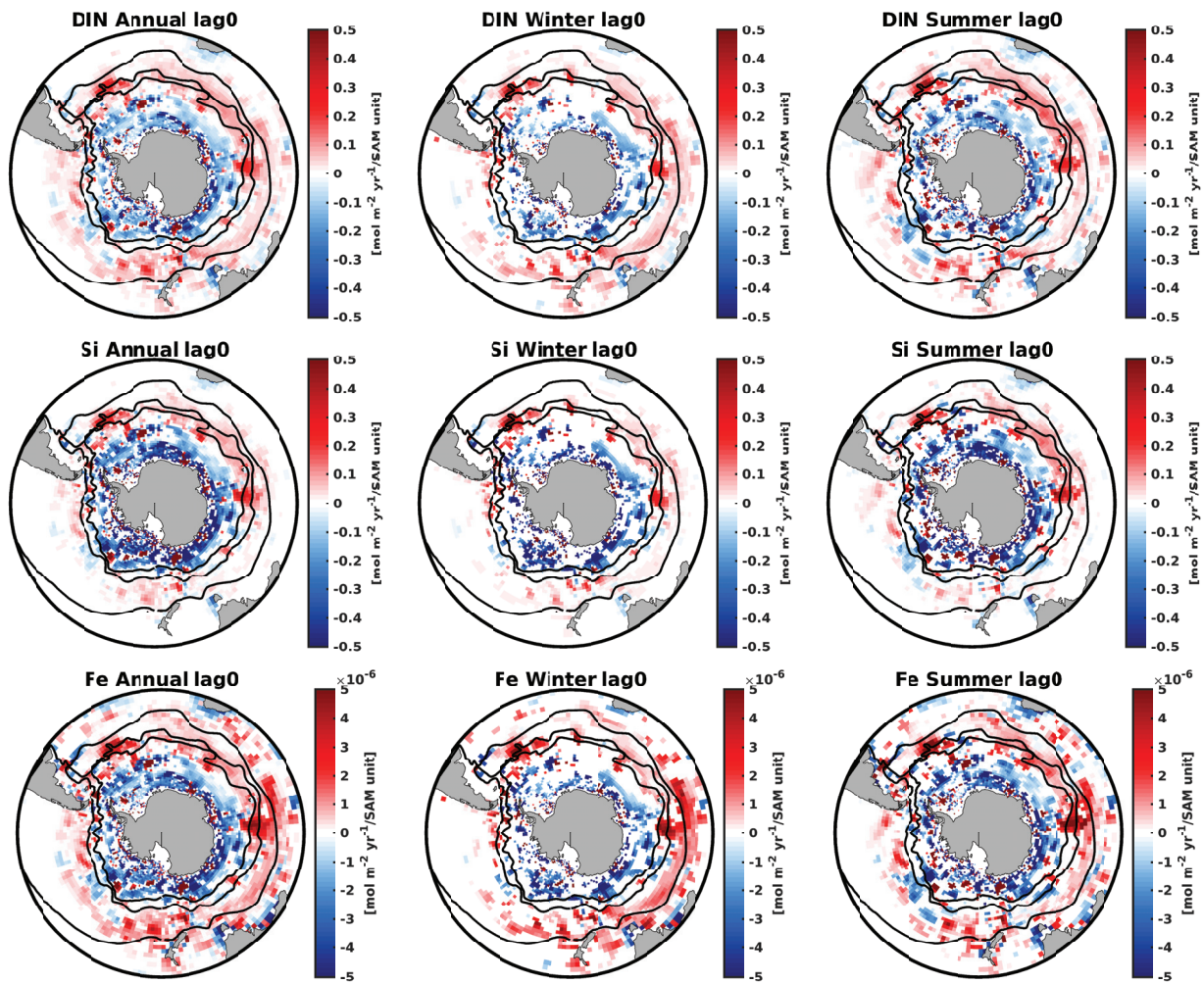
Figure 5.7: Regression coefficients of state variables regressed onto the SAM index. All numbers are per one unit increase in SAM index. Shown are regressions onto the SAM index of subduction rate of dissolved inorganic nitrate (DIN, 0 lag, first row), dissolved silicic acid (Si, 0 lag, second row) and dissolved iron (Fe, 0 lag, third row), in annual mean (left column), winter (middle column) and summer (right column) seasons. White areas indicate no trend or no significant correlation at the 95% confidence level. The black contours represent the mean positions of the STF, SAF and APF (from north to south), respectively (*Orsi et al.*, 1995).

Temporal variability of subduction

In the following section, we analyse the time-series of gross subduction, gross obduction and net subduction rates. All these rates are reported as positive quantities. Larger positive numbers indicate stronger transports. For this, the gross obduction rate was multiplied with -1, which is different to the convention used in previous section where subduction is shown positively and obduction negatively in the maps.

Density class of highest subduction $(1026.5 < \sigma_\theta < 1026.7)$ The time series of the annual mean gross subduction, gross obduction and net subduction rates of DIC, DIN, Si, and Fe between 1958 to 2016 are shown in Figures 5.8 to 5.11, respectively.

The annual gross DIC subduction rate between 1958 and 1989 varied by a maximum of 4.2 PgC yr^{-1} around the mean of 41.5 PgC yr^{-1}. Since the early 1990s the gross DIC subduction rate increased by 0.3 (PgC yr^{-1}) yr^{-1} (Figure 5.8A). The annual gross DIC obduction rate between 1958 and 1989 varied by a maximum of 3.8 PgC yr^{-1} around the mean of 24.1 PgC yr^{-1}. Since the early 1990s the gross DIC obduction rate increased by 0.2 (PgC yr^{-1}) yr^{-1} (Figure 5.8B). The gross subduction increased stronger than the obduction rate and therefore the net DIC subduction rate increased by 0.04 (PgC yr^{-1}) yr^{-1} from 1958 to 2016 and 0.1 (PgC yr^{-1}) yr^{-1} between 1990 and 2016 (Figure 5.8C).

Similarly the gross DIN subduction rate between 1958 and 1989 varied by a maximum of 2.5 Gmol yr^{-1} around the mean of 24.0 Gmol yr^{-1}, and from 1990 to 2016, the gross DIN subduction rate decreased by 0.2 (Gmol yr^{-1}) yr^{-1} (Figure 5.9A). The gross DIN obduction rate between 1958 and 1989 varied by a maximum of 2.4 Gmol yr^{-1} around the mean of 15.9 Gmol yr^{-1}, and from 1990 to 2016, the gross DIN obduction rate increased by 0.1 (Gmol yr^{-1}) yr^{-1} (Figure 5.9B). The net DIN subduction rate increased by 0.04 (Gmol yr^{-1}) yr^{-1} from 1958 to 2016 and by 0.08 (Gmol yr^{-1}) yr^{-1} between 1990 and 2016 (Figure 5.9C).

In contrast to DIC and DIN, the subduction and obduction rates of Si and Fe decreased until the early 1990s and showed little change since then. Applying a linear fit to the net Si and Fe subduction rates, results in a negative trend of -0.029 (Gmol Si yr^{-1}) yr^{-1} and -0.5 (Kmol Fe yr^{-1}) yr^{-1} (Figures 5.10C and 5.11C).

We also investigated the influence of SAM on the annul mean net subduction rates of DIC, DIN, Si, and Fe. The net subduction rates increased by 0.8 TgC yr^{-1} (DIC), 0.5 Gmol DIN yr^{-1}, 0.05 Gmol Si yr^{-1} and 4.4 Kmol Fe yr^{-1} for a one unit increase in the SAM index.

Figure 5.8: Time series of the total annual subduction rate of DIC from 1958 to 2016 in the density classes with strongest subduction ($1026.5 < \sigma_\theta < 1026.7$ kg m^{-3}).

Figure 5.9: Time series of the total annual subduction rate of DIN from 1958 to 2016 in the density classes with strongest subduction ($1026.5 < \sigma_\theta < 1026.7$ kg m^{-3}).

Figure 5.10: Time series of the total annual subduction rate of Si from 1958 to 2016 in the density classes with strongest subduction ($1026.5 < \sigma_\theta < 1026.7$ kg m^{-3}).

Figure 5.11: Time series of the total annual subduction rate of Fe from 1958 to 2016 in the density classes with strongest subduction ($1026.5 \leq \sigma_\theta < 1026.7$ kg m^{-3}).

Density class of highest obduction ($1027.3 \leq \sigma_\theta < 1027.5$) The time series of the annual mean gross subduction, gross obduction and net subduction rates of DIC, DIN, Si, and Fe between 1958 to 2016 are shown in Figures 5.12 to 5.15, respectively.

The annual gross DIC subduction rate between 1958 and 1989 varied by a maximum of 3.0 TgC yr^{-1} around the mean of 14.0 TgC yr^{-1}. Since the early 1990s the annual gross

DIC subduction rate decreased by -0.03 (PgC yr^{-1}) yr^{-1} (Figure 5.12A). The annual gross DIC obduction rate between 1958 and 1980 varied by a maximum of 2.4 TgC yr^{-1} around the mean of 24.0 TgC yr^{-1}. Since the early 1990s the gross DIC obduction rate increased by 0.02 (PgC yr^{-1}) yr^{-1} (Figure 5.12B). While the gross obduction rate increased, the gross subduction rate decreased and therefore the net DIC obduction rate increased by 0.04 (PgC yr^{-1}) yr^{-1} from 1958 to 2016 and 0.05 (PgC yr^{-1}) yr^{-1} between 1990 and 2016 (Figure 5.12C).

Similarly, the annual gross DIN subduction rate between 1958 and 1989 varied by a maximum of 3.4 Gmol yr^{-1} around the mean of 18.2 Gmol yr^{-1}, and from 1990 to 2016, the annual gross DIN subduction rate decreased by -0.01 (Gmol yr^{-1}) yr^{-1} (Figure 5.13A). The annual gross DIN obduction rate between 1958 and 1989 varied by a maximum of 3.0 Gmol yr^{-1} around the mean of 30.0 Gmol yr^{-1}, and from 1990 to 2016, the annual gross DIN obduction rate increased by 0.05 (Gmol yr^{-1}) yr^{-1} (Figure 5.13B). The net DIN obduction rate increased by 0.05 (Gmol yr^{-1}) yr^{-1} from 1958 to 2016 and 0.06 (Gmol yr^{-1}) yr^{-1} between 1990 and 2016 (Figure 5.13C).

The annual gross Si and Fe subduction rates between 1958 and 1989 varied by a maximum of 5.6 Gmol Si yr^{-1} (56.3 Kmol Fe yr^{-1}) around the mean of 31.9 Gmol Si yr^{-1} (307.3 Kmol Fe yr^{-1}), and from 1990 to 2016 the gross Si and Fe subduction rate increased by 0.01 (Gmol Si yr^{-1}) yr^{-1} [0.2 (Kmol Fe yr^{-1}) yr^{-1}], respectively (Figure 5.14A and Figure 5.15A). The annual gross Si and Fe obduction rates between 1958 and 1989 varied by a maximum of 5.0 Gmol yr^{-1} (62.0 Kmol Fe yr^{-1}) around the mean of 52.3 Gmol yr^{-1} (485.5 Kmol Fe yr^{-1}), and from 1990 to 2016 the gross Si and Fe obduction rates increased by 0.1 (Gmol yr^{-1}) yr^{-1} [1.1 (Kmol Fe yr^{-1}) yr^{-1}] (Figure 5.13B and Figure 5.15B). The net Si and Fe obduction rates increased by 0.06 (Gmol Si yr^{-1}) yr^{-1} [0.9 (Kmol Fe yr^{-1}) yr^{-1}] from 1958 to 2016 and 0.09 (Gmol Si yr^{-1}) yr^{-1} [0.9 (Kmol Fe yr^{-1}) yr^{-1}] between 1990 and 2016 (Figure 5.14C and Figure 5.15C).

We also investigated the influence of SAM on the annul mean net obduction rates of DIC, DIN, Si, and Fe. The net obduction rates increased by 0.5 TgC yr^{-1} (DIC), 0.6 Gmol DIN yr^{-1}, 0.9 Gmol Si yr^{-1} and 9.3 Kmol Fe yr^{-1} for a one unit increase in the SAM index.

In the positive phase of the SAM there is more obduction of nutrients and carbon into the mixed layer. Parts of the nutrients are utilized in the surface mixed layer and as a result the positive anomalies of subduction are smaller than the positive anomalies of obduction. This is particularly true for silicic acid. In contrast, while the positive trend in SAM brings more carbon into the surface mixed layer, an even larger amount of carbon is subducted.
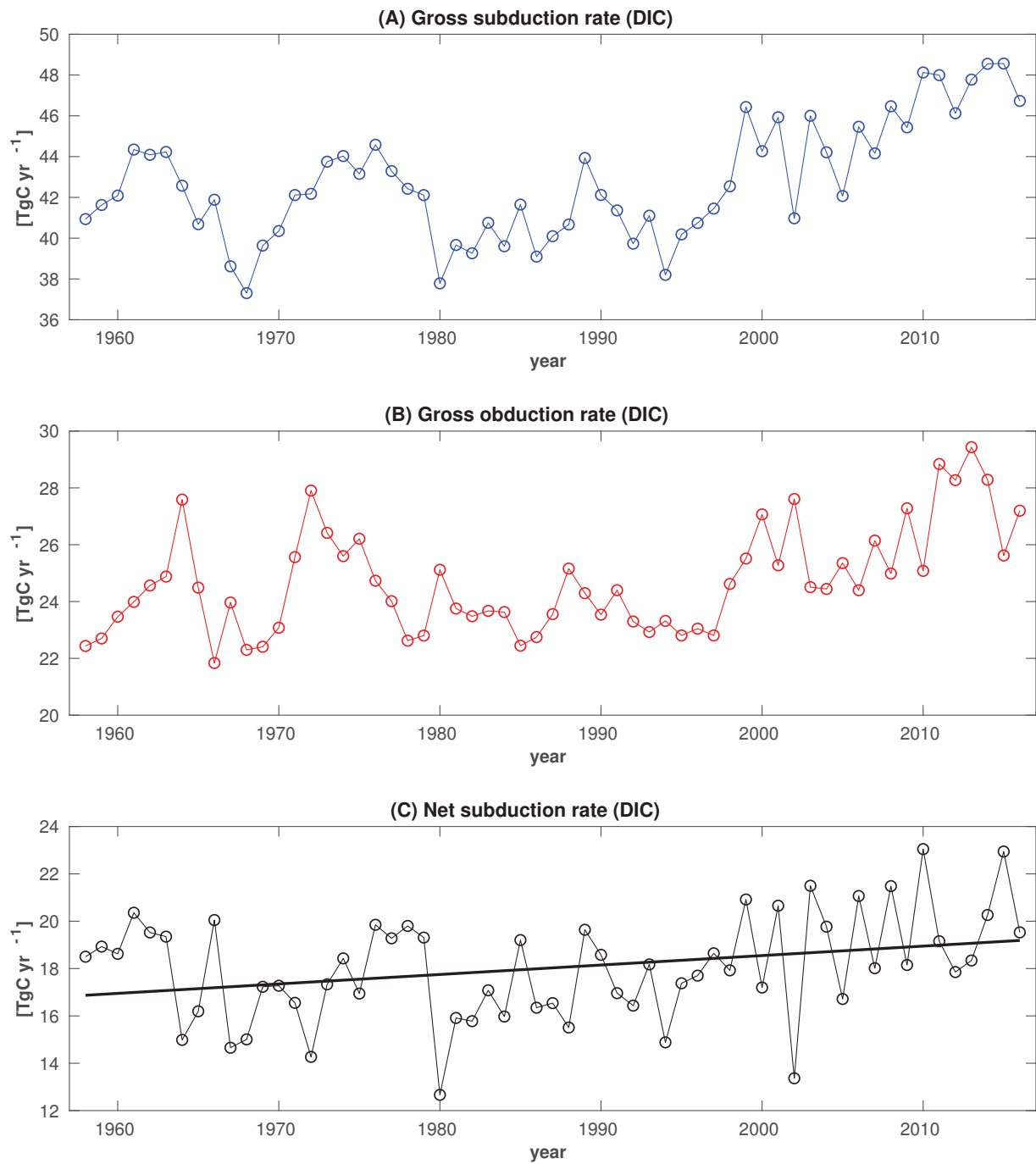
Figure 5.12: Time series of the total annual obduction rate of DIC from 1958 to 2016 in the density classes with strongest obduction ($1027.3 \leq \sigma_\theta < 1027.5$ kg m^{-3}).
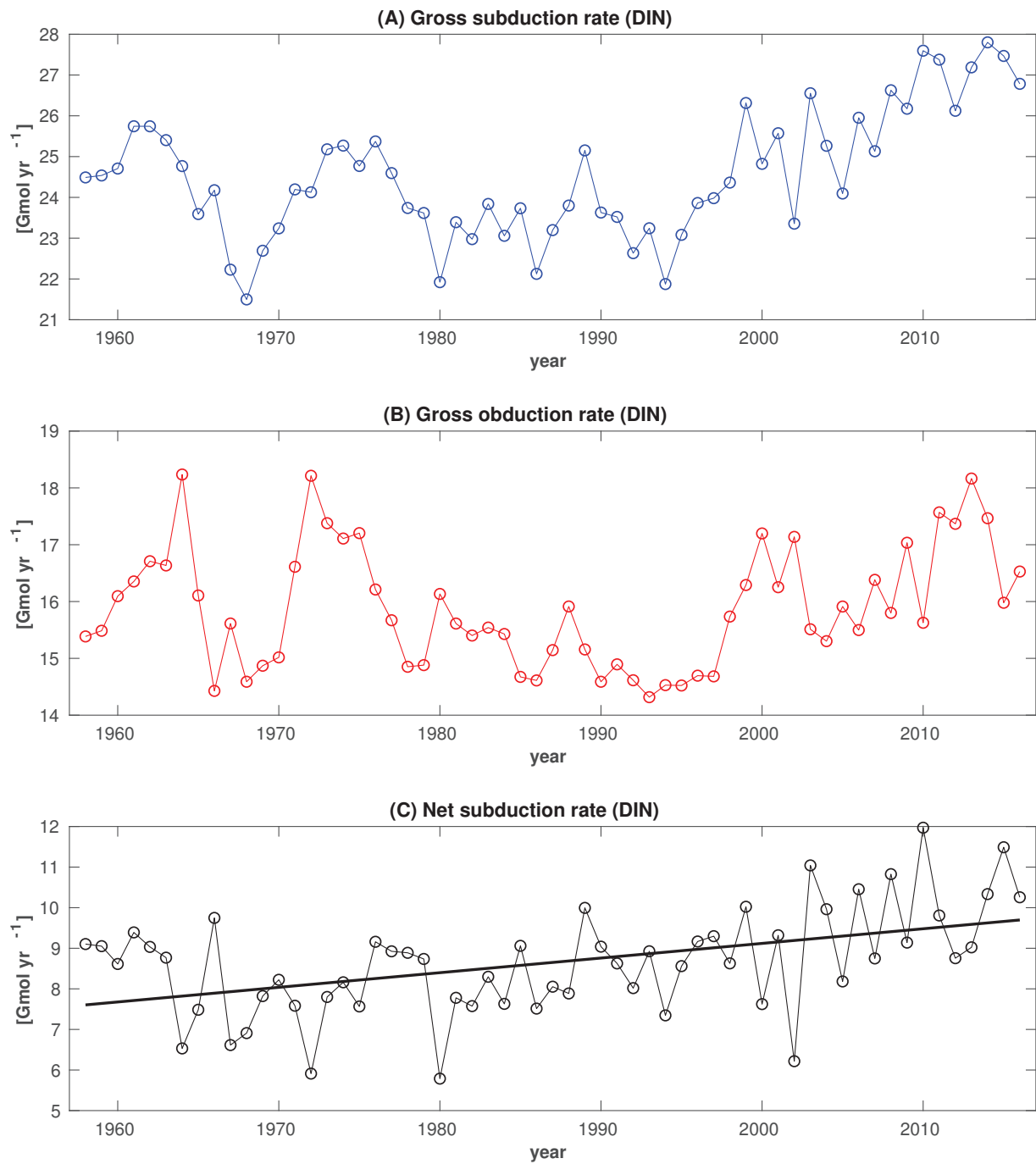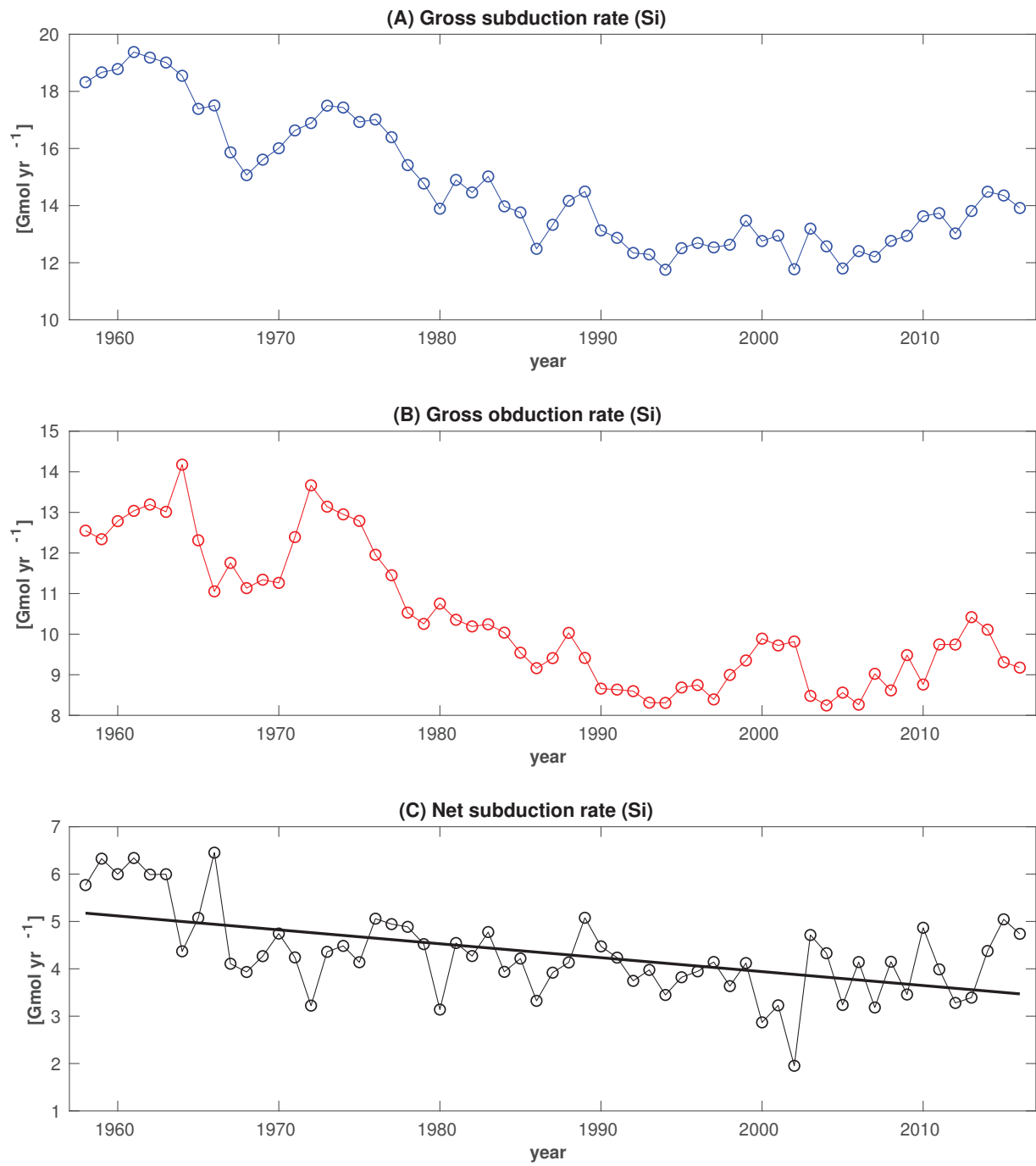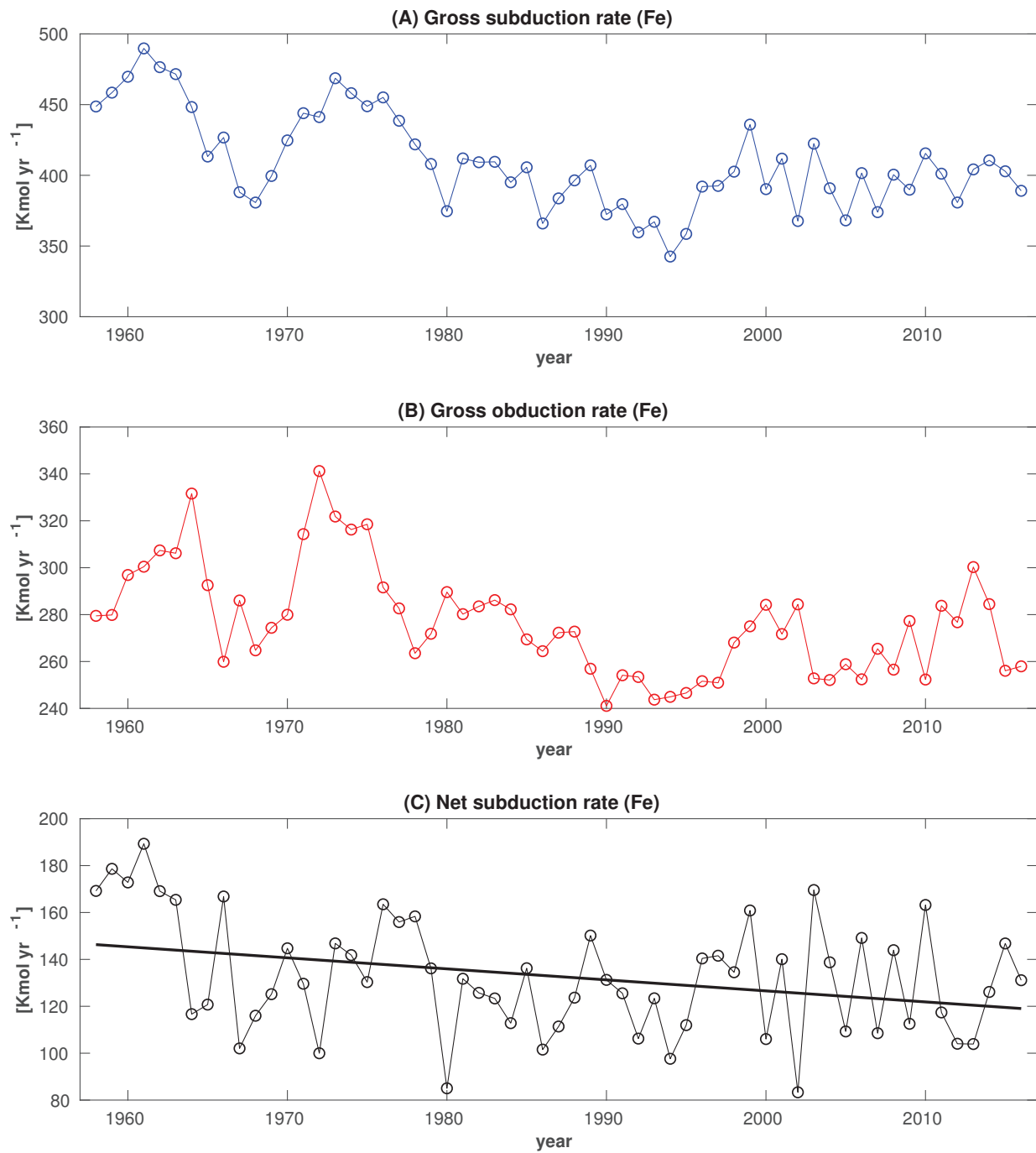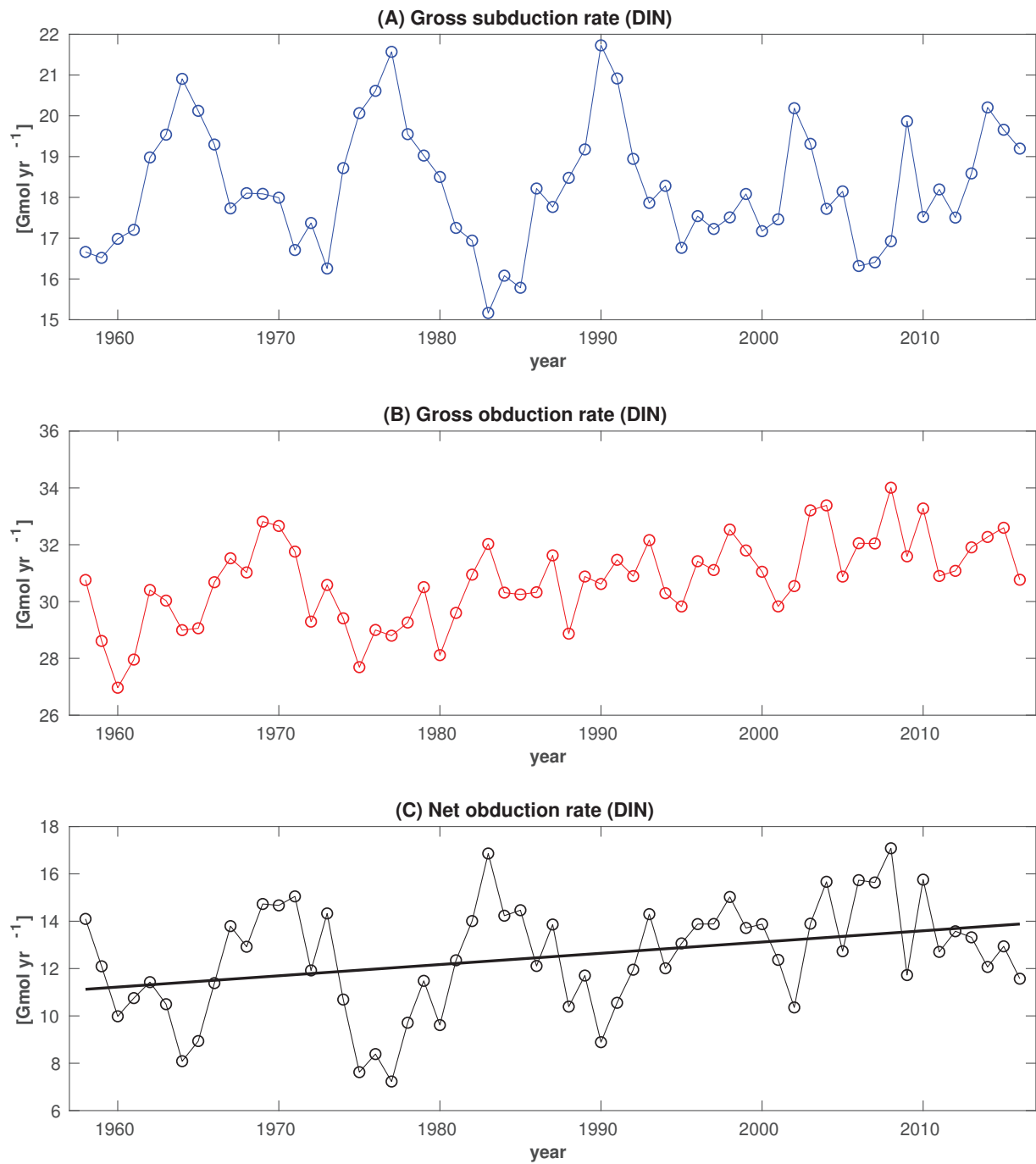
Figure 5.13: Time series of the total annual obduction rate of DIN from 1958 to 2016 in the density classes with strongest obduction ($1027.3 \leq \sigma_\theta < 1027.5$ kg m^{-3}).
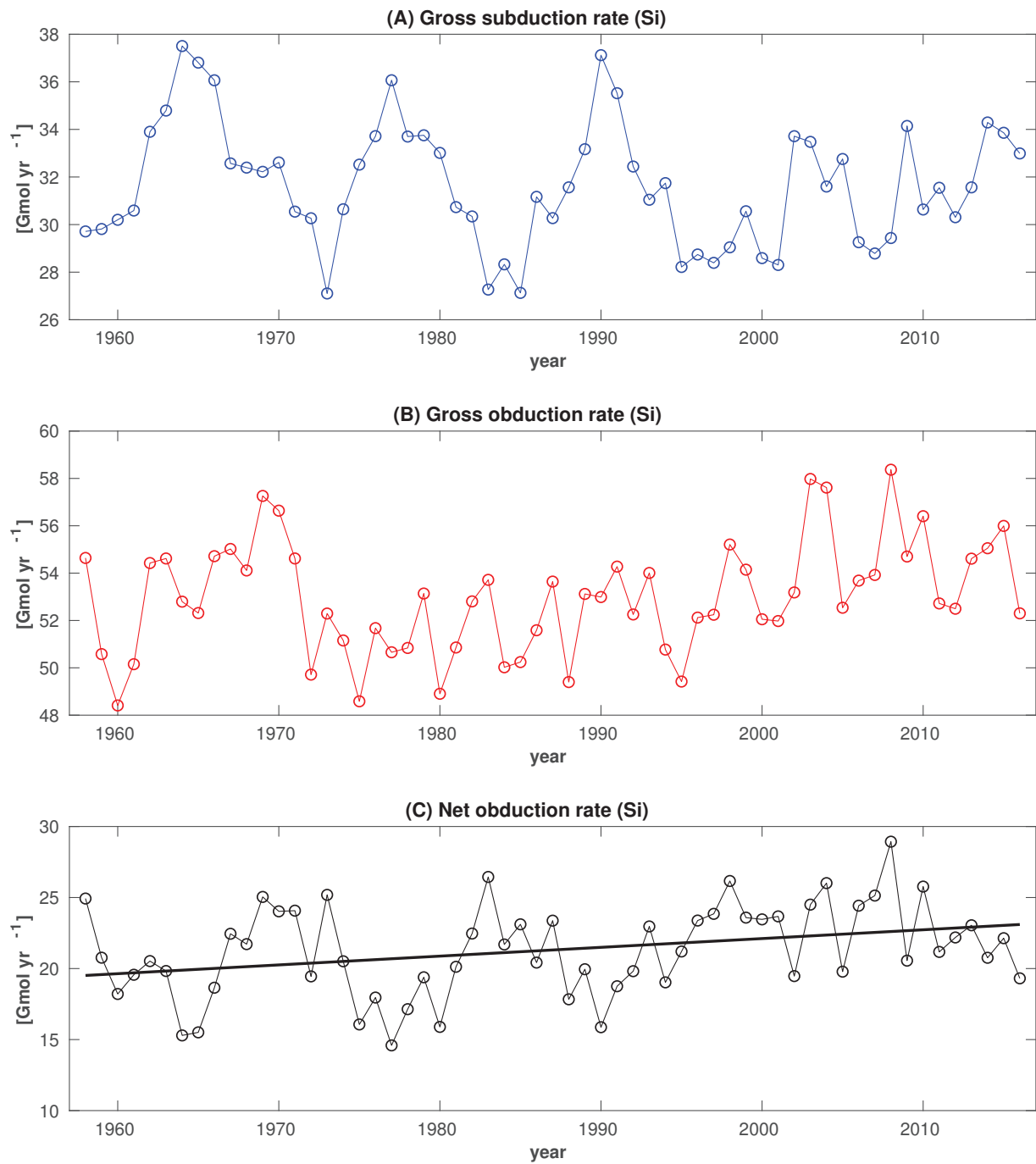
Figure 5.14: Time series of the total annual obduction rate of Si from 1958 to 2016 in the density classes with strongest obduction ($1027.3 \leq \sigma_\theta < 1027.5$ kg m^{-3}).
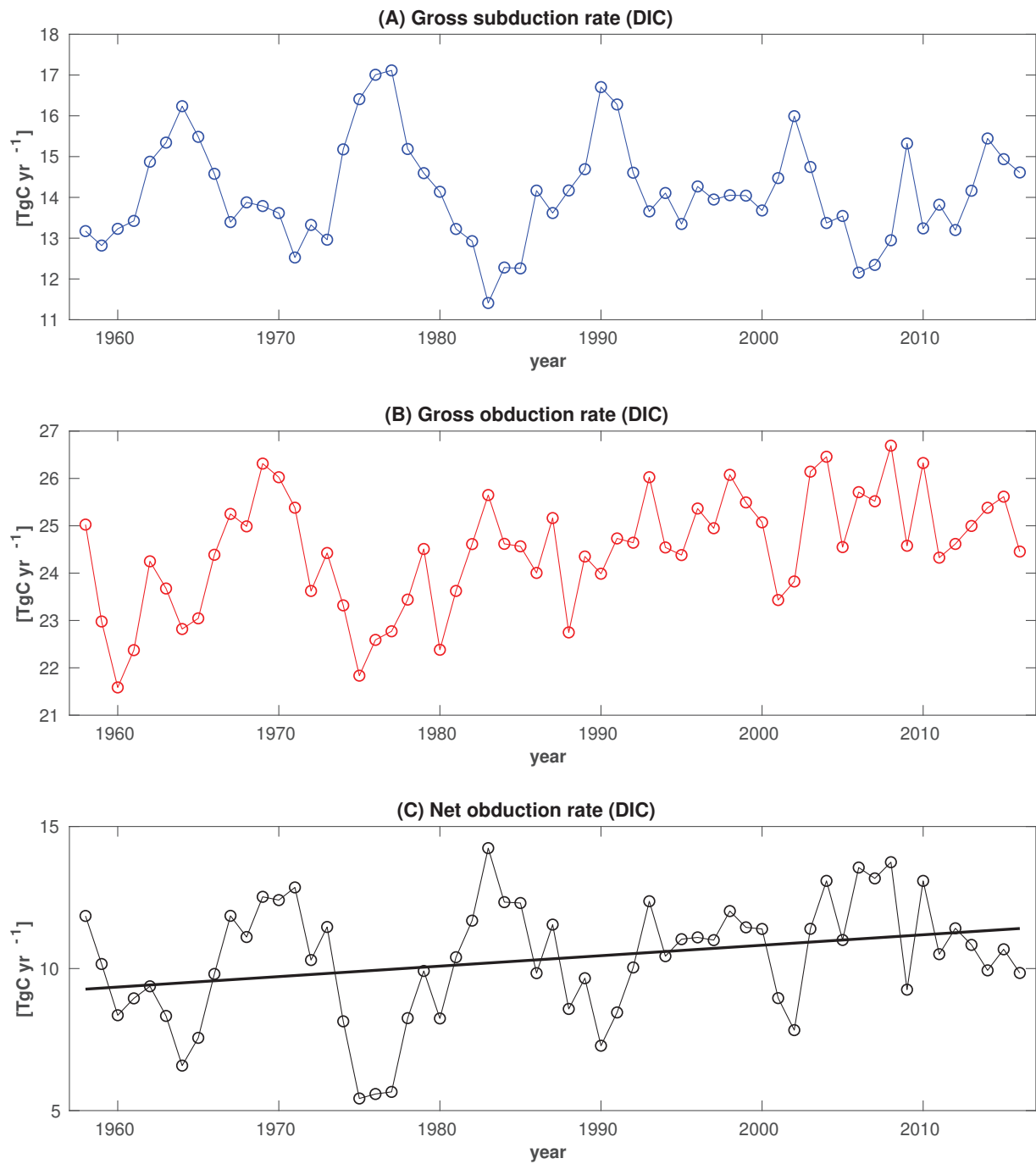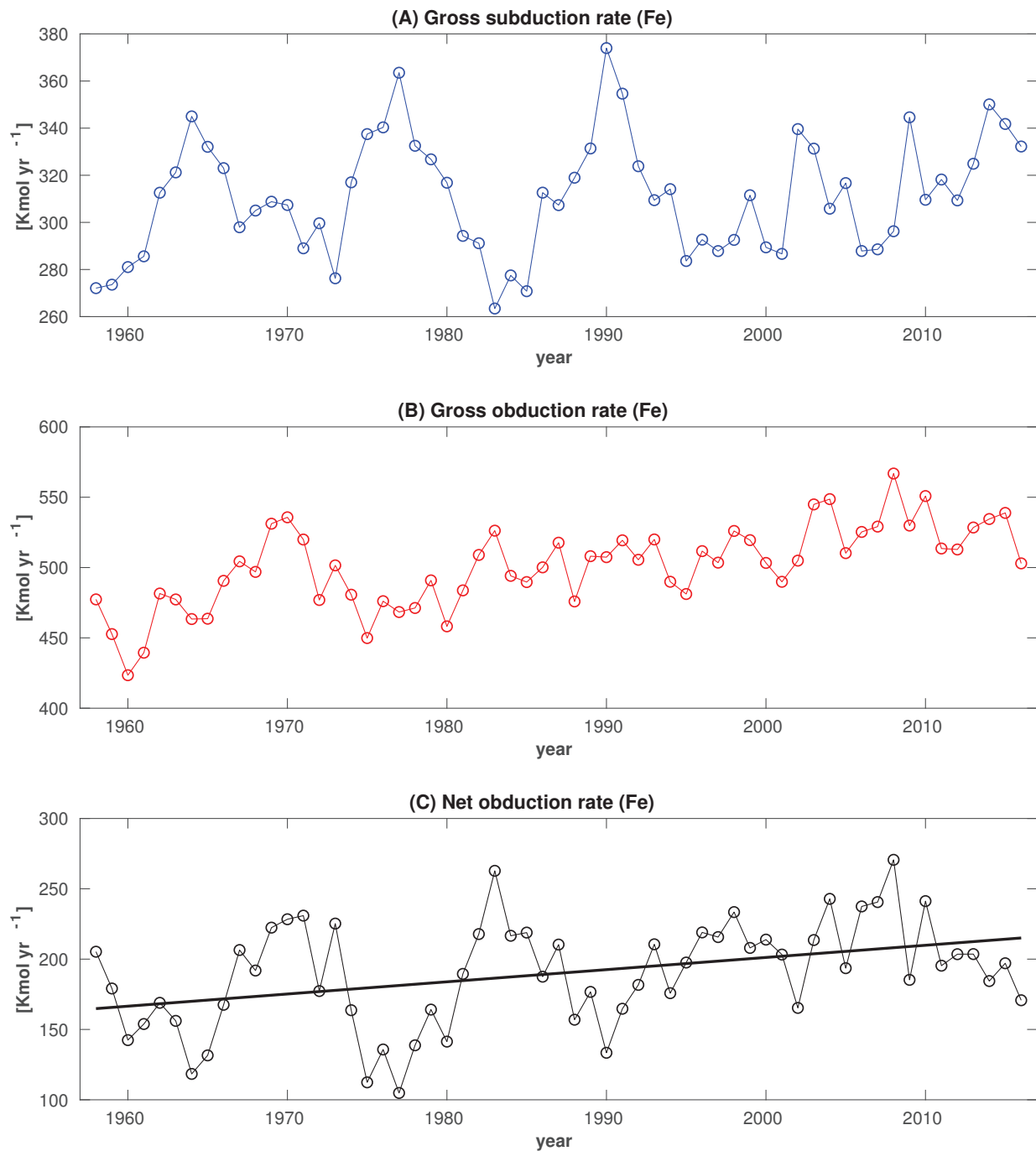
Figure 5.15: Time series of the total annual obduction rate of Fe from 1958 to 2016 in the density classes with strongest obduction ($1027.3 \leq \sigma_\theta < 1027.5$ kg m^{-3}).

5.4 Summary and outlook

Subduction and obduction represent the physical processes that control the transport of water parcels with distinct characteristics across the base of the winter mixed layer

from the mixed layer to the permanent thermocline (subduction) or from the permanent thermocline to the mixed layer (obduction).

The integrated gross subduction rates south of 30°S of volume, carbon and nutrients from the mixed layer across the base of the winter mixed layer averaged between 1958 to 2016 are estimated to be 200.6 Sv for volume, 167.7 PgC yr^{-1} for DIC, 113.9 Tmol yr^{-1} for DIN, 159.8 Tmol yr^{-1} for Si and 2.0 Gmol yr^{-1} for Fe.

The integrated gross obduction rates south of the 30°S of volume, carbon and nutrients from the permanent thermocline across the base of the winter mixed layer averaged between 1958 to 2016 are estimated to be -177.4 Sv for volume, -151.0 PgC yr^{-1} for DIC, -135.5 Tmol yr^{-1} for DIN, -203.7 Tmol yr^{-1} for Si and -2.3 Gmol yr^{-1} for Fe.

The response of the subduction rates of carbon and nutrients to the positive trend in the Southern Annular Mode (SAM) index is zonally symmetric. In fact, the positive phase of the SAM leads to positive subduction rate anomalies of carbon and nutrients north of the Antarctic Polar Front (APF) and negative obduction rate anomalies south of the APF.

The time series of subduction and obduction rates of carbon and nutrients in the density classes of the highest subduction and obduction reveal strong interannual variability from 1958 to the early 1990s, since then obduction and subduction of carbon and nitrate have intensified. While we see an increase in silicic acid and iron obduction over time, the subduction rates of silicic acid and iron show a decrease.

With respect to the response to SAM, the net DIC and nutrient subduction rates in the density classes of the highest subduction rate ($1026.5 < \sigma_\theta < 1026.7$ kg m^{-3}) increased by 0.8 Tg DIC yr^{-1}, 0.5 Gmol DIN yr^{-1}, 0.05 Gmol Si yr^{-1} and 4.4 Kmol Fe yr^{-1} for a one unit increase in the SAM index. The net increase in obduction rates of carbon and nutrients in the density classes of the highest obduction rate ($1027.3 \leq \sigma_\theta < 1027.5$ kg m^{-3}) was estimated to be 0.5 Tg DIC yr^{-1}, 0.6 Gmol DIN yr^{-1}, 0.9 Gmol Si yr^{-1} and 9.3 Kmol Fe yr^{-1} for a one unit increase in the SAM index.

This study focused only on the quantification of variability of carbon and nutrient subduction across the winter mixed layer depth south of 30°S. This should be refined to the Subantarctic Mode Water and Antarctic Intermediate Waters, the dominant water masses for subduction. While their density classes were considered in this study, the exact representation of these water masses in the model in each sector of the SO will have to be checked based on their characteristic salinity and vorticity distributions. Doing that we can quantify the relative contribution of each Southern Ocean sector (Pacific, Atlantic, and Indian) to the integrated Southern Ocean carbon and nutrient fluxes that we quantified in this study.

Further work will include an analysis of the model control simulation for a possible

model drift that could affect the results and application of a correction if needed.

In the current version, changes in the subduction and obduction rates are only caused by changes in vertical and horizontal advection rates because we keep the maximum MLD constant in time. We will also aim to take into account the interannual variability of the MLD for the subduction rate calculation.

The available model output can then also be used to calculate the mean overturning rates for the 1980s, 1990s and 2000s as in *DeVries et al.* (2017) to test their hypothesis that the Southern Ocean overturning has weakened in the 2000s.

In general, repeating the same model experiment with a high-resolution model to fully resolve the effect of mesoscale processes on the carbon and nutrient subduction rates would be desirable.

References

Bopp, L., M. Lévy, L. Resplandy, and J.-B. Sallée (2015), Pathways of anthropogenic carbon subduction in the global ocean, *Geophysical Research Letters*, *42*(15), 6416–6423, doi: 10.1002/2015GL065073.

Cerovečki, I., L. D. Talley, M. R. Mazloff, and G. Maze (2013), Subantarctic Mode Water Formation, Destruction, and Export in the Eddy-Permitting Southern Ocean State Estimate, *Journal of Physical Oceanography*, *43*(7), 1485–1511, doi:10.1175/JPO-D-12-0121.1.

Conkright, M. E., T. P. Boyer, and S. Levitus (1994), *World Ocean Atlas: 1994 Nutrients*, vol. 1, DIANE Publishing.

de Boyer Montégut, C., G. Madec, A. S. Fischer, A. Lazar, and D. Iudicone (2004), Mixed layer depth over the global ocean: An examination of profile data and a profile-based climatology, *Journal of Geophysical Research: Oceans*, *109*(C12003), doi:10.1029/2004JC002378.

DeVries, T., M. Holzer, and F. Primeau (2017), Recent increase in oceanic carbon uptake driven by weaker upper-ocean overturning, *Nature*, *542*(7640), 215–218, doi:10.1038/nature21068.

Downes, S., A. Budnick, J. Sarmiento, and R. Farneti (2011), Impacts of wind stress on the Antarctic Circumpolar Current fronts and associated subduction, *Geophysical Research Letters*, *38*(L11605), doi:10.1029/2011GL047668.

Downes, S. M., N. L. Bindoff, and S. R. Rintoul (2009), Impacts of Climate Change on the Subduction of Mode and Intermediate Water Masses in the Southern Ocean, *Journal of Climate*, *22*(12), 3289–3302, doi:10.1175/2008JCLI2653.1.

Downes, S. M., N. L. Bindoff, and S. R. Rintoul (2010), Changes in the Subduction of Southern Ocean Water Masses at the End of the Twenty-First Century in Eight IPCC Models, *Journal of Climate*, *23*(24), 6526–6541, doi:10.1175/2010JCLI3620.1.

Downes, S. M., C. Langlais, J. P. Brook, and P. Spence (2017), Regional Impacts of the Westerly Winds on Southern Ocean Mode and Intermediate Water Subduction, *Journal of Physical Oceanography*, *47*(10), 2521–2530, doi:10.1175/JPO-D-17-0106.1.

Gent, P. R., and J. C. McWilliams (1990), Isopycnal mixing in ocean circulation models, *Journal of Physical Oceanography*, *20*(1), 150–155, doi:10.1175/1520-0485(1990)020$< 0150 : IMIOCM > 2.0.CO; 2$.

Gille, S. T. (2008), Decadal-scale temperature trends in the Southern Hemisphere ocean, *Journal of Climate*, *21*(18), 4749–4765, doi:10.1175/2008JCLI2131.1.

Gruber, N., M. Gloor, S. E. Mikaloff Fletcher, S. C. Doney, S. Dutkiewicz, M. J. Follows, M. Gerber, A. R. Jacobson, F. Joos, K. Lindsay, et al. (2009), Oceanic sources, sinks, and transport of atmospheric CO_2, *Global Biogeochemical Cycles*, *23*(GB1005), 1924–9224, doi:10.1029/2008GB003349.

Hauck, J., C. Völker, T. Wang, M. Hoppema, M. Losch, and D. A. Wolf-Gladrow (2013), Seasonally different carbon flux changes in the Southern Ocean in response to the southern annular mode, *Global Biogeochemical Cycles*, *27*(4), 1236–1245, doi:10.1002/2013GB004600.

Hauck, J., C. Völker, D. Wolf-Gladrow, C. Laufkötter, M. Vogt, O. Aumont, L. Bopp, E. T. Buitenhuis, S. C. Doney, J. Dunne, et al. (2015), On the Southern Ocean CO_2 uptake and the role of the biological carbon pump in the 21st century, *Global Biogeochemical Cycles*, *29*(9), 1451–1470, doi:10.1002/2015GB005140.

Hauck, J., P. Köhler, D. Wolf-Gladrow, and C. Völker (2016), Iron fertilisation and century-scale effects of open ocean dissolution of olivine in a simulated CO_2 removal experiment, *Environmental Research Letters*, *11*(2), 024,007, doi:10.1088/1748-9326/11/2/024007.

Holzer, M., and F. W. Primeau (2013), Global teleconnections in the oceanic phosphorus cycle: Patterns, paths, and timescales, *Journal of Geophysical Research: Oceans*, *118*(4), 1775–1796, doi:10.1002/jgrc.20072.

Hoppema, M., K. Bakker, S. M. van Heuven, J. C. van Ooijen, and H. J. de Baar (2015), Distributions, trends and inter-annual variability of nutrients along a repeat section through the Weddell Sea (1996–2011), *Marine Chemistry*, *177*, 545–553, doi:10.1016/j.marchem.2015.08.007.

Iudicone, D., K. B. Rodgers, Y. Plancherel, O. Aumont, T. Ito, R. M. Key, G. Madec, and M. Ishii (2016), The formation of the ocean's anthropogenic carbon reservoir, *Scientific Reports*, *6*, 35,473, doi:10.1038/srep35473.

Jones, D. C., A. J. Meijers, E. Shuckburgh, J.-B. Sallée, P. Haynes, E. K. McAufield, and M. R. Mazloff (2016), How does Subantarctic Mode Water ventilate the Southern Hemisphere subtropics?, *Journal of Geophysical Research: Oceans*, *121*(9), 6558–6582, doi:10.1002/2016JC011680.

Kalnay, E., M. Kanamitsu, R. Kistler, W. Collins, D. Deaven, L. Gandin, M. Iredell, S. Saha, G. White, J. Woollen, et al. (1996), The NCEP/NCAR 40-year reanalysis project, *American Meteorological Society*, *77*(3), 437–471, doi:10.1175/1520-0477(1996)077$< 0437 : TNYRP > 2.0.CO; 2$.

Khatiwala, S., F. Primeau, and T. Hall (2009), Reconstruction of the history of anthropogenic CO_2 concentrations in the ocean, *Nature*, *462*(7271), 346–349, doi:10.1038/nature08526.

Kwon, E. Y. (2013), Temporal variability of transformation, formation, and subduction rates of upper Southern Ocean waters, *Journal of Geophysical Research: Oceans*, *118*(11), 6285–6302, doi:10.1002/2013JC008823.

Langlais, C., A. Lenton, R. Matear, D. Monselesan, B. Legresy, E. Cougnon, and S. Rintoul (2017), Stationary Rossby waves dominate subduction of anthropogenic carbon in the Southern Ocean, *Scientific Reports*, *7*(1), 17,076, doi:10.1038/s41598-017-17292-3.

Large, W. G., J. C. McWilliams, and S. C. Doney (1994), Oceanic vertical mixing: A review and a model with a nonlocal boundary layer parameterization, *Reviews of Geophysics*, *32*(4), 363–403, doi:10.1029/94RG01872.

Laubscher, R., R. Perissinotto, and C. McQuaid (1993), Phytoplankton production and biomass at frontal zones in the Atlantic sector of the Southern Ocean, *Polar Biology*, *13*(7), 471–481, doi:10.1007/BF00233138.

Le Quéré, C., R. M. Andrew, J. G. Canadell, S. Sitch, J. I. Korsbakken, G. P. Peters, et al. (2016), Global Carbon Budget 2016, *Earth Syst. Sci. Data*, *8*, 605–649, doi:10.5194/essd-8-605-2016.

Le Quéré, C., R. M. Andrew, P. Friedlingstein, S. Sitch, J. Pongratz, A. C. Manning, J. I. Korsbakken, G. P. Peters, J. G. Canadell, R. B. Jackson, et al. (2017), Global Carbon Budget 2017, *Earth System Science Data Discussions*, pp. 1–79, doi:10.5194/essd-2017-123.

Lévy, M., L. Bopp, P. Karleskind, L. Resplandy, C. Éthé, and F. Pinsard (2013), Physical pathways for carbon transfers between the surface mixed layer and the ocean interior, *Global Biogeochemical Cycles*, *27*(4), 1001–1012, doi:10.1002/gbc.20092.

Liu, L. L., and R. X. Huang (2012), The Global Subduction/Obduction Rates: Their Interannual and Decadal Variability, *Journal of Climate*, *25*(4), 1096–1115, doi:10.1175/2011JCLI4228.1.

Losch, M., D. Menemenlis, J.-M. Campin, P. Heimbach, and C. Hill (2010), On the formulation of sea-ice models. Part 1: Effects of different solver implementations and parameterizations, *Ocean Modelling*, *33*(1), 129–144, doi:10.1016/j.ocemod.2009.12.008.

Lumpkin, R., and K. Speer (2007), Global ocean meridional overturning, *Journal of Physical Oceanography*, *37*(10), 2550–2562, doi:10.1175/JPO3130.1.

Marshall, G. J. (2003), Trends in the Southern Annular Mode from observations and reanalyses, *Journal of Climate*, *16*(24), 4134–4143, doi:10.1175/1520-0442(2003)016$< 4134 : TITSAM >$ $2.0.CO; 2$.

Marshall, J., and K. Speer (2012), Closure of the meridional overturning circulation through Southern Ocean upwelling, *Nature Geoscience*, *5*(3), 171–180, doi:10.1038/NGEO1391.

Marshall, J., A. Adcroft, C. Hill, L. Perelman, and C. Heisey (1997), A finite-volume, incompressible Navier Stokes model for studies of the ocean on parallel computers, *Journal of Geophysical Research: Oceans*, *102*(C3), 5753–5766, doi:10.1029/96JC02775.

Marshall, J. C., R. G. Williams, and A. G. Nurser (1993), Inferring the subduction rate and period over the North Atlantic, *Journal of Physical Oceanography*, *23*(7), 1315–1329, doi: 10.1175/1520-0485(1993)023$< 1315 : ITSRAP >$ $2.0.CO; 2$.

Martínez-García, A., D. M. Sigman, H. Ren, R. F. Anderson, M. Straub, D. A. Hodell, S. L. Jaccard, T. I. Eglinton, and G. H. Haug (2014), Iron Fertilization of the Subantarctic Ocean During the Last Ice Age, *Science*, *343*(6177), 1347–1350, doi:10.1126/science.1246848.

Meijers, A. (2014), The Southern Ocean in the Coupled Model Intercomparison Project phase 5, *Phil. Trans. R. Soc. A*, *372*, 20130,296, doi:10.1098/rsta.2013.0296.

Mikaloff Fletcher, S. E., N. Gruber, A. R. Jacobson, M. Gloor, S. C. Doney, S. Dutkiewicz, M. Gerber, M. Follows, F. Joos, K. Lindsay, et al. (2007), Inverse estimates of the oceanic sources and sinks of natural CO_2 and the implied oceanic carbon transport, *Global Biogeochemical Cycles*, *21*(GB1010), doi:10.1029/2006GB002751.

Orsi, A. H., T. Whitworth, and W. D. Nowlin (1995), On the meridional extent and fronts of the Antarctic Circumpolar Current, *Deep Sea Research Part I: Oceanographic Research Papers*, *42*(5), 641–673, doi:10.1016/0967-0637(95)00021-W.

Palter, J., J. Sarmiento, A. Gnanadesikan, J. Simeon, and R. Slater (2010), Fueling export production: Nutrient return pathways from the deep ocean and their dependence on the Meridional Overturning Circulation, *Biogeosciences*, *7*(11), 3549–3568, doi:10.5194/bg-7-3549-2010.

Panassa, E., J. M. Santana-Casiano, M. González-Dávila, M. Hoppema, S. M. van Heuven, C. Völker, D. Wolf-Gladrow, and J. Hauck (2018), Variability of nutrients and carbon dioxide in the Antarctic Intermediate Water between 1990 and 2014, *Ocean Dynamics*, *68*(3), 295–308, doi:10.1007/s10236-018-1131-2.

Pardo, P. C., B. Tilbrook, C. Langlais, T. W. Trull, and S. R. Rintoul (2017), Carbon uptake and biogeochemical change in the Southern Ocean, south of Tasmania, *Biogeosciences*, *14*(22), 5217–5237, doi:10.5194/bg-14-5217-2017.

Sabine, C. L., R. A. Feely, N. Gruber, R. M. Key, K. Lee, J. L. Bullister, R. Wanninkhof, C. Wong, D. W. Wallace, B. Tilbrook, et al. (2004), The oceanic sink for anthropogenic CO_2, *Science*, *305*(5682), 367–371, doi:10.1126/science.1097403.

Sallée, J.-B., K. Speer, S. Rintoul, and S. Wijffels (2010), Southern Ocean Thermocline Ventilation, *Journal of Physical Oceanography*, *40*(3), 509–529, doi:10.1175/2009JPO4291.1.

Sallée, J.-B., R. J. Matear, S. R. Rintoul, and A. Lenton (2012), Localized subduction of anthropogenic carbon dioxide in the Southern Hemisphere oceans, *Nature Geoscience*, *5*(8), 579–584, doi:10.1038/ngeo1523.

Sarmiento, J., N. Gruber, M. Brzezinski, and J. Dunne (2004), High-latitude controls of thermocline nutrients and low latitude biological productivity, *Nature*, *427*(6969), 56–60, doi:10.1038/nature02204.

Swart, N., and J. Fyfe (2012), Observed and simulated changes in the Southern Hemisphere surface westerly wind-stress, *Geophysical Research Letters*, *39*(16), doi:10.1029/2012GL052810.

Talley, L. D. (2013), Closure of the global overturning circulation through the Indian, Pacific, and Southern Oceans: Schematics and transports, *Oceanography*, *26*(1), 80–97, doi:10.5670/oceanog.2013.07.

Tanhua, T., M. Hoppema, E. M. Jones, T. Stöven, J. Hauck, M. G. Dávila, M. Santana-Casiano, M. Álvarez, and V. H. Strass (2017), Temporal changes in ventilation and the carbonate system in the Atlantic sector of the Southern Ocean, *Deep Sea Research Part II: Topical Studies in Oceanography*, *138*, 26–38, doi:10.1016/j.dsr2.2016.10.004.

Thompson, D. W., S. Solomon, P. J. Kushner, M. H. England, K. M. Grise, and D. J. Karoly (2011), Signatures of the Antarctic ozone hole in Southern Hemisphere surface climate change, *Nature Geoscience*, *4*(11), 741–749, doi:10.1038/NGEO1296.

Zheng, F., J. Li, R. T. Clark, and H. C. Nnamchi (2013), Simulation and Projection of the Southern Hemisphere Annular Mode in CMIP5 Models, *Journal of Climate*, *26*(24), 9860–9879, doi:10.1175/JCLI-D-13-00204.1.

Chapter 6

Synthesis

The Southern Ocean (SO) climate system is changing (e.g. *Gille*, 2008; *Thompson et al.*, 2011; *Jones et al.*, 2016a; *Haumann et al.*, 2016) and is expected to continue to do so in the future under high-CO_2 forcing (*Meijers*, 2014). The Southern Annular Mode (SAM) is the main atmospheric mode of variability that also controls variability of ocean circulation in the SO. During a positive phase of SAM, the westerly wind belt strengthens and moves towards Antarctica (*Sokolov and Rintoul*, 2009b; *Thompson et al.*, 2011). Over the last two decades, SAM has shifted more to its high index polarity (Figure 6.1) driven by the steady increase of greenhouse gases in the atmosphere in combination with the Antarctic ozone hole caused by the emissions of chlorofluorocarbons (CFCs; *Thompson et al.*, 2011). This has led to the strengthening of westerly winds. At the same time, increasing anthropogenic CO_2 emissions led to global warming. These two processes (wind and temperature forcing) co-occur in the SO (*Gille*, 2008; *Thompson et al.*, 2011). At present-day, changes in wind forcing are likely dominant, as the Southern Ocean experiences sea-surface cooling (*Jones et al.*, 2016a) but subsurface warming (*Gille*, 2008). However, the warming signal might become dominant in the future, as warming trends are expected to continue or even increase (*Kirtman et al.*, 2013). The forcing by wind and warming have opposite effects on the surface mixed layer depth. Increased wind forcing would lead to more ocean mixing and would consequently deepen the mixed layer. In contrast, increased ocean surface warming would lead to stronger surface ocean stratification and shoaling of the mixed layer. The variability of the mixed layer depth (MLD) plays a crucial role in the regulation of heat and gas exchange between ocean and atmosphere (*Sarmiento et al.*, 1998). Also, variations in the MLD control the availability of nutrients and light in the surface ocean, and thereby affect phytoplankton productivity (*Sallée et al.*, 2010a). Furthermore, variations in MLD affect the subduction rates of water masses (*Marshall et al.*, 1993; *Sallée et al.*, 2010a) and could therefore potentially impact carbon and nutrient transport (*Sallée et al.*, 2012). The main subduction path of carbon and nutrients is through the formation of the Subantarctic Mode Water (SAMW) and Antarctic Intermediate Water (AAIW; *Talley*, 2013; *Sallée et al.*, 2012). Coarse resolution models indicate an increase in SAMW and AAIW subduction rates to wind stress increase in the SO (*Downes et al.*, 2011), whereas a recent study with a high-resolution model indicated a decrease in the SAMW and AAIW subduction rates (*Downes et al.*, 2017). Future projections suggest a decrease in SAMW and AAIW subduction rates caused by the increase in ocean warming and shoaling of the winter mixed layer (*Downes et al.*, 2010), though not all models show a decrease in SAMW subduction rate (*Downes et al.*, 2009). This is in spite of a clear trend towards stronger and more poleward atmospheric jets and a positive trend in the SAM (*Gillett and Fyfe*, 2013) and despite a 20% strengthening in the wind-driven upper overturning cell in future projections (*Downes and Hogg*, 2013). While

open questions remain with respect to present and future changes in the subduction rate, no studies exist, to the best of our knowledge, on the variability and change of associated transport of carbon and nutrients. The overall wind forcing effect can be described as follows (Figure 6.2). Stronger westerly winds lead to an increase in upwelling of carbon and nutrient-rich deep water south of the Antarctic Polar Front (APF). This is balanced by the stronger northward Ekman transport of these upwelled waters across and north of the APF where it provokes a deepening of the mixed layer (*Sallée et al.*, 2008) and enhances the carbon and nutrient subduction rates in the AAIW and SAMW. The southward flow that results from surface Ekman divergence in the upwelling zone is directed towards Antarctica, where it either sinks to bottom layers or flows westward within the coastal current.
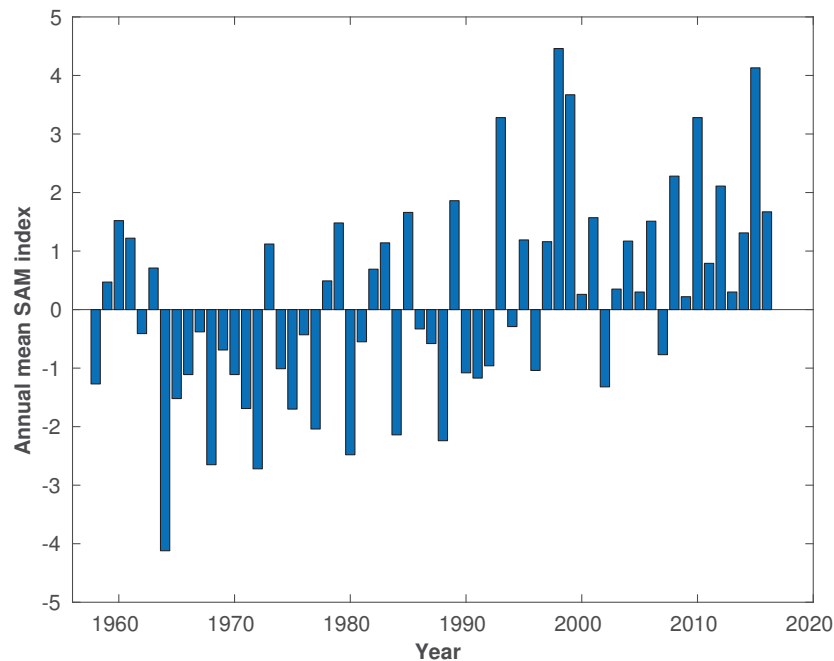
Figure 6.1: Annual mean values of the observation-based Southern Annular Mode (SAM) index (*Marshall*, 2003). Marshall's SAM index is calculated based on the difference in sea-level pressure between 40°S and 65°S.
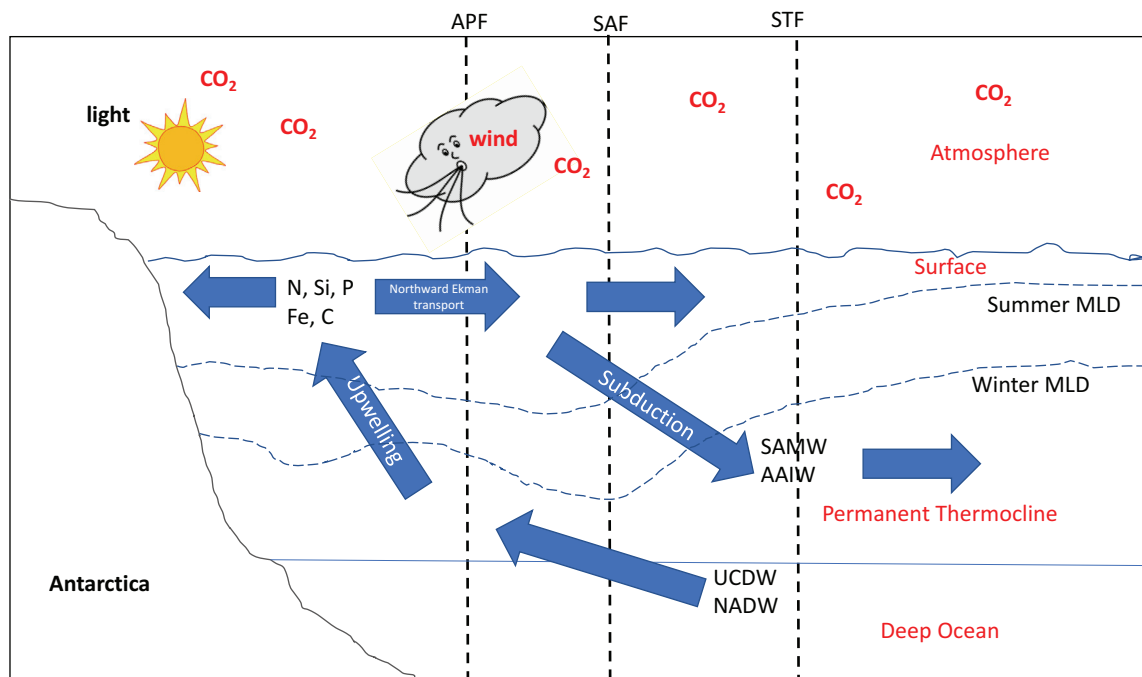
Figure 6.2: The positive SAM has induced an increase in westerly winds and their poleward shift. The wind drives a net surface Ekman transport at 90 degrees to the direction of the surface wind across the Antarctic Polar Front (APF). This leads to a surface divergence and upwelling of carbon and nutrient-rich Upper Circumpolar Deep Water (UCDW) to the surface ocean south of the APF. The northward Ekman transport of surface waters reaches its maximum transport at the APF and the Subantarctic Front (SAF). There, this water converges (Ekman pumping) leading to a deepening of the mixed layer and subduction of water along with its carbon and nutrient content to the ocean interior as intermediate and mode waters (AAIW and SAMW). AAIW: Antarctic Intermediate Water. SAMW: Subantarctic Mode Water. NADW: North Atlantic Deep Water. STF: Subtropical Front.

The main focus of this thesis was to investigate the recent wind forcing along with the global warming impact (1) on the variability of carbon and nutrient concentrations in the Antarctic Intermediate Water of the Atlantic sector of the SO based on observational data (chapter 3), (2) on the Southern Ocean summer mixed layer depth and its variability (chapter 4) and (3) on the carbon and nutrient transport across the base of the winter mixed layer at large scale analyzing output from an ocean biogeochemical model (chapter 5). The main results and their implications are discussed below.

(1) How does wind forcing in the SO affect the interannual variability of carbon and nutrient concentrations in mode and intermediate waters (SAMW and AAIW), that link

the Southern Ocean with lower latitude surface waters on shorter time-scales than the Antarctic Bottom Water transport, that transports two to three times more water volume across 30°S than AAIW and SAMW together (*Talley*, 2013)? To answer this question from in-situ observational data is challenging, because observations are sparse. Previous studies of *Pardo et al.* (2017), *Ayers and Strutton* (2013), and *Iida et al.* (2013) analyzed the variability of carbon and nutrient concentrations in the SO except in the Atlantic sector. *Pardo et al.* (2017) found that a DIC increase in the SAMW and AAIW and an increase in silicate and salinity in the Antarctic divergence zone between 1995-2011 in the Australian sector and linked the changes observed to the intensification of upwelling. *Iida et al.* (2013) found a long-term increase of phosphate and nitrate in intermediate depths south of the APF in the Indian Ocean sector between 1965 and 2008. *Ayers and Strutton* (2013) depicted a high interannual variability in nutrients in the SAMW between 1991 to 2001 that is correlated with the SAM index. They found that for a one unit increase in the SAM index, phosphate and nitrate increased by 3% and temperature decreased by 0.5°C. *Ayers and Strutton* (2013) argue that increased westerlies in response to a positive SAM phase lead to increased upwelling of nutrients in high latitudes that is balanced by a stronger northward Ekman transport, followed by a higher subduction of nutrients in the SAMW. In chapter 3 of this thesis, I focused on the AAIW and analyzed carbon and nutrients along with hydrographic data (salinity and temperature) in the Atlantic sector of the SO. I found that dissolved inorganic carbon and nitrate concentrations increased along with a decrease in temperature and salinity between 1990 and 2014. This indicates a scenario of an increase in the upwelling rate in the Atlantic sector, balanced by a stronger northward Ekman transport with larger subduction rates of carbon and unutilized nutrients in the AAIW of the Atlantic sector. My analysis and other regional studies (*Ayers and Strutton*, 2013; *Iida et al.*, 2013; *Pardo et al.*, 2017; *Hoppema et al.*, 2015) suggest that the changes I observed are likely related to the positive phase in SAM over the last two decades (Figure 6.1). This also highlights that the recent changes in the atmospheric circulation related to the positive trend in SAM have not only induced significant changes at the ocean surface (*Jones et al.*, 2016a) but perturb also the ocean interior as shown here for carbon and nutrient concentrations in the AAIW.

(2) How does the intensification of westerlies in response to the trend towards a more positive SAM index along with the global warming signal affect the ocean mixed layer depth? While *Sallée et al.* (2010a) analyzed the annual mean mixed layer depth response to SAM (wind forcing), there is at present no study on the seasonal wind effect on the SO mixed layer depth. The *Sallée et al.* (2010a) study is based on observations, that -on their own- cannot provide proof of the mechanisms that drive the mixed layer variability.

In chapter 4 of this thesis, I focus on the analysis of summer mixed layer depth variability and quantify the relative contribution of the effects of wind and temperature changes independently on the summer mixed layer variability by combining observations and model MLD sensitivity experiments. The results suggest that summer MLD variability over the decade 2002-2011 can be largely explained by a linear zero-lag response to summer wind and air temperature changes and that wind forcing dominates over temperature. The response of the summer mixed layer depth to recent atmospheric forcing is zonally asymmetric but the pattern of change differs from the zonally asymmetric response found by *Sallée et al.* (2010a). My study is the first that attempts to split the effects of wind and temperature forcing by a linear approach using a three-dimensional model experiment. It suggests that the future projections of the SO mixed layer change in a high-CO_2 world will critically depend on the expected changes in atmospheric wind forcing and temperature. While wind forcing dominates the summer MLD response today, this might change in the future with a stronger warming signal.

(3) While *Hauck et al.* (2013) analyzed vertical carbon fluxes across 100 m depth in response to SAM, an overview of the carbon and nutrient fluxes across the base of the winter mixed layer that takes also horizontal transports into account, had not been performed yet. Analyzing these processes is an important research question as the subduction of nutrients and their transport equatorwards help to fuel 15 to 75% of primary productivity in low latitudes (*Sarmiento et al.*, 2004; *Palter et al.*, 2010; *Holzer and Primeau*, 2013). In chapter 5 of this thesis, I address this research question using a three-dimensional model that is driven by interannually varying atmospheric forcing fields. I analyzed changes of the carbon and nutrient subduction rates (vertical and horizontal) across the base of the winter mixed layer with respect to interannual variability and response to the positive trend in the SAM index. I found a positive trend in carbon and nutrient obduction rates in the density range that showed the highest rates of obduction (upwelling region) since the 1990s in comparison to the pre-1990s period which is characterized more by interannual rather than decadal variability. Similarly, carbon and nitrate subduction rates in the density range that showed the highest rates of subduction (subduction region) showed a positive trend, whereas silicate and iron subduction rates decreased. Overall, the positive phase of the SAM leads to more carbon and nutrient obduction south of the APF and enhanced carbon and nutrient subduction north of the APF. Overall, the obduction rate changes in the upwelling region are larger than the subduction rate changes for nutrients in response to SAM. In contrast, changes in DIC subduction rate are stronger than the obduction rate changes in the upwelling region in response to SAM. This can be explained by the uptake of anthropogenic CO_2 and its subsequent subduction. This indicates that

the intensification of westerly winds in the SO has profoundly perturbed the oceanic circulation over the last decades and affects the subduction rates.

Also, the response of the modelled summer mixed layer depth to the SAM (chapter 5) agrees very well with the observed positive trend of summer MLD between 2002 and 2011 (chapter 4). The data-based analysis revealed a deepening of the mixed layer south of the Subantarctic Front (SAF) in the Atlantic and Indian sectors and in the Pacific ACC region, which was shown to be dominantly driven by changes in the wind forcing (chapter 4). This confirms that changes in MLD are caused by the SAM trend and are strongest during summer (*Thompson et al.*, 2011).

Also, the analysis of the variability of carbon and nutrient subduction rates across the base of the winter mixed layer based on the model study (chapter 5) goes in the right direction, supporting the hypothesis of increased subduction to explain the positive trend in the carbon and nitrate concentrations in the AAIW (chapter 3). The model result of the negative trend in the silicic acid and iron subduction rates may well explain the non-significant trend of silicic acid that we observed in the AAIW (chapter 3). Nevertheless, we cannot make a direct comparison between the strong positive trend we observed in the carbon and nitrate subduction rates since the 1990s (chapter 5) and the positive trend in nutrient concentrations in the AAIW explicitly (chapter 3). This needs more analysis of our results before we can shed light on the physical process responsible for the changes in carbon and nutrient concentrations that my own and other observational studies depicted in the lighter density mode and intermediate waters.

Future research perspectives   The analysis of carbon and nutrient variability in the Atlantic sector presented in chapter 3 focused only on the AAIW. This should be extended to include SAMW that, together with AAIW, partly fuels the low latitude biological productivity (*Sarmiento et al.*, 2004; *Palter et al.*, 2010; *Holzer and Primeau*, 2013) and both play an important role for uptake of heat and anthropogenic carbon (*Frölicher et al.*, 2015).

In chapter 4, I focus only on the summer season to assess the sensitivity of MLD to the recent wind and temperature forcing. Providing a complete view of the seasonal sensitivities (spring-autumn-winter) and discussing the potential differences between seasons is necessary for a complete view on how the recent changes in atmospheric forcing affect the seasonal mixed layer dynamics. Doing that would increase our understanding of how wind and temperature variability in different seasons have shaped the pattern of the annual mean MLD response to SAM (*Sallée et al.*, 2010a). It is also important to investigate the response of the winter mixed layer depth to SAM variations as winter mixed layer changes have a strong effect on the subduction processes (*Marshall et al.*, 1993; *Sallée*

et al., 2010a; 2012).

Many unresolved questions remain to be investigated to fully address the carbon and nutrient subduction/obduction processes studied in chapter 5:

- Calculate the mean subduction and obduction rates to compare to the *DeVries et al.* (2017) analysis on whether upwelling has increased in the 1990s and decreased in the 2000s

- Conduct a comparative study between chapters 3 and 5 more closely to shed light on the primary physical mechanism responsible for the changes in the carbon and nutrient concentrations in the SAMW and AAIW that I and other studies have described.

- Investigate the regional variability of nutrient and carbon subduction rates summed over the density classes of SAMW-AAIW following *Downes et al.* (2017) to resolve the relative roles of the different sectors in the Southern Ocean.

- Quantify the carbon and nutrient obduction (upwelling) rates in the equatorial region and correlate the changes/variability we find in the Southern Hemisphere subduction rates to the low latitude obduction. This is important if we really want to quantify the relative contribution of the recent SO wind intensification effect on the low latitude productivity (*Sarmiento et al.*, 2004; *Marinov et al.*, 2006; *Palter et al.*, 2010; *Holzer and Primeau*, 2013).

- It would be highly desirable to repeat the same experiment with a high-resolution eddy-resolving model with inter-annual forcing. Coarse model simulations are found to significantly underestimate the inventory of the carbon subduction rate in the SAMW-AAIW density range due to unresolved mesoscale processes (*Langlais et al.*, 2017). The coarse resolution models only take into account eddy parametrizations.

The positive trend in the SAM index has induced significant variability in the surface mixed layer and upwelling rate south of the Antarctic Polar Front (APF). Upwelling and entrainment of macro and micro-nutrients into the surface mixed layer south of the APF increased due to the Ekman divergence in response to stronger surface wind stress curl. While most of the iron and silicic acid (limiting nutrients) get utilized directly by phytoplankton, we see an increase in the lateral transport of the surface carbon and nitrate-rich waters north of the APF and stronger subduction of Subantarctic Mode Water and Antarctic Intermediate Water (SAMW and AAIW), since the 1990s in our model simulation. This finding may well explain the positive trend quantified in carbon and nutrient concentrations in the SAMW and AAIW at basin scale based on the analysis

of observational data since the 1990s. This suggests that in the recent past the wind effect dominated over the warming effect with respect to the mixed layer dynamics and subduction processes and that the upper overturning circulation has increased. In the future, as global warming effect is expected to become dominant over the wind effect, the winter mixed layer is expected to shoal. This will likely reduce the annual mean SAMW and AAIW subduction rates (*Downes et al.*, 2009; 2010; *Meijers*, 2014) and lead to less carbon and nutrient transport out of the Southern Ocean. This might well affect the low latitude primary productivity and carbon budget (*Sarmiento et al.*, 2004; *Marinov et al.*, 2006; *Palter et al.*, 2010; *Holzer and Primeau*, 2013).

References

Abram, N. J., R. Mulvaney, F. Vimeux, S. J. Phipps, J. Turner, and M. H. England (2014), Evolution of the Southern Annular Mode during the past millennium, *Nature Climate Change*, *4*(7), 564–569, doi:10.1038/NCLIMATE2235.

Archer, D., H. Kheshgi, and E. Maier-Reimer (1997), Multiple timescales for neutralization of fossil fuel CO_2, *Geophysical Research Letters*, *24*(4), 405–408, doi:10.1029/97GL00168.

Ayers, J. M., and P. G. Strutton (2013), Nutrient variability in Subantarctic Mode Waters forced by the Southern Annular Mode and ENSO, *Geophysical Research Letters*, *40*(13), 3419–3423, doi:10.1002/grl.50638.

Behrenfeld, M. J. (2010), Abandoning Sverdrup's critical depth hypothesis on phytoplankton blooms, *Ecology*, *91*(4), 977–989, doi:10.1890/09-1207.1.

Böning, C. W., A. Dispert, M. Visbeck, S. Rintoul, and F. U. Schwarzkopf (2008), The response of the Antarctic Circumpolar Current to recent climate change, *Nature Geoscience*, *1*(12), 864–869, doi:10.1038/ngeo362.

Bopp, L., L. Resplandy, J. C. Orr, S. C. Doney, J. P. Dunne, M. Gehlen, P. Halloran, C. Heinze, T. Ilyina, R. Seferian, et al. (2013), Multiple stressors of ocean ecosystems in the 21st century: projections with CMIP5 models, *Biogeosciences*, *10*, 6225–6245, doi:10.5194/bg-10-6225-2013.

Bopp, L., M. Lévy, L. Resplandy, and J.-B. Sallée (2015), Pathways of anthropogenic carbon subduction in the global ocean, *Geophysical Research Letters*, *42*(15), 6416–6423, doi:10.1002/2015GL065073.

Brainerd, K. E., and M. C. Gregg (1995), Surface mixed and mixing layer depths, *Deep Sea Research Part I: Oceanographic Research Papers*, *42*(9), 1521–1543, doi:10.1016/0967-0637(95)00068-H.

Cai, W., G. Shi, T. Cowan, D. Bi, and J. Ribbe (2005), The response of the Southern Annular Mode, the East Australian Current, and the southern mid-latitude ocean circulation to global warming, *Geophysical Research Letters*, *32*(L23706), doi:10.1029/2005GL024701.

Capotondi, A., M. A. Alexander, N. A. Bond, E. N. Curchitser, and J. D. Scott (2012), Enhanced upper ocean stratification with climate change in the CMIP3 models, *Journal of Geophysical Research: Oceans*, *117*(C4), doi:10.1029/2011JC007409.

Cunningham, S., S. Alderson, B. King, and M. Brandon (2003), Transport and variability of the Antarctic Circumpolar Current in Drake Passage, *Journal of Geophysical Research: Oceans*, *108*(C5), 8084, doi:10.1029/2001JC001147.

de Baar, H. J., A. G. Buma, R. F. Nolting, G. C. Cadée, G. Jacques, and P. J. Tréguer (1990), On iron limitation of the Southern Ocean: experimental observations in the Weddell and Scotia Seas, *Marine Ecology Progress Series*, *65*, 105–122.

de Boyer Montégut, C., G. Madec, A. S. Fischer, A. Lazar, and D. Iudicone (2004), Mixed layer depth over the global ocean: An examination of profile data and a profile-based climatology, *Journal of Geophysical Research: Oceans*, *109*(C12003), doi:10.1029/2004JC002378.

Denman, K. (1973), A time-dependent model of the upper ocean, *Journal of Physical Oceanography*, *3*(2), 173–184, doi:10.1175/1520-0485(1973)003$< 0173 : ATDMOT > 2.0.CO; 2$.

DeVries, T., M. Holzer, and F. Primeau (2017), Recent increase in oceanic carbon uptake driven by weaker upper-ocean overturning, *Nature*, *542*(7640), 215–218, doi:10.1038/nature21068.

Dlugokencky, E., and P. Tans (2018), Trends in atmospheric carbon dioxide, National Oceanic & Atmospheric Administration, Earth System Research Laboratory (NOAA/ESRL), https://www.esrl.noaa.gov/gmd/ccgg/trends/global.html.

Dong, S., J. Sprintall, S. T. Gille, and L. Talley (2008), Southern Ocean mixed-layer depth from Argo float profiles, *Journal of Geophysical Research: Oceans*, *113*(C6), doi:10.1029/2006JC004051.

Downes, S., A. Budnick, J. Sarmiento, and R. Farneti (2011), Impacts of wind stress on the Antarctic Circumpolar Current fronts and associated subduction, *Geophysical Research Letters*, *38*(L11605), doi:10.1029/2011GL047668.

Downes, S. M., and A. M. Hogg (2013), Southern Ocean circulation and eddy compensation in CMIP5 models, *Journal of Climate*, *26*(18), 7198–7220, doi:10.1175/JCLI-D-12-00504.1.

Downes, S. M., N. L. Bindoff, and S. R. Rintoul (2009), Impacts of Climate Change on the Subduction of Mode and Intermediate Water Masses in the Southern Ocean, *Journal of Climate*, *22*(12), 3289–3302, doi:10.1175/2008JCLI2653.1.

Downes, S. M., N. L. Bindoff, and S. R. Rintoul (2010), Changes in the Subduction of Southern Ocean Water Masses at the End of the Twenty-First Century in Eight IPCC Models, *Journal of Climate*, *23*(24), 6526–6541, doi:10.1175/2010JCLI3620.1.

Downes, S. M., C. Langlais, J. P. Brook, and P. Spence (2017), Regional Impacts of the Westerly Winds on Southern Ocean Mode and Intermediate Water Subduction, *Journal of Physical Oceanography*, *47*(10), 2521–2530, doi:10.1175/JPO-D-17-0106.1.

Dugdale, R., and J. Goering (1967), Uptake of new and regenerated forms of nitrogen in primary productivity, *Limnology and Oceanography*, *12*(2), 196–206, doi:10.4319/lo.1967.12.2.0196.

Durack, P. J., S. E. Wijffels, and R. J. Matear (2012), Ocean salinities reveal strong global water cycle intensification during 1950 to 2000, *Science*, *336*(6080), 455–458, doi:10.1126/science.1212222.

England, M. H., S. McGregor, P. Spence, G. A. Meehl, A. Timmermann, W. Cai, A. S. Gupta, M. J. McPhaden, A. Purich, and A. Santoso (2014), Recent intensification of wind-driven circulation in the Pacific and the ongoing warming hiatus, *Nature Climate Change*, *4*(3), 222–227, doi:10.1038/NCLIMATE2106.

Fahrbach, E., M. Hoppema, G. Rohardt, O. Boebel, O. Klatt, and A. Wisotzki (2011), Warming of deep and abyssal water masses along the Greenwich meridian on decadal time scales: The Weddell gyre as a heat buffer, *Deep Sea Research Part II: Topical Studies in Oceanography*, *58*(25–26), 2509–2523, doi:10.1016/j.dsr2.2011.06.007.

Falkowski, P. G. (1994), The role of phytoplankton photosynthesis in global biogeochemical cycles, *Photosynthesis Research*, *39*(3), 235–258, doi:10.1007/BF00014586.

Farneti, R., and T. L. Delworth (2010), The role of mesoscale eddies in the remote oceanic response to altered Southern Hemisphere winds, *Journal of Physical Oceanography*, *40*(10), 2348–2354, doi:10.1175/2010JPO4480.1.

Farneti, R., T. L. Delworth, A. J. Rosati, S. M. Griffies, and F. Zeng (2010), The role of mesoscale eddies in the rectification of the Southern Ocean response to climate change, *Journal of Physical Oceanography*, *40*(7), 1539–1557, doi:10.1175/2010JPO4353.1.

Fischer, A. D., E. A. Moberg, H. Alexander, E. F. Brownlee, K. R. Hunter-Cevera, K. J. Pitz, S. Z. Rosengard, and H. M. Sosik (2014), Sixty years of Sverdrup: A retrospective of progress in the study of phytoplankton blooms, *Oceanography*, *27*(1), 222–235, doi:10.5670/oceanog.2014.26.

Frölicher, T. L., J. L. Sarmiento, D. J. Paynter, J. P. Dunne, J. P. Krasting, and M. Winton (2015), Dominance of the Southern Ocean in anthropogenic carbon and heat uptake in CMIP5 models, *Journal of Climate*, *28*(2), 862–886, doi:10.1175/JCLI-D-14-00117.1.

Fyfe, J. C., and O. A. Saenko (2005), Human-induced change in the Antarctic Circumpolar Current, *Journal of Climate*, *18*(15), 3068–3073.

Gille, S. T. (2002), Warming of the Southern Ocean since the 1950s, *Science*, *295*(5558), 1275–1277, doi:10.1126/science.1065863.

Gille, S. T. (2008), Decadal-scale temperature trends in the Southern Hemisphere ocean, *Journal of Climate*, *21*(18), 4749–4765, doi:10.1175/2008JCLI2131.1.

Gillett, N., and J. Fyfe (2013), Annular mode changes in the CMIP5 simulations, *Geophysical Research Letters*, *40*(6), 1189–1193, doi:10.1002/grl.50249.

Gruber, N., M. Gloor, S. E. Mikaloff Fletcher, S. C. Doney, S. Dutkiewicz, M. J. Follows, M. Gerber, A. R. Jacobson, F. Joos, K. Lindsay, et al. (2009), Oceanic sources, sinks, and transport of atmospheric CO_2, *Global Biogeochemical Cycles*, *23*(GB1005), 1924–9224, doi:10.1029/2008GB003349.

Hallberg, R., and A. Gnanadesikan (2006), The role of eddies in determining the structure and response of the wind-driven Southern Hemisphere overturning: Results from the Modeling Eddies in the Southern Ocean (MESO) project, *Journal of Physical Oceanography*, *36*(12), 2232–2252, doi:10.1175/JPO2980.1.

Hauck, J., and C. Völker (2015), Rising atmospheric CO_2 leads to large impact of biology on Southern Ocean CO_2 uptake via changes of the Revelle factor, *Geophysical Research Letters*, *42*(5), 1459–1464, doi:10.1002/2015GL063070.

Hauck, J., C. Völker, T. Wang, M. Hoppema, M. Losch, and D. A. Wolf-Gladrow (2013), Seasonally different carbon flux changes in the Southern Ocean in response to the southern annular mode, *Global Biogeochemical Cycles*, *27*(4), 1236–1245, doi:10.1002/2013GB004600.

Hauck, J., C. Völker, D. Wolf-Gladrow, C. Laufkötter, M. Vogt, O. Aumont, L. Bopp, E. T. Buitenhuis, S. C. Doney, J. Dunne, et al. (2015), On the Southern Ocean CO_2 uptake and the role of the biological carbon pump in the 21st century, *Global Biogeochemical Cycles*, *29*(9), 1451–1470, doi:10.1002/2015GB005140.

Haumann, F. A., D. Notz, and H. Schmidt (2014), Anthropogenic influence on recent circulation-driven Antarctic sea ice changes, *Geophysical Research Letters*, *41*(23), 8429–8437, doi:10.1002/2014GL061659.

Haumann, F. A., N. Gruber, M. Münnich, I. Frenger, and S. Kern (2016), Sea-ice transport driving Southern Ocean salinity and its recent trends, *Nature*, *537*(7618), 89–92, doi:10.1038/nature19101.

Helm, K. P., N. L. Bindoff, and J. A. Church (2010), Changes in the global hydrological-cycle inferred from ocean salinity, *Geophysical Research Letters*, *37*(L18701), doi:10.1029/2010GL044222.

Hogg, A. M., P. Spence, O. A. Saenko, and S. M. Downes (2017), The energetics of Southern Ocean upwelling, *Journal of Physical Oceanography*, *47*(1), 135–153, doi:10.1175/JPO-D-16-0176.1.

Hogg, A. M. C., M. P. Meredith, J. R. Blundell, and C. Wilson (2008), Eddy heat flux in the Southern Ocean: Response to variable wind forcing, *Journal of Climate*, *21*(4), 608–620.

Holland, P. R., and R. Kwok (2012), Wind-driven trends in Antarctic sea-ice drift, *Nature Geoscience*, *5*(12), 872–875, doi:10.1038/ngeo1627.

Holte, J., and L. Talley (2009), A new algorithm for finding mixed layer depths with applications to Argo data and Subantarctic Mode Water formation, *Journal of Atmospheric and Oceanic Technology*, *26*(9), 1920–1939, doi:10.1175/2009JTECHO543.1.

Holzer, M., and F. W. Primeau (2013), Global teleconnections in the oceanic phosphorus cycle: Patterns, paths, and timescales, *Journal of Geophysical Research: Oceans*, *118*(4), 1775–1796, doi:10.1002/jgrc.20072.

Hoppema, M., K. Bakker, S. M. van Heuven, J. C. van Ooijen, and H. J. de Baar (2015), Distributions, trends and inter-annual variability of nutrients along a repeat section through the Weddell Sea (1996–2011), *Marine Chemistry*, *177*, 545–553, doi:10.1016/j.marchem.2015.08.007.

Hughes, C. W., and E. R. Ash (2001), Eddy forcing of the mean flow in the Southern Ocean, *Journal of Geophysical Research: Oceans*, *106*(C2), 2713–2722, doi:10.1029/2000JC900332.

Iida, T., T. Odate, and M. Fukuchi (2013), Long-Term Trends of Nutrients and Apparent Oxygen Utilization South of the Polar Front in Southern Ocean Intermediate Water from 1965 to 2008, *PloS one*, *8*(8), e71,766, doi:10.1371/journal.pone.0071766.

Jones, D. C., A. J. Meijers, E. Shuckburgh, J.-B. Sallée, P. Haynes, E. K. McAufield, and M. R. Mazloff (2016a), How does Subantarctic Mode Water ventilate the Southern Hemisphere subtropics?, *Journal of Geophysical Research: Oceans*, *121*(9), 6558–6582, doi:10.1002/2016JC011680.

Jones, J. M., S. T. Gille, H. Goosse, N. J. Abram, P. O. Canziani, D. J. Charman, K. R. Clem, X. Crosta, C. De Lavergne, I. Eisenman, et al. (2016b), Assessing recent trends in high-latitude Southern Hemisphere surface climate, *Nature Climate Change*, *6*(10), 917–926, doi:10.1038/NCLIMATE3103.

Joos, F., and R. Spahni (2008), Rates of change in natural and anthropogenic radiative forcing over the past 20,000 years, *Proceedings of the National Academy of Sciences*, *105*(5), 1425–1430.

Kang, Y. J., Y. Noh, and S.-W. Yeh (2010), Processes that influence the mixed layer deepening during winter in the North Pacific, *Journal of Geophysical Research: Oceans*, *115*(C12), doi:10.1029/2009JC005833.

Kara, A. B., P. A. Rochford, and H. E. Hurlburt (2000), Mixed layer depth variability and barrier layer formation over the North Pacific Ocean, *Journal of Geophysical Research: Oceans*, *105*(C7), 16,783–16,801, doi:10.1029/2000JC900071.

Kara, A. B., P. A. Rochford, and H. E. Hurlburt (2003), Mixed layer depth variability over the global ocean, *Journal of Geophysical Research: Oceans*, *108*(C3), 3079, doi:10.1029/2000JC000736.

Karleskind, P., M. Lévy, and L. Mémery (2011), Subduction of carbon, nitrogen, and oxygen in the northeast Atlantic, *Journal of Geophysical Research: Oceans*, *116*(C02025), doi:10.1029/2010JC006446.

Keeling, C. D., R. B. Bacastow, A. E. Bainbridge, C. A. Ekdahl Jr, P. R. Guenther, L. S. Waterman, and J. F. Chin (1976), Atmospheric carbon dioxide variations at Mauna Loa observatory, Hawaii, *Tellus*, *28*(6), 538–551, doi:10.3402/tellusa.v28i6.11322.

Khatiwala, S., F. Primeau, and T. Hall (2009), Reconstruction of the history of anthropogenic CO_2 concentrations in the ocean, *Nature*, *462*(7271), 346–349, doi:10.1038/nature08526.

Khatiwala, S., T. Tanhua, S. M. Fletcher, M. Gerber, S. Doney, H. Graven, N. Gruber, G. McKinley, A. Murata, A. Ríos, et al. (2013), Global ocean storage of anthropogenic carbon, *Biogeosciences (BG)*, *10*(4), 2169–2191, doi:10.5194/bg-10-2169-2013.

Kirtman, B., S. Power, A. Adedoyin, G. Boer, R. Bojariu, I. Camilloni, F. Doblas-Reyes, A. Fiore, M. Kimoto, G. Meehl, et al. (2013), Near-term Climate Change: Projections and Predictability. In: Climate Change 2013: The Physical Science Basis. Contribution of Working Group I to the Fifth Assessment Report of the Intergovernmental Panel on Climate Change .

Kushner, P. J., I. M. Held, and T. L. Delworth (2001), Southern Hemisphere atmospheric circulation response to global warming, *Journal of Climate*, *14*(10), 2238–2249, doi:10.1175/1520-0442(2001)014< 0001 : SHACRT > 2.0.CO; 2.

Landschützer, P., N. Gruber, F. A. Haumann, C. Rödenbeck, D. C. Bakker, S. Van Heuven, M. Hoppema, N. Metzl, C. Sweeney, T. Takahashi, et al. (2015), The reinvigoration of the Southern Ocean carbon sink, *Science*, *349*(6253), 1221–1224, doi:10.1126/science.aab2620.

Langlais, C., A. Lenton, R. Matear, D. Monselesan, B. Legresy, E. Cougnon, and S. Rintoul (2017), Stationary Rossby waves dominate subduction of anthropogenic carbon in the Southern Ocean, *Scientific Reports*, *7*(1), 17,076, doi:10.1038/s41598-017-17292-3.

Laufkötter, C., M. Vogt, N. Gruber, O. Aumont, L. Bopp, S. Doney, J. Dunne, J. Hauck, J. John, I. Lima, et al. (2015), Projected decreases in future marine export production: the role of the carbon flux through the upper ocean ecosystem., *Biogeosciences*, *13*(23), 4023–4047, doi: 10.5194/bg-13-4023-2016.

Le Quéré, C., C. Rödenbeck, E. T. Buitenhuis, T. J. Conway, R. Langenfelds, A. Gomez, C. Labuschagne, M. Ramonet, T. Nakazawa, N. Metzl, et al. (2007), Saturation of the Southern Ocean CO_2 sink due to recent climate change, *science*, *316*(5832), 1735–1738, doi: 10.1126/science.1136188.

Le Quéré, C., M. R. Raupach, J. G. Canadell, G. Marland, L. Bopp, P. Ciais, T. J. Conway, S. C. Doney, R. A. Feely, P. Foster, et al. (2009), Trends in the sources and sinks of carbon dioxide, *Nature Geoscience*, *2*(12), 831–836, doi:10.1038/ngeo689.

Le Quéré, C., R. M. Andrew, P. Friedlingstein, S. Sitch, J. Pongratz, A. C. Manning, J. I. Korsbakken, G. P. Peters, J. G. Canadell, R. B. Jackson, et al. (2017), Global Carbon Budget 2017, *Earth System Science Data Discussions*, pp. 1–79, doi:10.5194/essd-2017-123.

Lee, M.-M., A. G. Nurser, I. Stevens, and J.-B. Sallée (2011), Subduction over the Southern Indian Ocean in a high-resolution atmosphere–ocean coupled model, *Journal of Climate*, *24*(15), 3830–3849, doi:10.1175/2011JCLI3888.1.

Lee, S., and S. B. Feldstein (2013), Detecting ozone-and greenhouse gas–driven wind trends with observational data, *Science*, *339*(6119), 563–567, doi:10.1126/science.1225154.

Levitus, S., J. I. Antonov, T. P. Boyer, O. K. Baranova, H. E. Garcia, R. A. Locarnini, A. V. Mishonov, J. Reagan, D. Seidov, E. S. Yarosh, et al. (2012), World ocean heat content and thermosteric sea level change (0–2000 m), 1955–2010, *Geophysical Research Letters*, *39*(L10603), doi:10.1029/2012GL051106.

Lévy, M., L. Bopp, P. Karleskind, L. Resplandy, C. Éthé, and F. Pinsard (2013), Physical pathways for carbon transfers between the surface mixed layer and the ocean interior, *Global Biogeochemical Cycles*, *27*(4), 1001–1012, doi:10.1002/gbc.20092.

Longhurst, A. (1995), Seasonal cycles of pelagic production and consumption, *Progress in Oceanography*, *36*(2), 77–167, doi:10.1016/0079-6611(95)00015-1.

Lorbacher, K., D. Dommenget, P. Niiler, and A. Köhl (2006), Ocean mixed layer depth: A subsurface proxy of ocean-atmosphere variability, *Journal of Geophysical Research: Oceans*, *111*(C7), doi:10.1029/2003JC002157.

Lovenduski, N. S., and N. Gruber (2005), Impact of the Southern Annular Mode on Southern Ocean circulation and biology, *Geophysical Research Letters*, *32*(11), doi: 10.1029/2005GL022727.

Lovenduski, N. S., N. Gruber, and S. C. Doney (2008), Toward a mechanistic understanding of the decadal trends in the Southern Ocean carbon sink, *Global Biogeochemical Cycles*, *22*(GB3016), doi:10.1029/2007GB003139.

Lozier, M. S. (2010), Deconstructing the Conveyor Belt, *Science*, *328*(5985), 1507–1511, doi: 10.1126/science.1189250.

Lumpkin, R., and K. Speer (2007), Global ocean meridional overturning, *Journal of Physical Oceanography*, *37*(10), 2550–2562, doi:10.1175/JPO3130.1.

Marinov, I., A. Gnanadesikan, J. Toggweiler, and J. Sarmiento (2006), The Southern Ocean biogeochemical divide, *Nature*, *441*(7096), 964–967, doi:10.1038/nature04883.

Marshall, D. (1997), Subduction of water masses in an eddying ocean, *Journal of Marine Research*, *55*(2), 201–222, doi:10.1357/0022240973224373.

Marshall, G. J. (2003), Trends in the Southern Annular Mode from observations and reanalyses, *Journal of Climate*, *16*(24), 4134–4143, doi:10.1175/1520-0442(2003)016$< 4134 : TITSAM >$ $2.0.CO; 2$.

Marshall, J., and K. Speer (2012), Closure of the meridional overturning circulation through Southern Ocean upwelling, *Nature Geoscience*, *5*(3), 171–180, doi:10.1038/NGEO1391.

Marshall, J. C., R. G. Williams, and A. G. Nurser (1993), Inferring the subduction rate and period over the North Atlantic, *Journal of Physical Oceanography*, *23*(7), 1315–1329, doi: 10.1175/1520-0485(1993)023$< 1315 : ITSRAP > 2.0.CO; 2$.

Meijers, A. (2014), The Southern Ocean in the Coupled Model Intercomparison Project phase 5, *Phil. Trans. R. Soc. A*, *372*, 20130,296, doi:10.1098/rsta.2013.0296.

Meredith, M. P., and A. M. Hogg (2006), Circumpolar response of Southern Ocean eddy activity to a change in the Southern Annular Mode, *Geophysical Research Letters*, *33*(16), doi:10.1029/2006GL026499.

Meredith, M. P., A. C. Naveira Garabato, A. M. Hogg, and R. Farneti (2012), Sensitivity of the overturning circulation in the Southern Ocean to decadal changes in wind forcing, *Journal of Climate*, *25*(1), 99–110, doi:10.1175/2011JCLI4204.1.

Monterey, G., and S. Levitus (1997), Climatological cycle of mixed layer depth in the world ocean, *US government printing office, NOAA NESDIS, Washington, DC.*

Morrison, A. K., and A. M. Hogg (2013), On the relationship between Southern Ocean overturning and ACC transport, *Journal of Physical Oceanography*, *43*(1), 140–148, doi:10.1175/JPO-D-12-057.1.

Morrison, A. K., T. L. Frölicher, and J. L. Sarmiento (2015), Upwelling in the Southern Ocean, *Physics Today*, *68*(1), 27, doi:10.1063/PT.3.2654.

Obata, A., J. Ishizaka, and M. Endoh (1996), Global verification of critical depth theory for phytoplankton bloom with climatological in situ temperature and satellite ocean color data, *Journal of Geophysical Research: Oceans*, *101*(C9), 20,657–20,667, doi:10.1029/96JC01734.

Orr, J. C., V. J. Fabry, O. Aumont, L. Bopp, S. C. Doney, R. A. Feely, A. Gnanadesikan, N. Gruber, A. Ishida, F. Joos, et al. (2005), Anthropogenic ocean acidification over the twenty-first century and its impact on calcifying organisms, *Nature*, *437*(7059), 681–686, doi: 10.1038/nature04095.

Palter, J., J. Sarmiento, A. Gnanadesikan, J. Simeon, and R. Slater (2010), Fueling export production: Nutrient return pathways from the deep ocean and their dependence on the Meridional Overturning Circulation, *Biogeosciences*, *7*(11), 3549–3568, doi:10.5194/bg-7-3549-2010.

Panassa, E., J. M. Santana-Casiano, M. González-Dávila, M. Hoppema, S. M. van Heuven, C. Völker, D. Wolf-Gladrow, and J. Hauck (2018), Variability of nutrients and carbon dioxide in the Antarctic Intermediate Water between 1990 and 2014, *Ocean Dynamics*, *68*(3), 295–308, doi:10.1007/s10236-018-1131-2.

Pardo, P. C., B. Tilbrook, C. Langlais, T. W. Trull, and S. R. Rintoul (2017), Carbon uptake and biogeochemical change in the Southern Ocean, south of Tasmania, *Biogeosciences*, *14*(22), 5217–5237, doi:10.5194/bg-14-5217-2017.

Polovina, J. J., G. T. Mitchum, and G. T. Evans (1995), Decadal and basin-scale variation in mixed layer depth and the impact on biological production in the Central and North Pacific, 1960-88, *Deep Sea Research Part I: Oceanographic Research Papers*, *42*(10), 1701–1716, doi:10.1016/0967-0637(95)00075-H.

Rintoul, S. R., and T. W. Trull (2001), Seasonal evolution of the mixed layer in the Subantarctic Zone south of Australia, *Journal of Geophysical Research: Oceans*, *106*(C12), 31,447–31,462, doi:10.1029/2000JC000329.

Rödenbeck, C., D. C. Bakker, N. Gruber, Y. Iida, A. R. Jacobson, S. Jones, P. Landschützer, N. Metzl, S.-i. Nakaoka, A. Olsen, et al. (2015), Data-based estimates of the ocean carbon sink variability–first results of the Surface Ocean pCO$_2$ Mapping intercomparison (SOCOM), *Biogeosciences*, *12*, 7251–7278, doi:10.5194/bg-12-7251-2015.

Russell, J. L., K. W. Dixon, A. Gnanadesikan, R. J. Stouffer, and J. Toggweiler (2006), The Southern Hemisphere westerlies in a warming world: Propping open the door to the deep ocean, *Journal of Climate*, *19*(24), 6382–6390, doi:10.1175/JCLI3984.1.

Rye, C. D., A. C. N. Garabato, P. R. Holland, M. P. Meredith, A. G. Nurser, C. W. Hughes, A. C. Coward, and D. J. Webb (2014), Rapid sea-level rise along the Antarctic margins in response to increased glacial discharge, *Nature Geoscience*, *7*(10), 732–735, doi:10.1038/NGEO2230.

Sabine, C. L., R. A. Feely, N. Gruber, R. M. Key, K. Lee, J. L. Bullister, R. Wanninkhof, C. Wong, D. W. Wallace, B. Tilbrook, et al. (2004), The oceanic sink for anthropogenic CO$_2$, *Science*, *305*(5682), 367–371, doi:10.1126/science.1097403.

Sallée, J., K. Speer, and S. Rintoul (2010a), Zonally asymmetric response of the Southern Ocean mixed-layer depth to the Southern Annular Mode, *Nature Geoscience*, *3*(4), 273–279, doi:10.1038/ngeo812.

Sallée, J.-B., R. Morrow, and K. Speer (2008), Eddy heat diffusion and Subantarctic Mode Water formation, *Geophysical Research Letters*, *35*(L05607), doi:10.1029/2007GL032827.

Sallée, J.-B., K. Speer, S. Rintoul, and S. Wijffels (2010b), Southern Ocean Thermocline Ventilation, *Journal of Physical Oceanography*, *40*(3), 509–529, doi:10.1175/2009JPO4291.1.

Sallée, J.-B., R. J. Matear, S. R. Rintoul, and A. Lenton (2012), Localized subduction of anthropogenic carbon dioxide in the Southern Hemisphere oceans, *Nature Geoscience*, *5*(8), 579–584, doi:10.1038/ngeo1523.

Salt, L. A., S. M. van Heuven, M. E. Claus, E. M. Jones, and H. de Baar (2015), Rapid acidification of mode and intermediate waters in the southwestern Atlantic Ocean, *Biogeosciences*, *12*(5), 1387–1401, doi:10.5194/bgd-11-6755-2014.

Sarmiento, J., N. Gruber, M. Brzezinski, and J. Dunne (2004), High-latitude controls of thermocline nutrients and low latitude biological productivity, *Nature*, *427*(6969), 56–60, doi: 10.1038/nature02204.

Sarmiento, J. L., T. M. Hughes, R. J. Stouffer, and S. Manabe (1998), Simulated response of the ocean carbon cycle to anthropogenic climate warming, *Nature*, *393*(6682), 245–249, doi:10.1038/30455.

Schmidtko, S., K. J. Heywood, A. F. Thompson, and S. Aoki (2014), Multidecadal warming of Antarctic waters, *Science*, *346*(6214), 1227–1231, doi:10.1126/science.1256117.

Screen, J. A., N. P. Gillett, D. P. Stevens, G. J. Marshall, and H. K. Roscoe (2009), The role of eddies in the Southern Ocean temperature response to the Southern Annular Mode, *Journal of Climate*, *22*(3), 806–818, doi:10.1175/2008JCLI2416.1.

Sigman, D. M., and M. P. Hain (2012), The Biological Productivity of the Ocean, *Nature Education Knowledge*, *3*(10), 21.

Sloyan, B. M., and S. R. Rintoul (2001), The Southern Ocean limb of the global deep overturning circulation, *Journal of Physical Oceanography*, *31*(1), 143–173, doi:10.1175/1520-0485(2001)031< 0143 : TSOLOT > 2.0.CO; 2.

Smetacek, V., C. Klaas, V. H. Strass, P. Assmy, M. Montresor, B. Cisewski, N. Savoye, A. Webb, F. d'Ovidio, J. M. Arrieta, et al. (2012), Deep carbon export from a Southern Ocean iron-fertilized diatom bloom, *Nature*, *487*(7407), 313–319, doi:10.1038/nature11229.

Sokolov, S., and S. R. Rintoul (2007), Multiple jets of the Antarctic Circumpolar Current south of Australia, *Journal of Physical Oceanography*, *37*(5), 1394–1412, doi:10.1175/JPO3111.1.

Sokolov, S., and S. R. Rintoul (2009a), Circumpolar structure and distribution of the Antarctic Circumpolar Current fronts: 1. Mean circumpolar paths, *Journal of Geophysical Research: Oceans*, *114*(C11), doi:10.1029/2008JC005108.

Sokolov, S., and S. R. Rintoul (2009b), Circumpolar structure and distribution of the Antarctic Circumpolar Current fronts: 2. Variability and relationship to sea surface height, *Journal of Geophysical Research: Oceans*, *114*(C11019), doi:10.1029/2008JC005248.

Speer, K., S. R. Rintoul, and B. Sloyan (2000), The Diabatic Deacon Cell, *Journal of Physical Oceanography*, *30*(12), 3212–3222, doi:10.1175/1520-0485(2000)030< 3212 : TDDC > 2.0.CO; 2.

Sundquist, E. T. (1993), The Global Carbon Dioxide Budget, *Science*, *259*(5097), 934–941, doi:10.1126/science.259.5097.934.

Sverdrup, H. (1953), On conditions for the vernal blooming of phytoplankton, *Journal du Conseil*, *18*(3), 287–295.

Talley, L. D. (2008), Freshwater transport estimates and the global overturning circulation: Shallow, deep and throughflow components, *Progress in Oceanography*, *78*(4), 257–303, doi: 10.1016/j.pocean.2008.05.001.

Talley, L. D. (2013), Closure of the global overturning circulation through the Indian, Pacific, and Southern Oceans: Schematics and transports, *Oceanography*, *26*(1), 80–97, doi: 10.5670/oceanog.2013.07.

Tanhua, T., M. Hoppema, E. M. Jones, T. Stöven, J. Hauck, M. G. Dávila, M. Santana-Casiano, M. Álvarez, and V. H. Strass (2017), Temporal changes in ventilation and the carbonate system in the Atlantic sector of the Southern Ocean, *Deep Sea Research Part II: Topical Studies in Oceanography*, *138*, 26–38, doi:10.1016/j.dsr2.2016.10.004.

Thompson, D. W., and S. Solomon (2002), Interpretation of recent Southern Hemisphere climate change, *Science*, *296*(5569), 895–899, doi:10.1126/science.1069270.

Thompson, D. W., S. Solomon, P. J. Kushner, M. H. England, K. M. Grise, and D. J. Karoly (2011), Signatures of the Antarctic ozone hole in Southern Hemisphere surface climate change, *Nature Geoscience*, *4*(11), 741–749, doi:10.1038/NGEO1296.

Thomson, R. E., and I. V. Fine (2003), Estimating mixed layer depth from oceanic profile data, *Journal of Atmospheric and Oceanic Technology*, *20*(2), 319–329, doi:10.1175/1520-0426(2003)020¡0319:EMLDFO¿2.0.CO;2.

Trossman, D., L. Thompson, S. Mecking, and M. Warner (2012), On the formation, ventilation, and erosion of mode waters in the North Atlantic and Southern Oceans, *Journal of Geophysical Research: Oceans*, *117*(C09026), doi:10.1029/2012JC008090.

Turner, J., J. S. Hosking, T. J. Bracegirdle, G. J. Marshall, and T. Phillips (2015), Recent changes in Antarctic Sea ice, *Philosophical Transactions of the Royal Society of London A: Mathematical, Physical and Engineering Sciences*, *373*(2045), 20140,163, doi:10.1098/rsta.2014.0163.

van Heuven, S. M., M. Hoppema, O. Huhn, H. A. Slagter, and H. J. de Baar (2011), Direct observation of increasing CO_2 in the Weddell Gyre along the Prime Meridian during 1973–2008, *Deep Sea Research Part II: Topical Studies in Oceanography*, *58*(25-26), 2613–2635, doi:10.1016/j.dsr2.2011.08.007.

van Heuven, S. M., M. Hoppema, E. M. Jones, and H. J. de Baar (2014), Rapid invasion of anthropogenic CO_2 into the deep circulation of the Weddell Gyre, *Phil. Trans. R. Soc. A*, *372*, 20130,056, doi:10.1098/rsta.2013.0056.

Villalba, R., A. Lara, M. H. Masiokas, R. Urrutia, B. H. Luckman, G. J. Marshall, I. A. Mundo, D. A. Christie, E. R. Cook, R. Neukom, et al. (2012), Unusual Southern Hemisphere tree growth patterns induced by changes in the Southern Annular Mode, *Nature Geoscience*, *5*(11), 793–798, doi:10.1038/NGEO1613.

Volk, T., and M. I. Hoffert (1985), Ocean carbon pumps: Analysis of relative strengths and efficiencies in ocean-driven atmospheric CO_2 changes, *American Geophysical Union*, pp. 99–110, doi:10.1029/GM032p0099.

Whitworth, T., and W. D. Nowlin (1987), Water masses and currents of the Southern Ocean at the Greenwich Meridian, *Journal of Geophysical Research: Oceans*, *92*(C6), 6462–6476, doi:10.1029/JC092iC06p06462.

Whitworth III, T. (1988), The Antarctic Circumpolar Current, *Oceanus*, *31*(2), 53–58.

Wijesekera, H. W., and M. C. Gregg (1996), Surface layer response to weak winds, westerly bursts, and rain squalls in the western Pacific Warm Pool, *Journal of Geophysical Research: Oceans*, *101*(C1), 977–997, doi:10.1029/95JC02553.

Williams, R. G., and M. J. Follows (2003), Physical transport of nutrients and the maintenance of biological production, in *Ocean Biogeochemistry*, pp. 19–51, Springer.

Wunsch, C. (1998), The work done by the wind on the oceanic general circulation, *Journal of Physical Oceanography*, *28*(11), 2332–2340, doi:10.1175/1520-0485(1998)028¡2332:TWDBTW¿2.0.CO;2.

Zeebe, R. E., and D. A. Wolf-Gladrow (2001), CO_2 *in seawater: equilibrium, kinetics, isotopes*, 65, 346 pp., Elsevier Oceanography Series.

Zickfeld, K., M. Eby, and A. J. Weaver (2008), Carbon-cycle feedbacks of changes in the atlantic meridional overturning circulation under future atmospheric co2, *Global Biogeochemical Cycles*, *22*(GB3024), doi:10.1029/2007GB003118.

Universität Bremen

Name: _Essowè Panassa_____ Ort, Datum: Bremerhaven, 5.March 2018 _____

Anschrift: Rutenbergstr. 24, 27568 Bremerhaven
_____

ERKLÄRUNG

.

Hiermit erkläre ich, dass ich die Doktorarbeit mit dem Titel:

**Role of Mixed Layer Depth and Subduction Processes for the Southern Ocean
Carbon and Nutrient Cycles**
_____

_____

_____

selbstständig verfasst und geschrieben habe und außer den angegebenen Quellen keine weiteren
Hilfsmittel verwendet habe.

Ebenfalls erkläre ich hiermit, dass es sich bei den von mir abgegebenen Arbeiten um drei
identische Exemplare handelt.

_____
        (Unterschrift)

iv